Single-cell image analysis and machine learning methods using the cellular microenvironment

Ph.D. Thesis

Tímea Tóth

Supervisor:

Péter Horváth, PhD

Doctoral School of Biology,

Faculty of Science and Informatics, University of Szeged

Department of Biochemistry, Biological Research Centre, Szeged

Szeged

2023

Publications

The graduation procedure is based on the following publications:

Toth, T., Balassa, T., Bara, N., Kovacs, F., Kriston, A., Molnar, C., Haracska, L., Sukosd, F., Horvath, P. (2018) *Environmental properties of cells improve machine learning-based phenotype recognition accuracy*. Scientific Reports 8, 10085

IF: 4.011

Toth, T., Bauer, D., Sukosd, F., Horvath, P. (2022) *Fisheye transformation enhances deep-learning-based single-cell phenotyping by including cellular microenvironment*. Cell Reports Methods, 2(12), 100339.

IF: 3.8

Other publications related to the subject of this thesis:

Diosdi, A., Hirling, D., Kovacs, M., **Toth, T.**, Harmati, M., Koos, K., Buzas, K., Piccinini, F., Horvath, P. (2021) *A quantitative metric for the comparative evaluation of optical clearing protocols for 3D multicellular spheroids*. Computational and Structural Biotechnology Journal 19, 1233-1243

IF: 6.155

Diosdi, A., Hirling, D., Kovacs, M., **Toth, T.**, Harmati, M., Koos, K., Buzas, K., Piccinini, F., Horvath, P. (2021) *Cell lines and clearing approaches: a single-cell level 3D light-sheet fluorescence microscopy dataset of multicellular spheroids*. Data in Brief 36, 107090

IF: not applicable

Tasnadi, E., **Toth, T.**, Kovacs, M., Diosdi, A., Pampaloni, F., Molnar, J., Piccinini, F., Horvath, P. (2020) *3D-Cell-Annotator: an open-source active surface tool for single-cell segmentation in 3D microscopy images*. Bioinformatics, Volume 36, Issue 9, May 2020, Pages 2948–2949

IF: 6.937

Piccinini, F., Balassa, T., Carbonaro, A., Diosdi, A., **Toth, T.**, Moshkov, N., Tasnadi, E., Horvath, P. (2020) *Software tools for 3D nuclei segmentation and quantitative analysis in multicellular aggregates*. Computational and Structural Biotechnology Journal 18, 1287-1300

IF: 7.271

Hollandi, R., Szkalisity, A., **Toth, T.**, Tasnadi, E., Molnar, C., Mathe, B., Grexa, I., Molnar, J., Balind, A., Gorbe, M., Kovacs, M., Migh, E., Goodman, A., Balassa, T., Koos, K., Wang, W., Caicedo, J.C., Bara, N., Kovacs, F., Paavolainen, L., Danka, T., Kriston, A., Carpenter, A.E., Smith, K., Horvath, P. (2020) *nucleAIzer: a parameter-free deep learning framework for nucleus segmentation using image style transfer*. Cell Systems 10 (5), 453-458. e6

IF: 10.304

Cumulative IF: 38.478

Table of contents

List of abbreviations

DAPI – 4′,6-diamidino-2-phenylindole

DL – deep learning

DMEM – Dulbecco's Modified Eagle Medium

DNN – deep neural network

FBS – Fetal Bovine Serum

GFP – Green Fluorescent Protein

GPU – graphics processing unit

HE – hematoxylin-eosin

KNN – K-nearest neighbours

LC – lung cancer

MCF-7 – Michigan Cancer Foundation-7 (breast cancer cell line)

MLP – multilayer perceptron

MRC-5 – Medical Research Council cell strain 5

P/S/A – Penicillin-Streptomycin-Amphotericin

PBS – Phosphate Buffered Saline

PFA – paraformaldehyde

RI – refractive index

SLIC – simple linear iterative clustering

SMO – sequential minimal optimization

UBC – urinary bladder cancer

1. Introduction

All living entities adapt to their environment. This phenomenon can be observed as morphological differences both at the macro- and microscales. Microscopy became a crucial tool for cell biology because it allowed researchers to go beyond the limits of the human eye and recognise structural differences between individual cells. With the development of optical, chemical and electronic technologies, modern automated microscopes produce thousands of images routinely.

In order to draw conclusions and suggest an appropriate diagnosis or treatment, biological samples are frequently examined at the single-cell level in biological research and medical examinations. The key step in treatment development is to validate efficacy on target cell types [1]. Cell cultures or tissue samples from patients can be used to study a treatment's effects. For each case, precise and reliable results depend on single-cell phenotyping. The phenotype of a cell is the culmination of numerous cellular processes – driven by the organism's genetic code and environmental factors – that result in a unique morphological trait. Visual cell phenotyping is the characterization and quantification of these cellular features in images. Image-based phenotypic classifications are usually performed by machine-learning algorithms.

Machine learning methods are designed to learn functional correlations based on features and solve tasks like classification, regression or clustering [2]. Image processing and classical machine learning approaches have been widely used to decipher significant biological patterns [3, 4]. However, a new generation of image analysis algorithms has been able to thrive thanks to the development of deep learning-based computer vision methods [5].

Machine learning earned a crucial role in cell biology and in medical image analysis. One of the reasons behind that is developments in microscopy and computational cell biology led to a massive increase in data volume, frequently as large as millions of images per study. Researchers nowadays prefer these high-content screenings, however analysing the produced datasets manually is either time-consuming or downright impossible. Another reason is that there is a chance that machines could see useful properties in images that are invisible for the human eye. It is in everyone's interest to get precise medical diagnosis

and reliable treatment suggestions and to achieve this, it is important to improve the accuracy of machine learning algorithms.

In this thesis, we show how taking the cellular microenvironment into account affects the phenotypic characterisation of single cells using supervised machine learning and deep learning [6, 7]. For the latter, we also propose a transformation similar to what is used in fisheye cameras to increase classification accuracy. Finally, we present the challenges we face when analysing 3-dimensional cell cultures. Outside of the classification procedure, we describe how to perform the necessary steps that precede the analysis: improve the quality of the microscopic images of these cultures [8], annotate [9] and segment cell nuclei [10].

1.1 Machine learning

Machine learning is a subfield of artificial intelligence that focuses on the development of algorithms and models that allow computers to learn from data and make predictions or decisions without being explicitly programmed. It involves the use of statistical methods and algorithms to build mathematical models of complex phenomena, making it possible to analyse and identify patterns in large datasets [11].

There are three main categories of machine learning algorithms: supervised learning, unsupervised learning, and semi-supervised learning [12]. In supervised learning, the algorithm is trained on a labelled dataset, meaning that the correct output is already known for each input example. The algorithm uses this labelled data to learn a mapping between inputs and outputs, allowing it to make predictions on new, unseen data. Commonly used algorithms that work in a supervised way include linear regression, logistic regression, and decision trees [13].

Unsupervised learning, on the other hand, involves training the algorithm on an unlabelled dataset, where the correct output is not known [14]. The goal of unsupervised learning is to identify patterns in the data, such as clusters or groups of similar examples. K-means clustering [15], hierarchical clustering [16], and principal component analysis [17] are widely used examples of this learning type.

In the semi-supervised learning approach, a small amount of labelled data is combined with a large amount of unlabelled data to train the algorithm [18]. The algorithm uses the labelled data to make predictions and then uses the information it learns from the predictions to improve its ability to make predictions on the unlabelled data. This process is repeated until the algorithm provides the best possible predictions for the entire dataset. Examples of semi-supervised learning algorithms include co-training and self-training [19].

All three approaches have been applied to a wide range of applications, from computer vision and natural language processing to finance and healthcare [11]. However, the choice of which approach to use depends on the specific problem being addressed and the characteristics of the data.

In recent years, machine learning methods have evolved significantly due to the increasing availability of large datasets and the development of more powerful computational resources [20]. This has enabled the development of deep learning algorithms, which use multiple layers of artificial neural networks to model different fields of life and science [21]. Deep learning has been particularly successful in tasks such as image classification [22] and natural language processing [23].

Despite the impressive results of machine learning algorithms, there are still many challenges that need to be addressed. Often, machine learning algorithms are susceptible to overfitting [24], which occurs when the algorithm becomes too specialised to the training data and is unable to make accurate predictions on new, unseen data. There is also ongoing work to improve the interpretability of machine learning models [25], so that it is easier for humans to understand why the algorithm makes certain predictions.

1.1.1 Classical supervised machine learning in biological image analysis

This section outlines a typical workflow for solving phenotypic classification using classical supervised machine learning [6], as depicted in Figure 1. The process begins with original images of biological samples, which are fed into segmentation algorithms to find the outlines of individual cells. From these segmented areas, computer-understandable

information is collected, which includes basic properties like intensity, texture, and shape of individual objects. Each cell has its own feature vector containing its data.

Once feature extraction is complete, a training database is created by a human expert who decides which phenotypes appear in the images. These phenotypes become the classes for machine learning. After adding enough training examples, the database is given to a machine learning algorithm, which aims to find the boundaries of each class in a multidimensional space (where the number of dimensions equal to the number of features used).

After the algorithm has completed the training phase, the resulting model can be saved and used to classify cells in new, previously unseen images. This workflow enables researchers to identify and study various phenotypes with high accuracy, providing insights into the underlying mechanisms of biological processes.
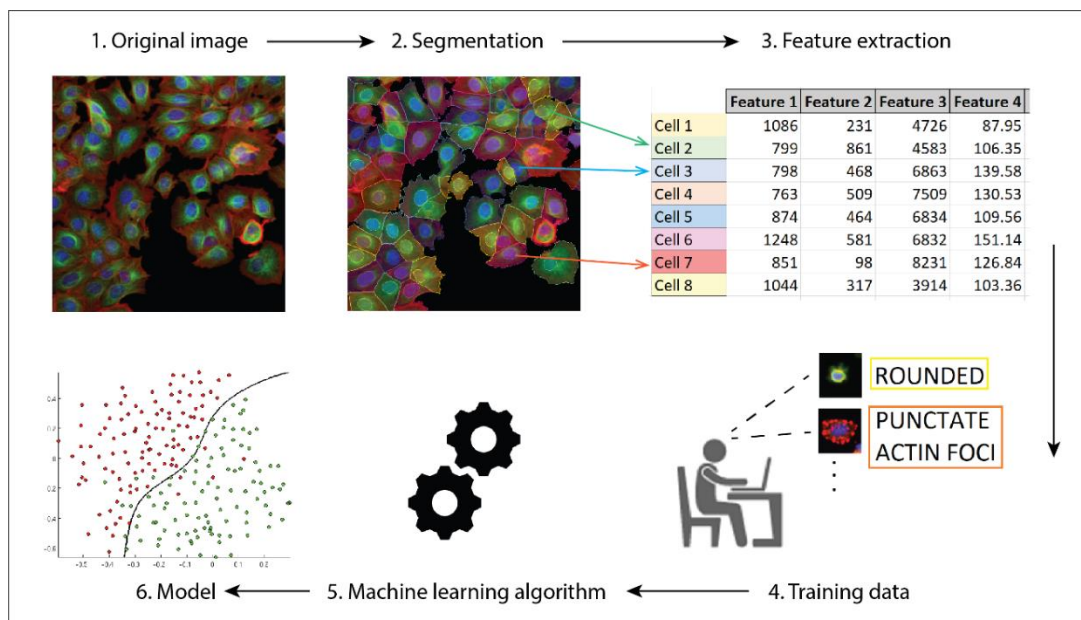

Figure 1 *Supervised machine learning process for biological image analysis*

1.1.2 Deep learning

Deep learning is a sub-field of neural networks, which is a sub-field of machine learning, all of which fall under the umbrella of artificial intelligence. Deep neural networks (DNNs) have been around since the 1960s, but their widespread use was limited due to

computational complexity and resource requirements [26–28]. Recent technological advancements, such as the availability of high-performance GPUs, have allowed for the rise of deep learning-powered applications.

Since their ground-breaking performance in the 2012 ImageNet challenge [29], deep learning techniques have been effectively used for a variety of visual identification tasks, such as pose estimation [30], activity recognition [31], object recognition [32], and object tracking [33]. In phenotypic image analysis, deep learning has taken the lead in tasks such as semantic segmentation, feature extraction, picture augmentation, and object detection [34].

DNNs use an end-to-end approach to learning, taking raw data as input and learning from training examples to produce the desired output. Unlike traditional machine learning techniques, which rely on manually selected features, DNNs automatically extract features from the data (Figure 2). DNNs are composed of multiple layers of artificial neurons that transform the data into a higher-level representation. This architecture allows for outstanding discriminatory power despite the simplicity of the individual calculations. Modern DNNs often contain hundreds of layers, and can learn to perform multiple tasks using the same network [35].

One of the main advantages of DNNs is their ability to perform transfer learning [36]. Transfer learning is the practice of using a pre-trained DNN for a new task, rather than starting the training from scratch [37]. This can greatly reduce the amount of data needed to train a new network, and can lead to better performance in some cases. Another advantage of DNNs is their ability to learn from large and diverse datasets, which can lead to better generalisation and robustness.

Despite their many advantages, DNNs are not without their challenges [38]. One of the biggest challenges is the need for large amounts of data to train the networks. Another challenge is the potential for overfitting, where the network becomes too specialised to the training data and performs poorly on new data. Additionally, DNNs can be computationally demanding, requiring powerful hardware to train and deploy.
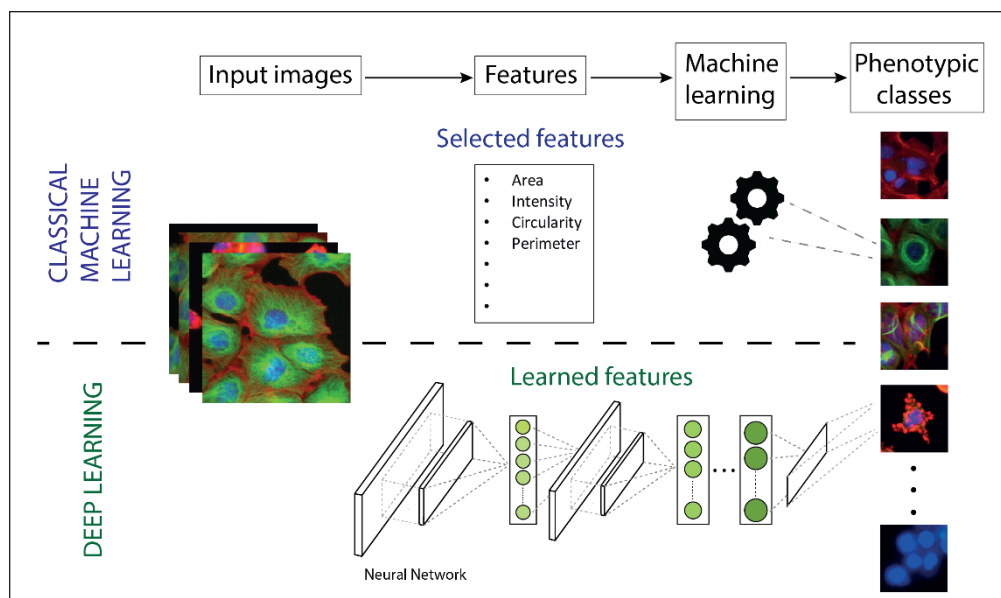
Figure 2 Differences between classical machine learning and deep learning. When solving a machine learning problem, we follow a specific workflow. We extract selected features from the input images, then with a machine learning algorithm, we create a model that describes or predicts the object. On the other hand, with deep learning, we skip the manual step of extracting features from images. Instead we feed the images directly into the deep learning network which then predicts the object's phenotypic class. Figure is partially adapted from [7].

Deep learning algorithms are more attractive than the conventional machine learning methods in a variety of aspects. Firstly, deep networks can learn to perform multiple tasks using the same network [39]. In addition, deep learning has the capacity to model highly complex functions, enabling it to solve issues that are beyond the scope of classical methods.

1.2 Biological background

Understanding cellular complexity is essential for treating diseases effectively and answering significant questions about cell biology. Personalised medicine has tremendous potential to become a widely used application for patients [40], but it requires the use of automated microscopes and appropriate analysis software to work efficiently. High-content screening is a popular method used with cell cultures to identify substances that can alter cell phenotype in a desired manner, such as small molecules, peptides, or RNAi [41]. Automated software capable of processing large amounts of data is used for

computational analysis [42]. Single-cell level analysis of cell cultures or tissue sections could provide a more precise description of the studied sample compared to looking at the sample as a whole. By considering the frequency and occurrence of affected cells, valuable insights can be gained into the functional differences between adapted and healthy samples. As a result, working on the single-cell level is essential for obtaining reliable information [43].

1.2.1 Cell cultures

For the past century, the most commonly used method for studying and analysing adherent cell lines has been 2D or monolayer culture [44, 45]. This involves growing cells on a flat surface, such as a plastic culture flask or Petri dish, which can be coated with proteins or other substances to aid in cell adhesion and promote their growth [46, 47]. Maintaining cells in these flasks is inexpensive and straightforward, and protocols have been developed that are robust and reduce the risk of contamination. Cell viability and morphology can be monitored easily as one can directly image through these substrates [48]. Additionally, it is simple to add reagents and take samples to analyse the effects of different conditions and stimuli.

High-content screening is a technique that enables the examination of various compounds and treatments on multiple cell lines simultaneously in multi-well plates [49]. Culturing is a convenient technique used to prepare and maintain cell cultures for high-content screening experiments. Patient-derived cells can also be cultured for clinical trials or medical treatments [50].

After undergoing microscopy, the acquired images are analysed with appropriate software [6]. Image processing is generally more straightforward for cell culture images compared to tissues, especially when using fluorescent labelling due to the negligible background signal [51]. Different kinds of labelling techniques can be applied to visualise the expression of certain protein products or more generally the functional integrity of cells. Fluorescent dyes are most frequently used to label certain proteins or cellular compartments [52], such as the nucleus, cell membrane, cytoskeletal proteins like actin or tubulin, lipid droplets, or virus particles in infection studies. DAPI or Hoechst are typically

used to label the nucleus, while Alexa Fluor dyes are usually used for the cytoskeleton. Expressed proteins are often tagged with GFP or mCherry. However, fluorescent labelling often prevents the examination of living cells, except for expressed fluorescent proteins, as the dye conjugation to the target biological structure may cause perturbations or even cell death [53].

1.2.2 Tissue sections

Tissue sections are thin slices of biological tissue that are used for a wide range of applications in biology, including histology, pathology, and molecular biology. These sections are typically generated through a process known as sectioning, in which a tissue sample is embedded in a matrix, such as paraffin or frozen media, and then sliced into thin sections using a microtome or cryostat [54]. The generation of tissue sections is a complex process that requires careful handling and processing of tissue samples to ensure that they are preserved in a manner that allows for accurate analysis. The choice of embedding matrix, slicing technique, and staining protocol can all impact the quality and integrity of the tissue section [55].

Histological analysis of tissue sections has been a cornerstone of medical research for over a century and has played a critical role in the diagnosis and treatment of diseases [56]. They are also widely used in molecular biology applications, such as in situ hybridization and immunohistochemistry [54]. These techniques allow researchers to localise specific molecules within the tissue section and to study their expression and distribution.

Samples in the form of tissue sections, originating from patients or model organisms, are commonly analysed in pathology to identify specific regions, such as tumorous or healthy [57]. In order to achieve our desired outcome, we may opt for brightfield microscopy instead of fluorescent microscopy, as it is more suitable for live-cell assays [53]. The most commonly used stain for tissue sections in histology is the hematoxylin and eosin stain, which allows pathologists to differentiate between different cellular compartments based on the staining patterns. Hematoxylin stains cell nuclei dark purple, while eosin stains the extracellular matrix and cytoplasm pink, with other components appearing in various combinations of these colours.

When conducting a software-guided analysis of tissue samples, their intrinsic 3D nature can pose challenges, as cells or nuclei located above or below the focal plane may be partly obscured by surrounding tissue, making accurate segmentation difficult [51]. However, the biological structure of the sample also means that cells imaged in tissue more closely resemble their true appearance than those in 2D culture, which can provide additional information on underlying cellular processes.

1.2.3 3D cell cultures

For decades, 2D monolayer cell cultures have been the go-to model systems to evaluate drug efficacy in drug discovery studies. These 2D cell culture systems are convenient, cost-effective, and widely used. However, they have several drawbacks and limitations. One of the main concerns is that the actual three-dimensional (3D) environment in which cancer cells exist in vivo is not accurately mimicked [58]. Thus, the 2D environment may provide misleading results regarding the expected responses of cancer cells to anticancer drugs [59]. Typically, the standard preclinical screening process for therapeutic agents involves testing compounds on 2D cell culture systems and animal models before introducing them in clinical trials [60]. However, the percentage of efficient agents dramatically decreases with each phase, and less than 5% of anticancer agents and small molecule oncology therapeutics pass the clinical trials and are finally approved for marketing by regulatory agencies [59]. One of the possible causes of this failure is that the drug responses of 2D cell cultures systems do not consistently predict the outcomes of clinical studies [61, 62].

The main drawback of conventional 2D culture is that it does not replicate the complex architecture and microenvironment of in vivo cells. As a result, cells cultured in 2D possess different characteristics such as morphology, proliferation, differentiation potential, cell-cell and cell-matrix interactions, and signal transduction, when compared to in vivo cells [63]. These concerns led to the development of 3D cell culture systems, which offer a promising solution to bridge the gap between cell-based assays and clinical trials. 3D cell culture systems provide a more physiologically relevant environment, closely resembling the behaviour of in vivo cells. In recent years, numerous in vitro platforms have been developed for 3D culture systems in cancer and stem cell research, including drug

development, biological research, tissue engineering, and other experimental analyses [64]. Therefore, cellular phenomena can be investigated under conditions that closely resemble the in vivo environment [65].

There are several 3D in vitro models that are currently used in biological laboratories, with spheroids being the most common [66]. Spheroids consist of clusters of cells arranged in a sphere-like structure and have several advantages over 2D cultures, including the ability to mimic in vivo conditions and preserve cell structure [67]. Consequently, spheroids are being increasingly used in drug discovery, tumour biology, and immunotherapy [68–70].

Despite the many benefits of using 3D cell cultures, large-scale image acquisition is still a major challenge, particularly with spheroids. The main issue is that it is difficult to visualise individual cells in the deeper layers of 3D samples due to limited light penetration and scattering. To address this problem, several optical clearing methods have been developed [8].

2. Aims

Our objective was to demonstrate how considering the cellular microenvironment during machine learning training impacts classification accuracy and determine the optimal distance from the cell of interest where the classifier performs with the highest efficiency. To accomplish this, we followed three main paths: 1) use information from the cell and its environment as input for classical machine learning algorithms, 2) use a fisheye-like transformation on original biological images and use these datasets as inputs for deep learning algorithms and 3) investigate the crucial steps required in 3D, such as 3D image acquisition, 3D cell annotation, 3D cell segmentation, and use a 3D co-culture dataset in which we distinguished phenotypes.

The main findings of this thesis are as follows.

1) Taking into account the environmental features of cells can enhance the accuracy of machine learning-based phenotypic classification.
2) Combining the cellular microenvironment with fisheye transformation can improve deep learning-based single-cell phenotyping.
3) Incorporating neighbourhood features can increase classification accuracy in 3D cell cultures.

3. Environmental features combined with classical machine learning

Understanding the diverse phenotypic structure of cellular systems is crucial to answer major biological questions. With the multitude of images that modern automated microscopes produce, manual analysis is nearly impossible. Because of that, machine learning-based analysis software earned a key role in single-cell-level profiling of large datasets. However, existing approaches are limited by only analysing the local features of the target cell in isolation, and do not include information from the cellular microenvironment.

In this part of the thesis, we demonstrate how including different environmental features can improve single-cell-level phenotypic analysis. The proposed methodology was tested on cell culture and tissue section images. We measured the size of the environment with Euclidean and KNN (K-nearest neighbours) distances. Our experimental results show that a cell's environment has a significant role in determining its entity.

3.1 Background

Analysing large bioimaging datasets produced during high-content screenings requires the development of automated and objective computational methods [71]. Numerous open-source and commercially available software have been developed to make image and computational data analysis more efficient [72–74]. CellProfiler became one of the most widely used open-source software for image processing [75]. It features modules for several image processing operations that can be performed task-by-task in a pipeline. This pipeline allows for the identification of biological objects—typically nuclei, cytoplasm, and cells—and the calculation of their metric features, such as their area, shape, texture, and intensity. Previous studies have suggested segmentation techniques for the differentiation of even more complex shape morphologies, like cells that are contacting or overlapping [76, 77].

Despite the developments in the field, it is still a challenge for single-cell segmentation methods to work on tissue section images. Therefore, we have chosen to apply the simple linear iterative clustering (SLIC) superpixel segmentation method on tissue sections to test

our hypothesis (that including the cellular microenvironment improves classification). Superpixel algorithms group pixels into larger coherent regions, thus they could replace the conventional pixel grid used in single-cell segmentation methods [78]. Superpixel algorithms became popular in computer vision applications because they are easy-to-use, fast, and produce high-quality segmentations. The SLIC algorithm generates superpixels by grouping pixels together based on similarities in intensity and location in the image plane [79].

Instead of manually verifying every experiment, machine learning techniques are made to discover functional relations from instances based on features [2]. Often, these techniques are more effective than traditional ones in handling multi-dimensional data analysis tasks like differentiating phenotypes that are defined by a large number of features [80, 81]. The extension of CellProfiler, CellProfiler Analyst applies supervised learning on features extracted from images of individual cells to identify their phenotypes [82, 83]. From version 2.0, it is written in Python, utilises a variety of machine learning techniques, performs classification at the cell and field-of-view levels, and offers a tool for visualising data from entire experiments [42]. CellClassifier displays the original microscope images so the users could annotate individual cells in their natural context [84]. Another software that uses CellProfiler metadata and is appropriate for multi-class classification is called Enhanced CellClassifier [85]. This program is able to distinguish between complex phenotypes. Advanced Cell Classifier is a graphical image analysis software in which users can use various machine learning methods [86]. Advanced Cell Classifier 2.0 has a built-in tool called phenotype finder, which allows researchers to reveal new and biologically important cell phenotypes [87]. Additionally, some programs have the ability to classify entire images rather than just individual objects (e.g., WND-CHARM, CP-CHARM) [88, 89].

The above-mentioned software have a major limitation in that they only operate at the single-cell level, and do not gather data from the cell's micro- or macroenvironment. As a result, they cannot account for the population context of the cell of interest. It has been demonstrated that both internal and extrinsic factors influence single-cell heterogeneity in cell populations [90–92]. Based on previous studies on genetically identical individual cells, it is hypothesised that differences in phenotypes are determined by the properties of growing cell populations, which create microenvironmental diversity to which cells

eventually adapt [93, 94]. The arrangement of cells inside tissues is also not random; the core of the cellular landscape is established even before differentiation, which is regulated by well-known biological mechanisms. As a result, the single-cell entity is strongly influenced by the cellular milieu. Based on this, it seems plausible that using environmental information of each individual cell of interest for machine learning applications would improve classification.

In this part of the thesis, we present a systematic analysis of how cellular neighbourhood impacts the phenotypic characterization of individual cells using supervised machine learning. For various neighbourhood sizes, environmental features were measured, and machine learning classification rates were compared. For the evaluations, a variety of well-known machine learning methods were applied. Data from tissue sections and cell cultures were used to compare the methods. Our results indicate that by including the features of the cell's surroundings in phenotypic analysis tools, we can significantly outperform conventional methods.

3.2 Datasets

We analysed two separate datasets to test our hypothesis utilising biological and clinical data. First, we tested data from a breast cancer cell line treated with various drugs used in medical practice. After that, we examined images of urinary bladder cancer tissue sections to confirm our findings and assess the performance of our method.

3.2.1 MCF-7 cell culture dataset

Our first dataset is a publicly available MCF-7 breast cancer cell line collection (available online at the Broad Bioimage Benchmark Collection [95] https://www.broadinstitute.org/bbbc/BBBC021/) that had been treated for 24 hours with 113 different small compounds at eight different doses. To summarise the treatments briefly, a specific group of targeted and cancer-relevant cytotoxic drugs were applied on the MCF-7 cell line. These drugs caused a wide range of aggressive and subtle cell phenotypes. The cells were then fixed, stained for DNA, F-actin, and B-tubulin and imaged by fluorescent microscopy. Images from 55 microtiter plates (with 96-well format) were

used to create the publicly accessible dataset. This dataset contains approximately 2 million cells in 39.000 images [96].

3.2.2. Urinary bladder cancer tissue sections

The images in our second image dataset are of a urinary bladder carcinoma (UBC) tissue sample. The images were acquired from patient derived samples were obtained from the University of Szeged (approval authorisation number: 5127, registration number: 17/2022-SZTE). The samples were obtained from 3 patients (sex and gender identity/age/stage of cancer of the subjects respectively: female/71/stage 2, male/65/stage 3, male/73/stage 2). According to standard histopathologic procedure, slides of urinary cancer tissue were stained with hematoxylin-eosin (HE). Formalin-fixed and paraffin-embedded tissues were cut in 4-µm-thick sections and stained in a Tissue-Tek DRS 2000E-D2 Slide Stainer (Sakura Finetek Japan) instrument according to the manufacturer's instructions. Images were taken by an Axio Imager Z.1 (Carl Zeiss Meditec AG, Germany) microscope equipped with an EC Plan-NEOFLUOAR 20x/0.5NA lens using the AxioVision SE64Rel.4.9.1.1 (Carl Zeiss Meditec AG, Germany) software.

3.3 Methods

3.3.1. Evaluation Software

For numerous steps in our experiments, we used an image analysis and machine learning software, BIAS (previously named as SCT Analyzer) developed by Single-Cell Technologies Ltd. (Szeged, Hungary). This software incorporates customisable cell segmentation algorithms, such as SLIC segmentation, and image pre-processing techniques (e.g. illumination correction, filtering). The user can annotate segmented regions into any number of phenotypic classes with the aid of an interactive interface. A variety of machine learning methods are available that can work on a single-cell-level. An active learning interface is also offered to increase user efficiency [97].

3.3.2 Segmentation

CellProfiler 2.2.0 was used to segment images from the high-content-screening dataset of drug-treated MCF-7 samples (Fig. 3a). Nuclei were detected using the adaptive Otsu algorithm. Cells with a diameter of less than 5 µm and nuclei touching the borders were excluded. Cytoplasm of cells was isolated using watershed separation based on the nuclei as seed points.
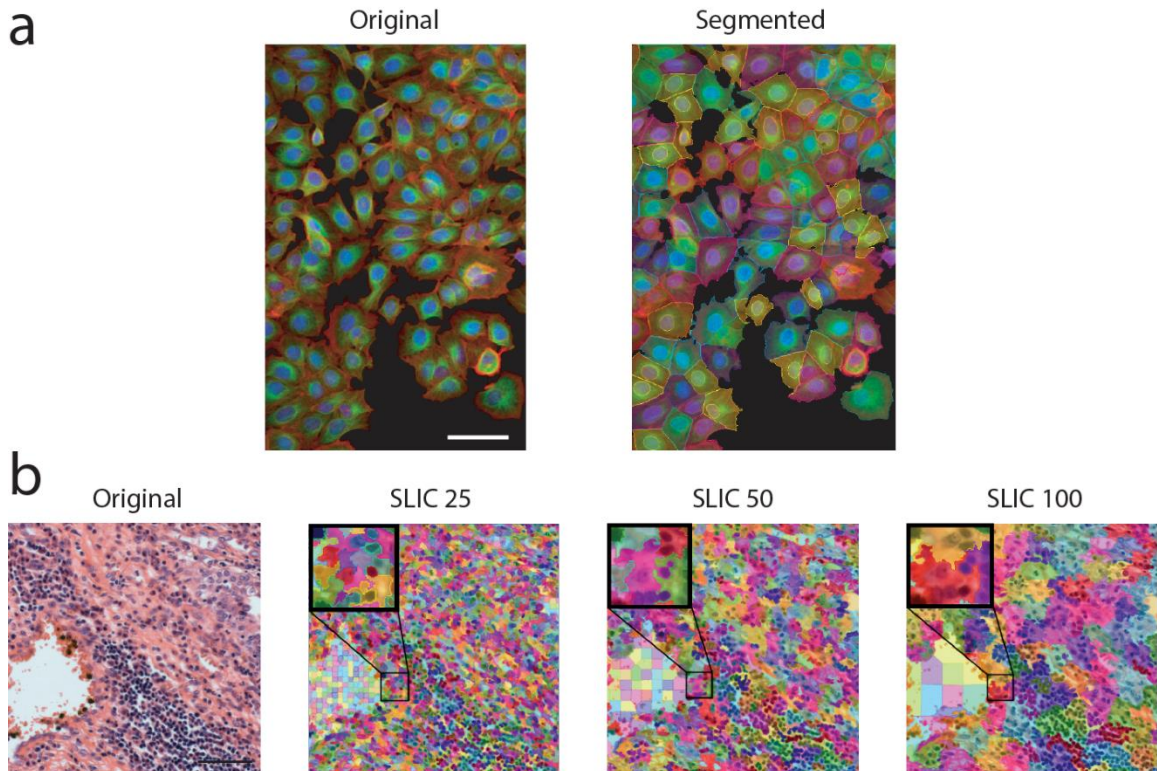
Figure 3 *Segmentation of cell culture and tissue section images. (a) Segmentation of the MCF-7 breast cancer cell line using CellProfiler 2.2.0. Scale bar: 50 µm (b) SLIC superpixel segmentation of urinary bladder cancer tissue section images. Images were segmented into superpixels of different sizes (25, 50, 100 pixels). Scale bar: 50 µm. Figure is adapted from* [6].

For the segmentation of the tissue dataset, we used the SLIC superpixel segmentation algorithm in BIAS. We tested different superpixel sizes: 25, 35, 50, 75, and 100 pixels - 6.75, 9.45, 13.5, 20.25, and 27 µm (Fig. 3b). For all cases, if the superpixels were smaller than 20, 25, 40, 60 or 75 pixels, respectively, we forced connectivity between them.

3.3.3 Feature extraction

We extracted the most commonly used cell-based and neighbourhood features. Regular features describe the intensity, texture, and shape of selected objects. We ran our experiment in three different ways: using only regular features, using only neighbourhood features and combining the two. The full list of features we used:

· *Regular features:* area, ellipse eccentricity, ellipse major axis length, ellipse minor axis length, ellipse orientation, enclosing circle radius, extent, form factor, Haralick texture features (angular second moment, contrast, correlation, sum of squares: variation, inverse difference moment, sum average, sum variance, sum entropy, entropy, difference variance, difference entropy, information measure of correlation), integrated intensity, intensity maximum, intensity mean, intensity median, intensity minimum, intensity standard deviation, perimeter, solidity.

· *Neighbourhood features:* the minimum, maximum, mean, median, and standard deviation statistics of the regular features; distance features: minimum, maximum, mean, median, standard deviation.

Before analysing the environment, we first computed all cellular features and then used these characteristics to describe the microenvironment. To calculate distances, we first found the centre of mass for each segmented area. We used two different approaches to get the neighbours of a cell: the K-nearest neighbours (KNN) and the N-distance methods (Fig. 4a, b). In the case of KNN (where 'K' denotes a positive integer) we chose the neighbouring cells based on Euclidean distance. For the other, we took a fixed N-pixel radius around an area's reference point and selected all cells/superpixels within this range. Once we had all neighbours for each individual cell, we calculated the neighbourhood features.

Neighbourhood features were computed from statistics of regular features. Distance statistics represent the localisation of the neighbouring cells. An additional feature was added for the Euclidean distance-based approach to describe the neighbourhood's size, i.e. the number of neighbours within the specified range (for KNN it was not necessary as 'K' was already known).
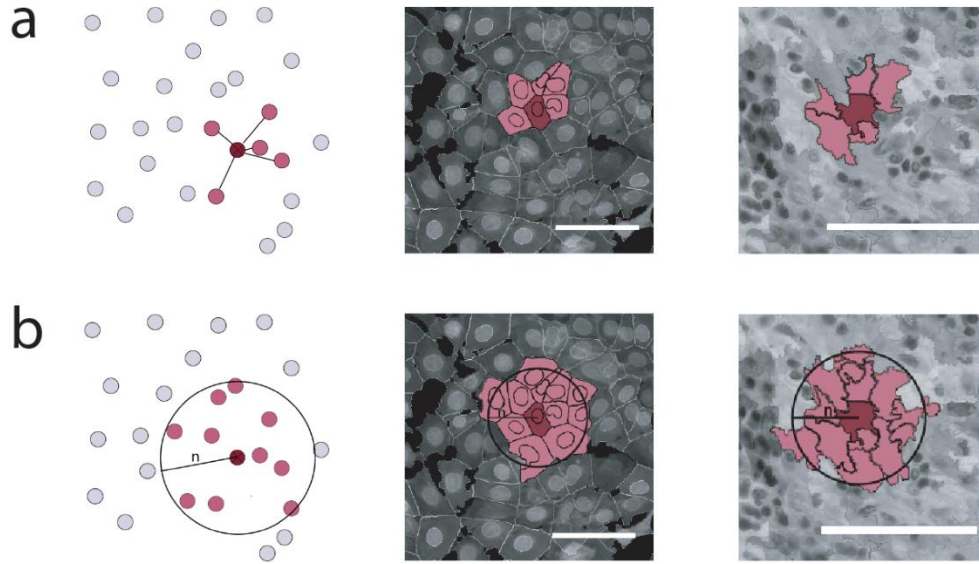
Figure 4 *Feature extraction. (a) The K-nearest neighbours (KNN) method, illustrated in a schematic figure and in real cell culture and tissue section scenarios, K=5. Scale bars: 25 μm (b) The n-distance method, illustrated in a schematic figure and in real cell culture and tissue section scenarios, n=50 pixels (cell culture: 19.51 μm, tissue sections: 13.5 μm). Scale bars: 25 μm. Figure is adapted from* [6].

Figure 5 is an example of how two cells with different phenotypes might have remarkably similar regular features and local appearances, but when additional neighbourhood properties are taken into account, we can see a clear distinction between them.

Figure 5 *Superpixels containing two different phenotypes (cancer cell and fibroblast) share highly similar regular features, but features of their neighbourhoods differ significantly. Scale bars: 50 μm. Figure is adapted from* [6].

3.3.4 Machine-learning algorithms

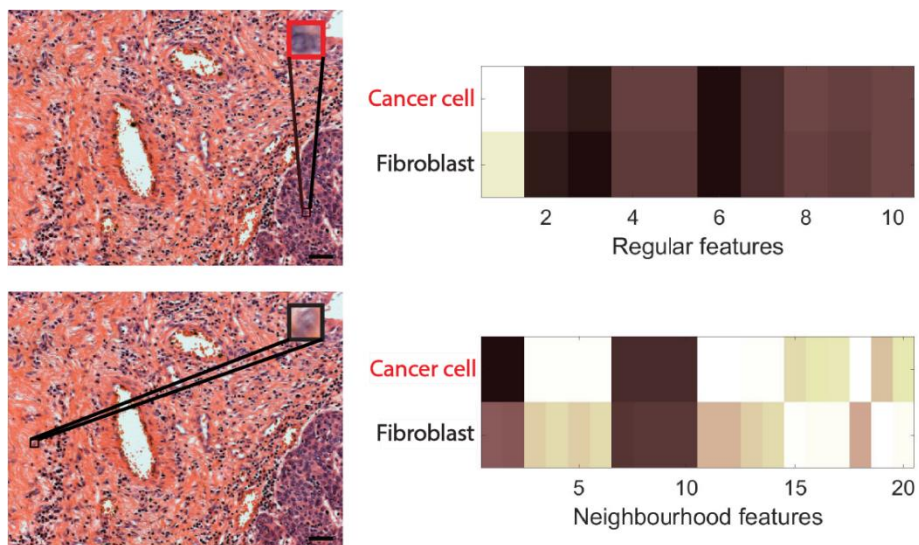After feature extraction, we created the annotated single-cell set for machine learning classification using BIAS. For the high-content-screening dataset, we used the phenotypic annotation set published by Piccinini and colleagues [87]. In their study, they applied the phenotype finder tool of Advanced Cell Classifier to identify biologically significant cell phenotypes in this dataset. Nine phenotypic classes (i.e. abundant, rounded, elongated, multinucleated, bundled microtubule, peripheral cytoskeleton, punctate actin foci, decreased cell size and fragmented nucleus) and a debris class were identified (Fig. 6a), and 1,673 cells were labelled (see Table 1). We took special care to prevent biasing of neighbourhood features by avoiding labelling identical cell types in close proximity, because in that arrangement, cells would have highly similar characteristics, which could lead to a bias in the evaluation.

Within the UBC cancer tissue image dataset, we distinguished eight different phenotypic classes: cancer cell, lumen, endothelial cell, stroma, fibroblast-fibrocyte, lymphocyte-plasma cell, smooth muscle, and lipocyte (Fig. 6b) and a debris class. We labelled an average of 1200 superpixels for each superpixel size. Table 1 contains the full list of labelled superpixels in each class. As this dataset contained a relatively low number of images (38), it was unavoidable to annotate cells in a close proximity. However, to ensure that cells close to each other are placed in either in the training or the test set (otherwise we may favourably bias the evaluation), we generated the cross-validation folders at the image level instead of the cell level.

Our aim was to find the optimal neighbourhood size, where machine-learning works with the highest classification accuracy. In the case of the UBC dataset, we also compared the classification performance on different superpixel sizes. For the evaluation we used Weka 3.8.1 (http://www.cs.waikato.ac.nz/ml/weka/), a machine learning and statistical framework.

We tested the performance of five classification methods: Naïve Bayes, Random Forest, Support Vector Machine (SMO), the Logistic Regression (Simple Logistic), and Multilayer Perceptron (MLP). We used 10-fold cross validation to measure the accuracy.
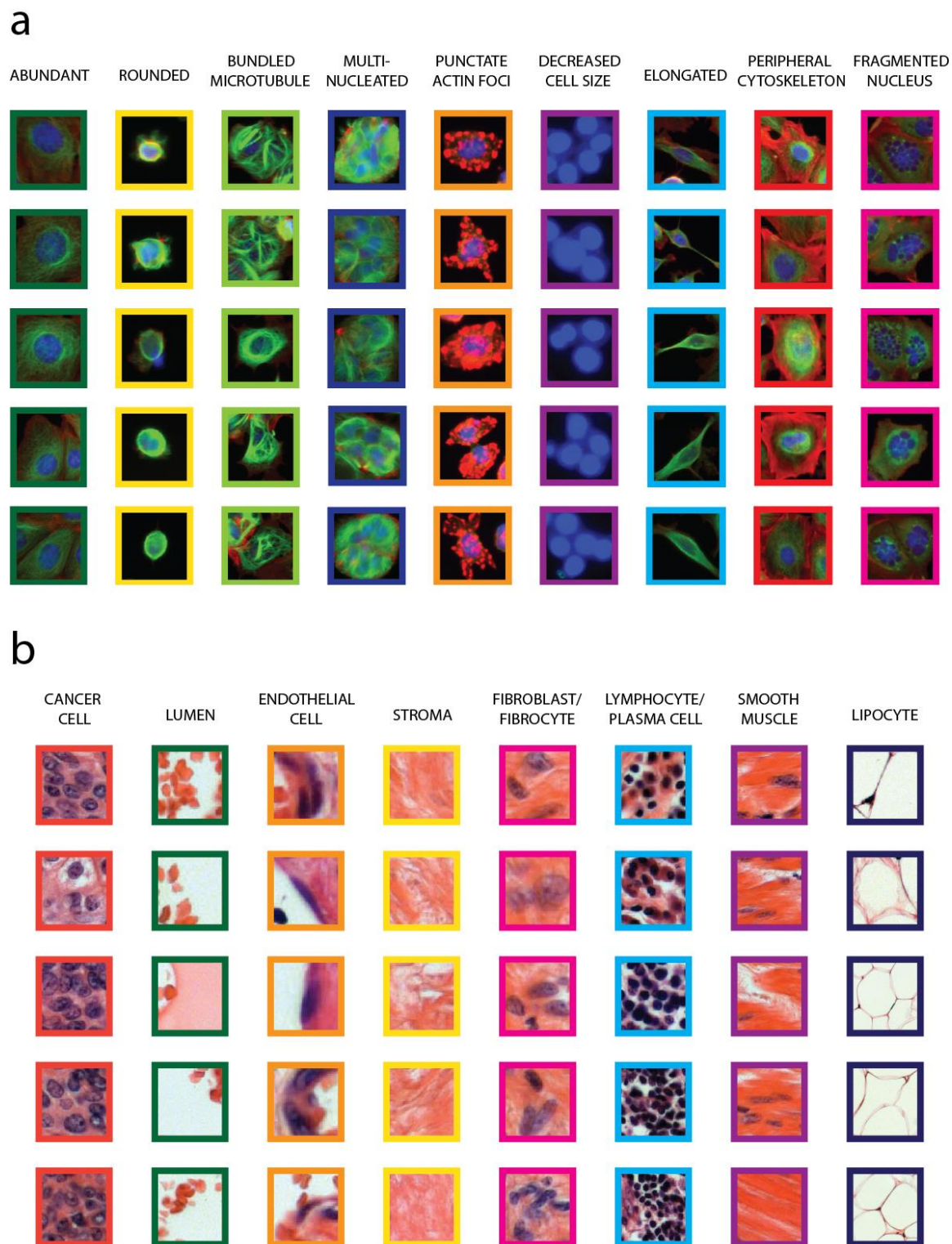
Figure 6 Distinguished phenotypes. (a) Cells of nine different phenotype classes identified in the MCF-7 High-Content-Screening Dataset. (b) Eight phenotypic classes in the UBC tissue image dataset. Figure is adapted from [6].

Table 1 Distribution of the labelled cells in the MCF-7 and the UBC datasets. Table is adapted from [6].

MCF-7 Phenotypes	Number of labelled cells	UBC Phenotypes	Number of labelled super-pixels (SLIC 25)	Number of labelled super-pixels (SLIC 35)	Number of labelled super-pixels (SLIC 50)	Number of labelled super-pixels (SLIC 75)	Number of labelled super-pixels (SLIC 100)
Abundant	307	*Cancer cell*	200	200	150	100	75
Rounded	301	*Lumen*	200	200	150	100	77
Bundled microtubule	85	*Endothelial cell*	100	100	75	55	40
Multi-nucleated	155	*Stroma*	200	200	150	100	62
Punctate actin foci	54	*Fibroblast/ fibrocyte*	200	200	150	100	62
Decreased cell size	47	*Lymphocyte/ Plasma cell*	200	200	150	100	66
Elongated	94	*Smooth muscle*	200	200	150	100	73
Peripheral cytoskeleton	124	*Lipocyte*	200	200	150	100	75
Fragmented nucleus	185	*Debris*	200	200	150	100	68
Debris	321						
Sum of labelled cells:	**1673**	**Sum of labelled superpixels:**	**1700**	**1700**	**1275**	**855**	**598**

3.4 Results

We evaluated the performance of neighbourhood features on both image sets. We compared various classification methods, took into account the size of the neighbourhood and tested whether regular features, neighbourhood features or the combination of these features produce the best results. We anticipated that the inclusion of neighbourhood features would improve the performance of machine learning based on the concordant opinion of biologists and pathologists, who highlight the relevance of cellular microenvironment. We also observed that the local features of cells can be remarkably similar, despite belonging to different phenotypic classes, but the neighbourhood features clearly distinguish them (Figure 5). We hypothesised that there is a nonzero, but not excessively big size of the environment, where classifiers work best (i.e., an optimal neighbourhood size with respect to accuracy).

3.4.1 Improved accuracy in cell culture

For the MCF-7 breast cancer cells, we selected 5–25 nearest neighbours for the KNN and 100–1200 pixels (39.025–468.3 μm) for the Euclidean distance-based analysis. According to cross-validation results, adding more neighbours increases accuracy for all classifiers (Fig. 7a). The SMO classifier displayed the best performance at a distance of 800 pixels (312.2 μm). In this instance, accuracy was 90.80%, which is 10% higher than that achieved when considering regular features only (Fig. 8a,b). An enhancement can also be seen when we compare our results to an earlier study[87], in which the MCF-7 dataset was analysed with Advanced Cell Classifier (see Supplementary Section 1).

3.4.2 Neighbourhood features have major influence on phenotyping tissue sections

In the case of the UBC dataset, we used the KNN approach with 5-3000 neighbours and the N-distance method between 100 and 1500 pixels (27-405 μm) to analyse the effect of neighbourhood features. First, we tested the RandomForest algorithm for all training sets. Figure 7b shows the cross validation results for various SLIC sizes. The best performance (90.96% accuracy) appears at superpixel size 35 (when a superpixel region is approximately 89.3 μm2) in the case of 100-nearest neighbours. Using only local features at the same superpixel size and same KNN value, accuracy reaches 83.87%. This means that the inclusion of neighbourhood features increases the performance of over 7%.

We used this preliminary information based on RandomForest calculations that superpixel size 35 could be the optimal choice and tested other supervised classification models on this size (Fig. 7c). The MLP classifier with 100-nearest neighbours produced the best accuracy (93.37%). Without the neighbourhood features, accuracy was 74.96%. The other classifiers we examined showed a similar trend: using neighbourhood features resulted in better results in each case than did relying only on regular features (Fig. 8c,d).
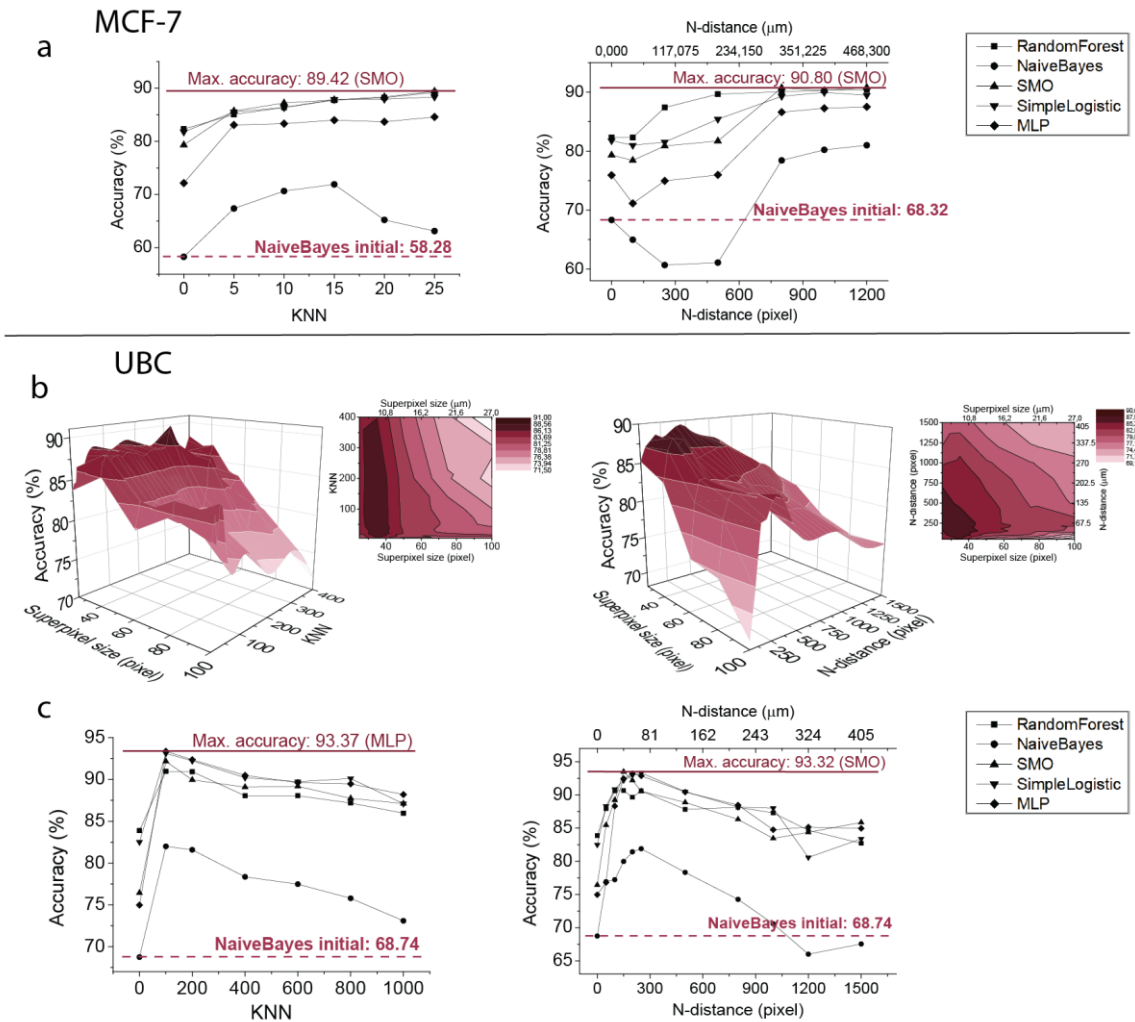
Figure 7 *Comparison of the performance of machine learning methods (RandomForest, NaiveBayes, SMO, SimpleLogistic, MultilayerPerceptron) on different neighbourhood distances. (a) Machine learning accuracies in the cell culture dataset using neighbours selected with the KNN (left) and the N-distance methods (right). (We note that principal component analysis was performed using 99% coverage before the Naïve Bayes and the Multilayer Perceptron calculations to reduce computational complexity.) (b) Three-dimensional (3D) illustration (and its contour) of the performance of the RandomForest algorithm in the UBC tissue dataset with respect to different superpixel and neighbourhood sizes using the KNN (left) and the N-distance (right) methods. (c) Machine learning accuracies on the best performing superpixel size (SLIC35, based on Figure 7b results) in the case of the UBC tissue image dataset. Figure is adapted from* [6].

29

Figure 8 *The effect of taking cellular neighbourhood into account. (a) Prediction examples based on machine learning (SMO) in the cell culture dataset. Original image (left), scale:*

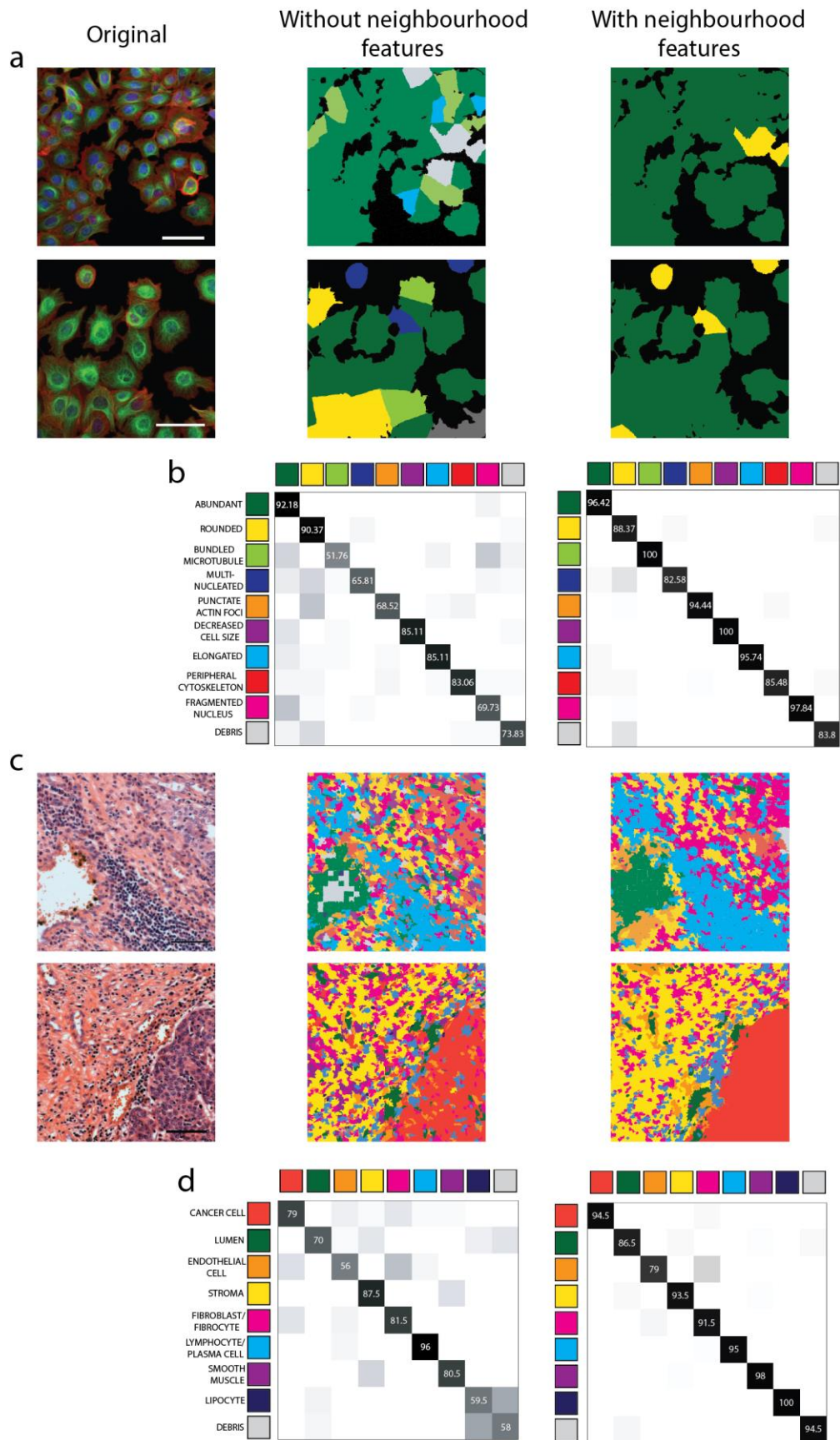*50 μm, prediction using regular features only (middle), prediction using regular and neighbourhood features, N-distance: 1200 pixels, 468.3 μm (right) (b) Confusion matrices of the best machine learning performance (SMO) in the MCF-7 breast cancer cell dataset, taking the features of single-cells into account (middle) and considering neighbourhood features (N-distance: 1200 pixels, 468.3 μm) as well (right) (c) Prediction examples based on machine learning (MLP) in the UBC tissue dataset. Original image (left), scale: 50 μm, prediction using regular features only (middle), prediction using the combination of regular and neighbourhood features, KNN, K=100 (right), superpixel size: 35 pixels (9.45 μm) (d) Confusion matrices of the best machine learning performance (MLP) in the case of the tissue section images. Calculations using base features only (middle) and taking cellular neighbourhood into account (KNN, K=100). Figure is adapted from [6].*

3.4 Conclusion

In this part of the thesis, we presented an analysis of two datasets to test our hypothesis using biological and clinical data. The first dataset used was a publicly available MCF-7 breast cancer cell line collection treated with various drugs used in medical practice. The second dataset was images of urinary bladder cancer tissue sections obtained from patient-derived samples. We extracted regular and neighbourhood features to describe the microenvironment (the local features of cells can be similar across different phenotypic classes, but neighbourhood features clearly distinguish them). We used two different approaches to get the neighbours of a cell, the K-nearest neighbours (KNN) and the N-distance methods. In conclusion, we found that the inclusion of neighbourhood features improves the accuracy of machine learning based classification in both cell culture and tissue sections (Figure 8). The optimal neighbourhood size varies based on the dataset and classifier used. The results suggest that neighbourhood features have a major influence on phenotyping tissue sections, with an increase in performance close to 20%. This information can be used to optimise the selection of neighbourhood features for machine learning classification in future studies.

4. Fisheye transformation combined with deep learning

In the previous chapter we discussed that image-based features derived from the microenvironment have an enormous impact on successfully determining the phenotype of a cell. Deep learning networks are able to process arbitrary image sizes and therefore it is technically feasible to process larger microenvironments. However, from a biological point of view it seems reasonable that the direct neighbours of a cell have a bigger impact than the cells that are farther. We wanted to illustrate this phenomenon in the input images of the networks. To achieve this, we used a distortion similar to those characteristic for fisheye cameras. With this approach we could produce images that (1) contain the fully featured view of the cell-of-interest, (2) include the neighbourhood and (3) give lesser weight to cells that are far from the cell-of-interest. In this part of the thesis we show that using the proposed transformation with proper settings, we could improve classification accuracy for both cell culture and tissue-section images. We also present that the range of potential applications of the aforementioned method goes beyond microscopy, as in the case of a dataset that contains images of wild animals, we could achieve better results compared to traditional deep-learning approaches.

4.1 Background

Researchers have utilised a combination of computer vision and traditional machine learning methods to aid in tasks such as exploring changes in cell structure during imaging-based drug screening, classifying the distribution of proteins within cells, segmenting single cells in images, and tracking objects [4, 77, 98–100]. Although these techniques were successfully used in the past, deep learning approaches tend to be more effective in recognizing biological patterns when analysing images [5, 101].

Deep learning has produced impressive results in addressing biological problems [34]. The appearance of a cell is shaped by various cellular processes and factors, including the stochasticity of gene expression, diverse proteomes and metabolomes, which contribute to its unique morphological configuration [102]. By utilising deep learning, researchers have been able to examine factors such as replicative age, organelle inheritance, and stress response [103]. Deep learning analysis methods have proven to be as effective as human pathologists in classifying whole-slide images into cancerous and normal lung tissue

categories, and even predicting the top ten most commonly mutated genes [104]. Another common challenge in cell biology is identifying proteins and determining their locations within cells. To address this issue, multiple models have been developed to automatically identify subcellular localization patterns, utilising data from the Human Protein Atlas, which comprises single-cell-level images of 12,003 human proteins [105–107].

The variability among individual cells within a population is also influenced by the microenvironment of each cell [92, 93]. Research has shown that the unique characteristics of the cellular neighbourhood can play a critical role in understanding the collective organisation of cells in various contexts. For example, Snijder et al. have reported that in a cell culture setting, the burden of viral infection at the single-cell level can be predicted based solely on each cell's microenvironment [93]. Bove et al. found that in a study of competition between normal Madin-Darby canine kidney (MDCK) cells and cells lacking the polarity protein scribble, the likelihood of cell division was significantly higher for MDCK cells when their neighbourhood was mostly comprised of scribble cells [108]. There are numerous other examples in the literature of the importance of cellular neighbourhood, such as neighbouring epidermal stem cells affecting each other's differentiation, and the size difference of ligand-producing hair cell precursors in the inner ear compared to their neighbours [109]. As it was shown in the previous chapter of the thesis, our group has also concluded that incorporating the features of a cell's microenvironment improves phenotype classification in high-content screens [6]. Based on these findings, we believe that incorporating environmental data into deep learning phenotypic profiling is worth exploring.

Recently, fisheye cameras have gained significant attention from both technical experts and the general public. These cameras use ultra-wide angle lenses that are capable of capturing panoramic or hemispheric images, but they introduce significant optical distortion into the process. Specific mapping techniques (such as stereographic, equidistant, equisolid angle, or orthogonal) are utilised by fisheye lenses, which give the resulting images a characteristic convex, non-rectilinear appearance [110]. Due to their ability to provide rich visual information, fisheye lenses have a wide range of applications, including generating augmented or virtual reality, improving the performance of intelligent robot vision systems, and simplifying the complexity of surveillance systems [111–113].

To rectify the distortion introduced by fisheye lenses, various correction models have been proposed [114–116].

In this part of the thesis, we propose a new approach to represent images for deep learning-based image classification networks. The approach involves using a fisheye-like spatial sampling method to transform the original image, which contains the object of interest in the centre along with its predefined microenvironment. The transformation collects more pixels from the proximity of the object-of-interest and decreases the resolution for larger proximity (Fig. 9b). The results show that the proposed pipeline outperforms classical machine learning methods and deep learning-based classifiers on different datasets, such as cell cultures, scans of cancerous tissues, and real-life images. The fisheye transform method achieves higher accuracy scores on the datasets compared to using multi-scale images in parallel (i.e. an image pyramid) for the network. Moreover, the fisheye transformation can be incorporated into the network as a layer, although it requires more computational resources when large images are fed into the network [117].
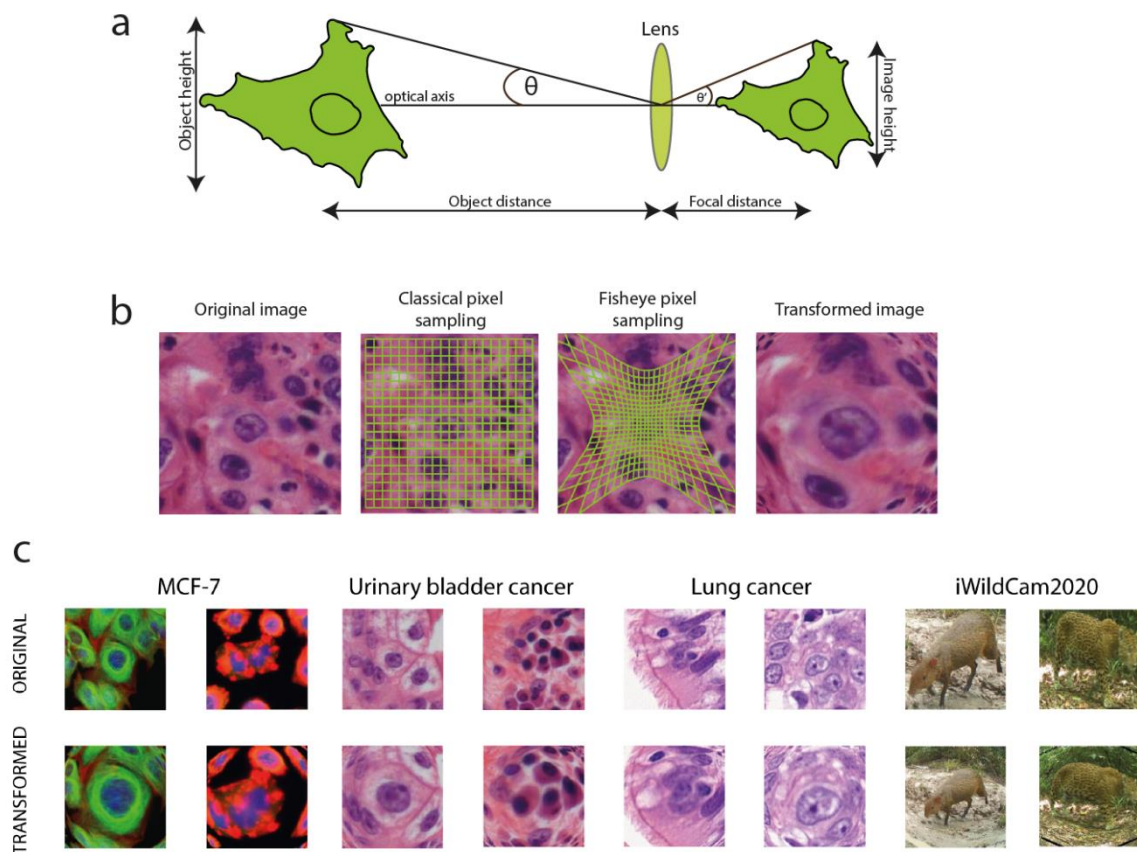

Figure 9 Fisheye transformation. (a) Illustration of the optical parameters for the fisheye transformation. (b) The difference between classical and fisheye pixel sampling: in the

classic case we select pixels evenly, while in case of fisheye, sampling is dense near to the object-of-interest, and less dense as the distance from the object increases. (c) Examples of the fisheye transformation. Figure is adapted from [7].

4.2 Datasets

4.2.1 MCF-7 cell culture

As a cell culture dataset, we used the same set we described in section 3.2.1. To see examples of the distinguished phenotypic classes, see Fig. 10a.

4.2.2 Urinary bladder cancer tissue sections

We used our previously described (section 3.2.2.) urinary bladder cancer (UBC) tissue dataset. Refer to Fig. 10b to observe instances of the distinguished phenotypic classes.

4.2.3 Lung cancer tissue sections

We used images of lung cancer (LC) tissues as a test dataset (Fig. 10c). The images were acquired from patient-derived samples were obtained from University of Szeged (approval authorisation number: 5127, registration number: 17/2022-SZTE). The samples were obtained from 4 patients (sex and gender identity/age/histological observations of the subjects respectively: female/75/primary pulmonary multinodular invasive papillary adenocarcinoma, female/65/primary lung origin, acinar predominant adenocarcinoma, female/74/primary lung origin, invasive adenocarcinoma, acinaris predominant, male/76/primary lung origin, invasive solid adenocarcinoma).

The slides of lung cancer tissues were stained with HE in standard histopathological procedures. Formalin-fixed and paraffin-embedded tissue sections were cut into 4 µm thick slices, and were stained using a Tissue-Tek DRS 2000E-D2 Slide Stainer (Sakura Finetek Japan) according to the manufacturer's instructions. Using the AxioVision SE64Rel.4.9.1.1 (Carl Zeiss Meditec AG, Germany) software, images were captured with

an Axio Imager Z.1 (Carl Zeiss Meditec AG, Germany) microscope equipped with an EC Plan-NEOFLUOAR 20x/0.5NA lens.

For this dataset, we differentiated 10 phenotypic classes (blood cell, cancer cell, cartilage, endothelial cell, epithelium, fibroblast-fibrocyte, gland, lymphocyte-plasma cell, muscle cell and stroma cell, see Fig. 10c), and labelled 5,000 cells.
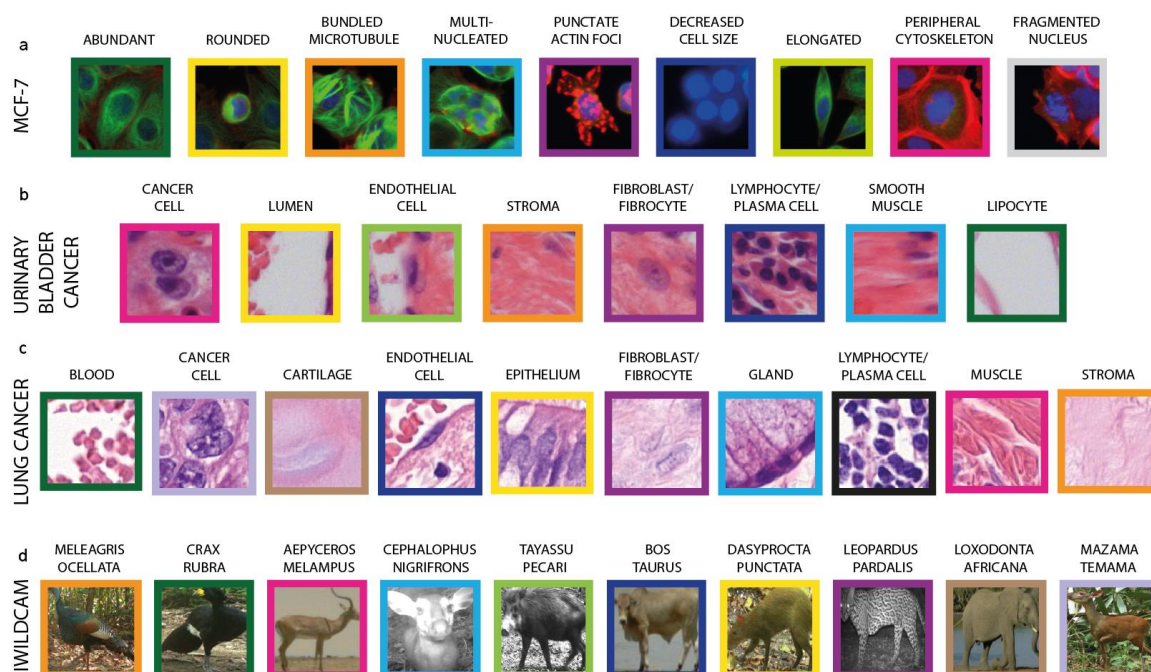
Figure 10 *Distinguished classes. (a) Cells of nine different phenotype classes identified in the MCF-7 High-Content-Screening Dataset. (b) Eight phenotypic classes in the UBC tissue image dataset. (c) Ten phenotypic classes in the LC tissue image dataset. (d) The ten most common animal species in the iWildCam2020 dataset. Figure is adapted from* [7].

4.2.4 iWildCam 2020 dataset

The iWildCam 2020 dataset was created from a Kaggle competition that was centred on the task of categorising different animal species. The Wildlife Conservation Society, iNaturalist, the U.S. Geological Survey, and Microsoft AI for Earth were the primary sources of data. The training dataset for the competition is composed of 217,959 pictures taken at 441 sites, and it contains 267 categories, which have an uneven number of examples. The top 10 classes that include the majority of the examples (excluding the 'empty' category, which has no visible animals in the picture) are shown in Fig. 10d.

4.3 Methods

4.3.1 Segmentation

The segmentation we used for the MCF-7 and UBC datasets is described in section 3.3.2.

Similar to the UBC dataset, the SLIC superpixel segmentation technique [78] was employed to segment urinary bladder cancer and lung cancer section images. In this case, a superpixel size of 35 pixels was used, and connectivity was enforced between superpixels with less than 25 pixels. Our previous research has shown that this superpixel size is most effective for representing cells [6].

While annotating the MCF-7, urinary bladder, and lung cancer datasets, we recorded and saved the x-y coordinates of the nuclei/superpixels' centres. These coordinates were then utilised as inputs for the fisheye transformation.

The iWildCam dataset was accompanied by a general animal detection model called MegaDetector (https://github.com/microsoft/CameraTraps/blob/master/megadetector.md) and an annotation file with one label per image, provided by the Kaggle competition organisers. In cases where multiple animals appeared in an image, we selected the detection with the highest accuracy and used its label. MegaDetector utilises bounding boxes, and for our study, we used the x-y coordinates of the bounding box centres as inputs for the fisheye transformation.

4.3.2 Fisheye transformation

A range of ultra-wide angle lenses exist, all of which introduce a notable visual distortion. In our investigation, we assessed an algorithm that artificially replicates this distortion present in images captured using ultra-wide angle lenses. We examined the importance of nearby features to identify the optimal distance for achieving the highest classification accuracy.
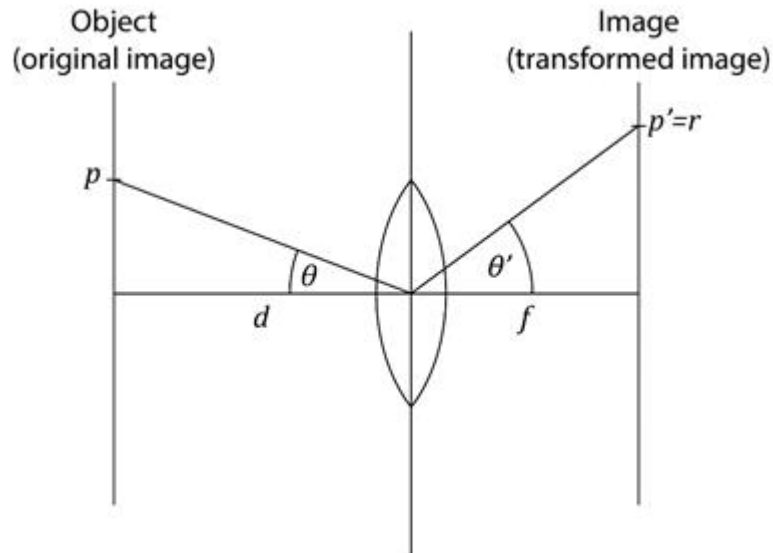
The projection position of a given real world point in fisheye transformation can be determined based on the angle of the incident ray. This can be calculated using a mapping function:

$$r = m(f, \theta),$$

where f is the focal length. For a given f we can reformulate the above equation as

$$r = m_f(\theta).$$

The mapping function is an essential component of fisheye lenses that determines the position of an object (r) in the image relative to the centre, based on the focal distance (f) and the angle (θ) from the optical axis. The functions in wide-angle lens cameras include the following:

- Rectilinear:

$$r = f \tan \theta$$

- Fisheye

    - Equidistant

    $$r = f\theta$$

    - Equisolid angle

    $$r = 2f \sin \frac{\theta}{2}$$

    - Stereographic

$$r = 2f \tan \frac{\theta}{2}$$

- Orthographic

$$r = f \sin \theta$$

All of these functions are invertible:

$$\theta = m_f^{-1}(r).$$

The following relation is also valid for θ:

$$\tan \theta \; = \frac{p}{d},$$

where d is the distance between point p and the centre of the lens, measured along the axis of the lens. In our case, the pixels of an image represent the object points, and the constant d remains the same throughout the entire image.

In tasks that involve transforming images, the transformation function is typically expressed as an inverse mapping, which specifies the source position of every output pixel. In other words, it determines the value of p for each output position r. From the equations above, p can be calculated as follows:

$$p = d \cdot \tan m_f^{-1}(r) \,.$$

This equation contains two free parameters: d and f. The scalar multiplier d only impacts magnification. The value of f affects both the scale and magnitude of distortion. However, in our study, we aimed to adjust the fisheye effect of the transformation without changing the scale of the selected area. To achieve this, we connected the value of d and f in a way that preserves the scaling.
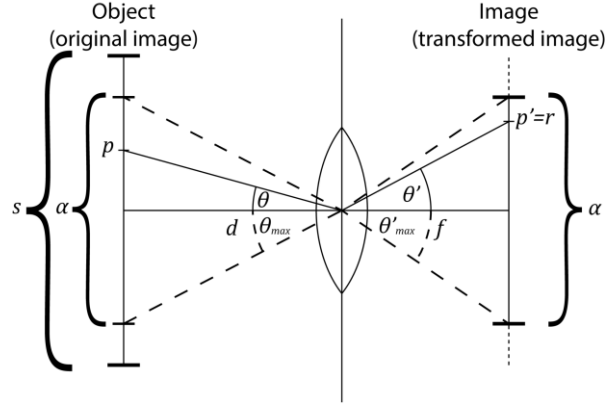
Let's mark the size of the selected area with α. Our objective is to maintain the original position of the corner points even after the fisheye distortion is applied. In this case an equation is introduced as follows:

$$tan\ \theta_{max} = \frac{\alpha}{2d},$$

where θ_{max} is the angle of the incoming ray from the borders of the selected area. As for the border points are expected to be transformed into themselves,

$$\theta_{max} = m_f^{-1}\left(\frac{\alpha}{2}\right)$$

is also valid. Combining these two equations gives

$$d = \frac{\alpha}{2\ tan\ m_f^{-1}\left(\frac{\alpha}{2}\right)}.$$

It is evident that the last equation is determined by f as a modifiable parameter (when the value of α is fixed). Thus, the final form of the equation for the fisheye transformation is

$$p = \frac{\alpha}{2} \cdot \frac{tan\ m_f^{-1}(r)}{tan\ m_f^{-1}\left(\frac{s}{2}\right)}.$$

As an easy-to-read interpretation, we normalise the value of θ to the range of $[0, 1]$, and then rescale it to the range $\left[0, \frac{\alpha}{2}\right]$.

40

Note that in the calculations above it is assumed that the selected area of interest is in the middle of the image. However, with a simple translation, the calculations are valid for any arbitrary image positions.

The first parameter that we optimised was the window size, which refers to the range around our object of interest (i.e., the object height in optical terms, as shown in Fig. 9a). For the MCF-7, UBC, and LC datasets, we previously saved the x-y coordinates of the nuclei/superpixels centre, and then applied the selected pixel range for fisheye transformation based on these coordinates. For the iWildCam dataset, we cropped the areas of interest from the original images in four different sizes for fisheye transformation. We multiplied the size of the original bounding box by 1.0, 1.5, 2.0, and 2.5. When we multiplied the original size by 1.0, we cropped the images to the same size for both the baseline and fisheye-transformation images. For all other cases, we considered a larger environment size.

The second adjustable parameter we optimised was the focal distance, which determines the extent of the distortion. Unlike for the analyses based on our original idea of acquiring information based on cell neighbourhood, we used pixel-based information acquisition (Fig. 4, 9b). The third parameter we optimised was the mapping function, which in cameras is responsible for transforming a portion of a spherical object into a 2D plane. In this study, we selected the "equidistant" function, which is one of the most common mapping functions used in cameras, to test our hypothesis on the significance of neighbourhood in classification accuracy. We set the object distance (the distance between the original image and the lenses) to eliminate scaling due to fisheye distortion in all cases. For additional examples of transformed images, see Supplementary Figure S1-S4.

4.3.3 Deep learning-based object classification

Matlab R2019b and its Deep Learning Toolbox (version 13.0) were employed for image classification in this study. The toolbox offers a platform to develop or implement networks, pre-trained models, and apps. Two pre-trained networks on ImageNet, ResNet50 and InceptionV3, were utilised for transfer learning due to their accuracy, speed, and size. To avoid any possible positive influence of evaluation, annotated cells were excluded from the validation image as a neighbour in the training dataset of MCF-7 and UBC datasets.

Instead, the training dataset was pre-defined at the image level. In contrast, LC and iWildCam datasets only contained one annotated object per image, and were randomised and split into 80% for training and 20% for validation. Data augmentation was performed on the training datasets using standard geometry transformations such as reflection in the left-right and a top-bottom directions, rotation, horizontal and vertical scaling. However, we did not use any transformations that would move the cell-of-interest away from the centre of the image, as this would impact the fisheye transformation.

The deep-learning parameters used: MiniBatchSize: 64, MaxEpochs: 100, InitialLearnRate: 3e-4, LearnRateDropFactor: 0.3, LearnRateDropPeriod: 50, Shuffle: every epoch.

4.4 Results

We assessed the effectiveness of a fisheye-inspired sampling approach in enhancing deep learning-based image classification networks, using several image datasets (Figure 10). We compared ResNet50 and InceptionV3-based classifiers, and examined the impact of neighbourhood extent and focal distance of the fisheye transformation. Our aim was to determine the best combination of these parameters that would produce the most accurate results.

We used ResNet50 and InceptionV3 models as baselines for comparison. For the cell culture and tissue section datasets, we cropped out 192x192 pixel-sized images around the cells' centres and resized them to 224x224 to meet the models' requirements. For the iWildCam dataset, we cropped out the bounding boxes around the animals and resized them to 224x224 pixel images. We did not use fisheye transformation for benchmarking. We performed two-sample t-tests for statistical analysis of the classification accuracy results (see Supplementary Section 2).

Based on previous studies in cellular biology, we hypothesised that considering the cell's microenvironment would enhance deep learning classification performance. To test this, we introduced a fisheye transformation, which takes into account more pixels from the object-of-interest's direct neighbourhood than from the surrounding region (Fig. 9b). We

also hypothesised that there would be an optimal combination of neighbourhood range and focal distance for deep learning-based classification accuracy.

4.4.1 Increased classification accuracy on images of cell cultures

For the MCF-7 breast cancer cell dataset, we defined an environmental range of 45 to 724 pixels (17.56-282.54 µm). The average nuclei size in this dataset is 37 pixels (14.44 µm). Validation results indicate that the accuracy of both ResNet50 and InceptionV3 classifiers improves when applying the fisheye transformation (Fig. 11a). The best performance was achieved with the ResNet50 model using a window size of 543 pixels (211.91 µm) and a focal length of 130 arbitrary units. This resulted in an accuracy of 91.38%, which is 7% better than deep learning alone (84.31%). Our previous results with classical machine learning approaches showed a maximum accuracy of 90.80% with the support vector machine classifier, which was outperformed by the highest classification accuracy achieved with fisheye distortion. Although InceptionV3 had a higher deep learning baseline (85.85%) than ResNet50, the best result we achieved with InceptionV3 using distorted images was only 89.33%.

We also segmented nuclei and cytoplasm in the MCF-7 dataset and tested the effect of including the environment and the fisheye transformation on classification accuracy. We used the same ResNet50 network for both the baseline and fisheye calculations. The results show that the accuracy is lowest when the network sees only the nuclei, and highest when using fisheye transformed images that include the cell's microenvironment (see Figure S5-S6).
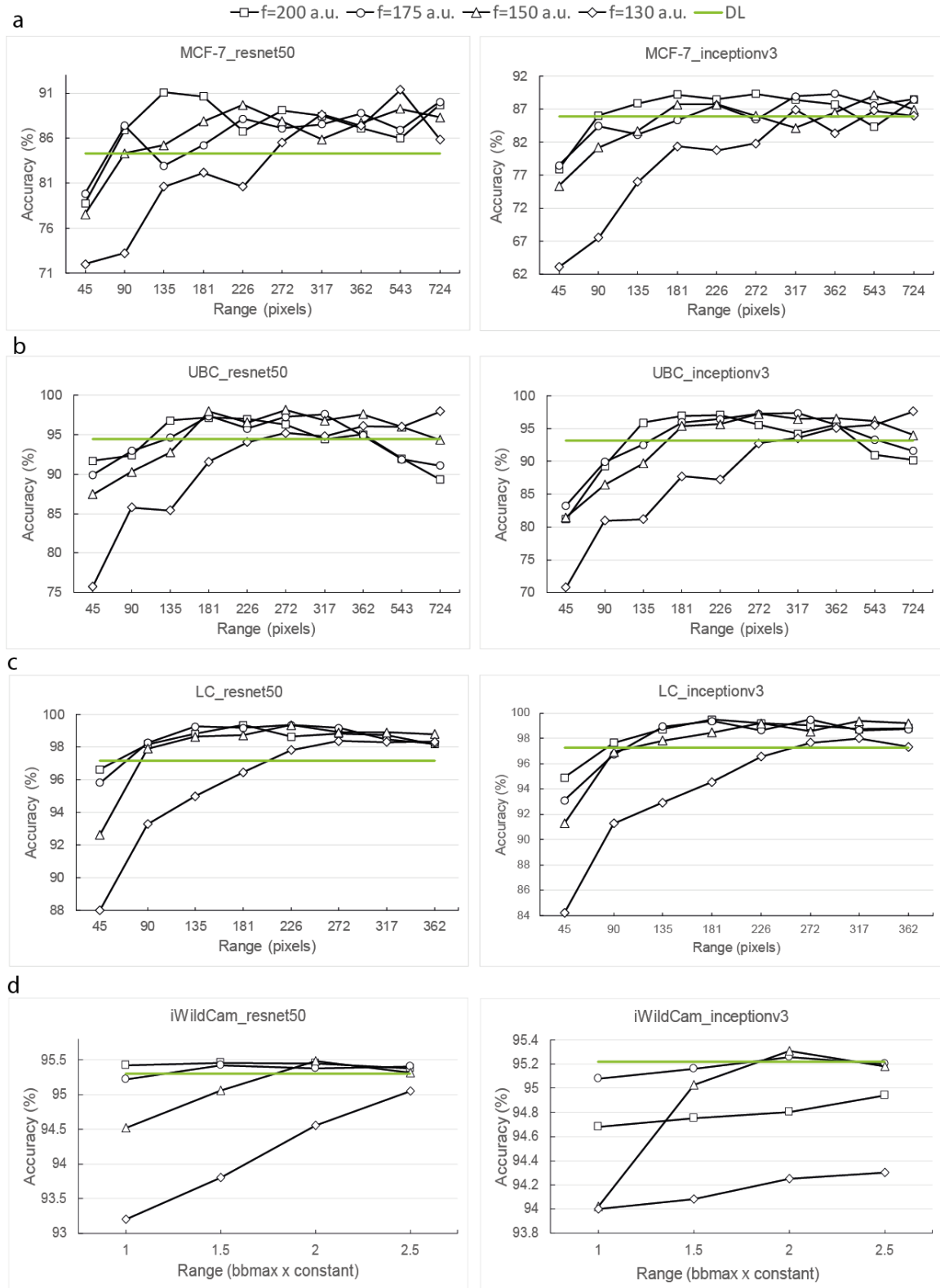
Figure 11 *Comparison of the performance of deep learning networks (ResNet50, InceptionV3) upon considering different neighbourhood distances. (a) Classification accuracies for the MCF-7 cell culture dataset using ResNet50 (left) and InceptionV3 (right). (b) Classification accuracies for the urinary bladder cancer tissue image dataset. (c) Classification accuracies for the lung cancer tissue dataset. (d) Classification accuracies for the iWildCam2020 dataset. Green lines indicate the baseline yielded with*

deep learning upon using the original (undistorted) images, while black lines indicate the results achieved on fisheye distorted images with different f (focal distance) values (the values are measured in arbitrary units). Figure is adapted from [7].

4.4.2 Fisheye transformation has a major impact on phenotyping tissue sections

In the UBC tissue image dataset and the lung cancer dataset, we collected neighbourhood information for window sizes of 45 to 724 pixels (12.15-195.48 µm) and 45 to 362 pixels (17.55-141.18 µm), respectively. The average nuclei sizes for these datasets were 32 pixels (8.64 µm) and 39 pixels (15.21 µm), respectively. Our results indicate that using the fisheye transformation improved classification accuracy compared to traditional deep learning, regardless of whether we used ResNet50 or InceptionV3.

In our previous study on the UBC dataset, we achieved a maximum classification accuracy of 93.37% with MLP calculations using neighbourhood features. In our current study, using the fisheye transformation with ResNet50, we achieved a best performance of 98.14% with a window size of 272 pixels and a 150 arbitrary unit focal length (Fig. 11b). Without using the distorted images, classification accuracy was 94.41% only. For the lung cancer dataset, InceptionV3 performed slightly better than ResNet50, with a maximum accuracy of 99.46% achieved by incorporating the neighbourhood feature with a 272 pixel range and using 170 arbitrary units as focal distance. This is more than 2% better than the results yielded with InceptionV3 on undistorted images (accuracy: 97.25%).

4.4.3 Fisheye transformation outperforms image pyramids

To compare the performance of our proposed fisheye transformation with classical multiscale approaches, we conducted a benchmark test on the UBC and LC datasets using an image pyramid as input for the networks. We provided ResNet50 networks with images of different scales (1/1, 1/2, 1/4) simultaneously. The phenotypic classification accuracy was 97.9% for the UBC dataset and 99.1% for the lung cancer dataset. These results show that using the image pyramid approach produces better outcomes than traditional deep learning. However, it is not as effective as the fisheye transformed approach.

4.4.4 Improved accuracy in case of the iWildCam2020 dataset

Our study aimed to determine whether incorporating environmental information from real-life scenes could enhance the accuracy of classification results. The dataset comprised photographs of animals captured from stationary camera positions. As the perspective varied, the animals appeared either small or large in the images. To address this disparity, we utilised the size of the bounding boxes surrounding the animals as references, rather than using fixed pixel-distances. The deep learning baselines for classification accuracy were 95.3% and 95.22% for ResNet50 and InceptionV3, respectively. However, when fisheye-transformed images were used, classification accuracy improved to 95.48% with ResNet50, using 2.0× the size of the bounding boxes as the neighbourhood feature and a focal length of 150 units.

4.5 Conclusion

In this chapter, we proposed a new method that combines fisheye transformation with deep learning to improve phenotypic classification accuracy. We tested our method on various datasets, including MCF-7 cell culture, urinary bladder cancer and lung cancer tissue sections, and iWildCam2020. Our approach outperformed traditional machine learning methods that used single-cell and neighbourhood features, as well as deep learning models that used non-fisheye transformed images as input (Figure 12).

The most significant improvement was observed in the tissue section images, where microenvironmental differences are apparent. These differences are evident in the histology studies of tissues, where the cooperation and interdependence of different cells are visible. Our method captures these differences by using the fisheye transformation and considers the adjacency information of endothelial cells and the presence of restricted cell types such as connective tissue cells and smooth muscle cells.
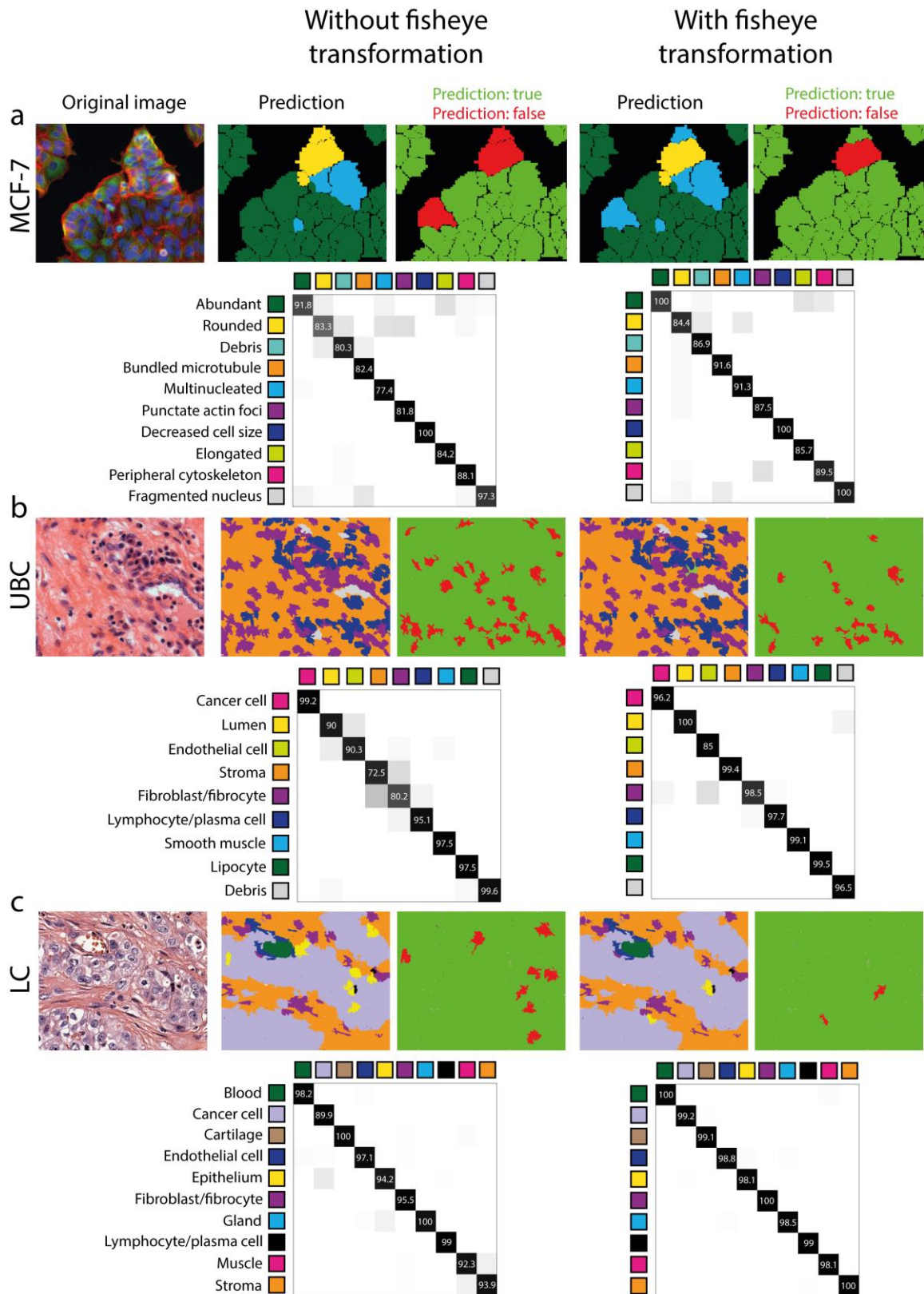
Figure 12 *The effect of combining the fisheye transformation with deep learning. (a) Prediction examples and confusion matrices based on ResNet50 models in the cell culture dataset. Original image (left), prediction and confusion matrix using the model built on standard images (middle), prediction and confusion matrix using the model built on*

fisheye-transformed images, window size: 543 pixels, focal length: 130 a.u. (right). In the second and fourth images we show with different colours the predicted phenotypes and in the third and fifth images we show if the prediction was true (green) or false (red). (b) Prediction examples and confusion matrices of the best deep learning performance (ResNet50) in the urinary bladder cancer tissue dataset. Original image (left), prediction and confusion matrix using traditional deep learning (middle) and considering the cellular neighbourhood with fisheye transformation, window size: 272 pixels, focal length: 150 a.u. (right). (c) Prediction examples and confusion matrices based on InceptionV3 models in the lung cancer tissue dataset. Original image (left), prediction and confusion matrix using the model built on undistorted images (middle), prediction and confusion matrix using the combination of deep-learning and fisheye-distorted images, window size: 272 pixels, focal length: 170 a.u. (right). Figure is adapted from [7].

We also observed an improvement in accuracy in the case of cell cultures. Though there are homogeneous-looking areas in these images, they are not composed of molecularly identical cells. Here, the fisheye transformation helps capture the differences in these regions, and the neighbourhood provides a more statistically stable basis for decision making.

While we observed only minor improvements in accuracy in the iWildCam dataset, we demonstrate that the fisheye transformation approach is generally applicable to any image data where the environment plays an important role.

In conclusion, our study shows that incorporating the microenvironment into machine-based decisions can improve phenotypic classification accuracy. This highlights the importance of considering macro structures in cellular structures. We also demonstrate that non-uniformly sampling the original image data for deep learning training and inference is feasible and can further improve accuracy. A potential extension to our approach could involve introducing data transformer layers that can learn non-linear spatial sampling functions.

5. Analysis of 3D cell cultures

In the previous chapters, we talked about improving machine learning accuracy for 2D images by considering the neighbourhood of the cell of interest. Now, we turn our attention to 3D cell cultures. Despite recent developments in the analysis of 3D data, a number of methodological challenges remain unresolved. So in this chapter we will focus not only on phenotypic classification, but also on the steps that precede it. These steps include sample generation, image acquisition, annotation and segmentation. We will discuss how to improve the quality of microscopy images using optical clearing and quantify the effectiveness of different clearing protocols. Then, we will discuss the challenges and solutions for annotating and segmenting cells in 3D. Finally, we will share our results so far in studying cells and their microenvironment in 3D co-cultures.

3D cell cultures refer to cell models where cells are grown in three-dimensional structures, as opposed to traditional two-dimensional monolayer cultures. 3D cultures have numerous applications in anticancer drug screenings and toxicology studies. Extensive research has shown that these 3D cell cultures are more reliable than the classical flat (2D) cell cultures (as described in Chapter 1). Culturing cells in a 3D manner offers multiple benefits compared to 2D cell culture, as it enables the expression of extracellular matrix components and facilitates interactions between cells and the matrix, as well as between cells themselves [118].

We can define different types of 3D multicellular models based on their geometry and functional complexity [66]:

- *Multicellular aggregate*: a 3D cell cluster free from a defined structural obligation

- *Spheroid*: a type of multicellular aggregate that is almost spherical in shape

- *Tumoroid*: a spheroid composed of cancer cells

- *Co-culture spheroid*: a spheroid that is composed of more than one cell type not accomplishing a specific function together

- *Microtissue*: a 3D multicellular aggregate that includes multiple cell types that work together to perform a specific function

- *Organoid*: a self-renewing multicellular aggregate that has an irregular shape and self-organise into *ex vivo* mini-organs

5.1 Related methods

5.1.1 Optical clearing and a quantitative metric to measure its effectiveness

Confocal and light sheet-based fluorescence microscopy are widely used to acquire images of single cells of spheroids [119]. However, in these models, imaging depth is significantly restricted due to the scattering of the excitation and emission lights. This scattering leads to a loss of fluorescence intensity and contrast, practically limiting the screening of cells to the outer layer of the spheroids only. The primary reason behind this light scattering effect is the presence of refractive index (RI) discontinuities between and within spheroids [120]. To address this issue, numerous optical clearing protocols have been developed [121].

Optical clearing is a process that makes biological samples, such as cells, tissues, or even whole organisms, optically transparent [122]. It is a crucial technique for biological imaging as it allows scientists to visualise the complex structures and connections within these samples in three dimensions, without the need of tissue sectioning approaches that can introduce artefacts. This technique is particularly valuable in the fields of neuroscience, developmental biology, and cancer research, where understanding the intricate three-dimensional organisation of cells and tissues is essential [123].

There are a variety of optical clearing methods, each with its strengths and drawbacks. However, the primary objective of most of these methods is to enhance the transparency of samples chemically, by equilibrating the RI throughout the sample. The process of optical clearing typically involves several steps, although the specific methods can vary depending on the application and the type of sample being studied. Here's a general overview of the optical clearing process [124]:

1. *Fixation*: The first step involves fixing the biological sample. Fixation helps preserve the sample's structural integrity and prevents degradation. Different fixatives may be used depending on the specific experiment's requirements.

2. *Dehydration*: In this step, water is removed from the sample using a series of alcohol solutions with increasing concentrations. Dehydration helps prevent the sample from swelling when it comes into contact with the clearing agent.

3. *Clearing*: The most critical step is the application of a clearing agent, which replaces the sample's water and lipids. The clearing agent has refractive properties similar to the biological sample, reducing light scattering and making the tissue transparent.

4. *Staining and labelling* (optional): Depending on the research objectives, the cleared sample can be stained or labelled with fluorescent markers or antibodies to highlight specific structures or molecules of interest.

5. *Imaging*: Once the sample has been successfully cleared, it can be imaged using various microscopy techniques, such as confocal microscopy or light-sheet microscopy. The ability to image the sample in three dimensions allows researchers to gain insights into complex cellular and neural networks, which would be challenging with conventional two-dimensional imaging.

While clearing protocols are being increasingly utilised for 3D cultures in cellular phenotyping assays [125, 126], quantitatively evaluating their effectiveness remains a challenging task. Qualitative and quantitative measures are used in most recent studies to assess the effectiveness of clearing [127–129]. During qualitative approaches, based on images that were taken with brightfield and fluorescence microscopy before and after optical clearing, most of the researchers applied subjective scoring [130]. While this method is suitable when determining the presence or absence of fluorescent signals after the clearing process or when distinguishing different clearing protocols based on brightfield images, it becomes time-consuming and impractical when comparing hundreds of 3D images.

In our work [8], we presented the development and comparison of metrics designed to measure the efficiency of optical clearing protocols for 3D images in a standardised manner. We evaluated seven metrics commonly used to assess blurriness in general photos and videos (namely intensity variance, gradient magnitude variance, Laplacian variance, histogram thresholding, histogram entropy, frequency thresholding and Kurtosis) and implemented them into an easy-to-use open-source ImageJ/Fiji [131] plugin called Spheroid Quality Measurement (SQM).

To test the performance and usability of these metrics, we created and shared a dataset [132] containing 90 spheroids derived from three different human carcinoma cell lines (T-47D: human breast cancer, 5-8F: human nasopharyngeal carcinoma, Huh-7D12: human hepatoma). In order to make the spheroids more comparable to each other, we paid special attention to generate them with a nearly identical size (200 to 250 µm in diameter). We cleared all three types of spheroids with five popular water-based clearing protocols, namely Clear^T [133] Clear^{T2} [133] CUBIC [132, 134], ScaleA2 [135] and Sucrose [132, 136]. In Figure 13 we could see the qualitative comparison of the cleared spheroids.
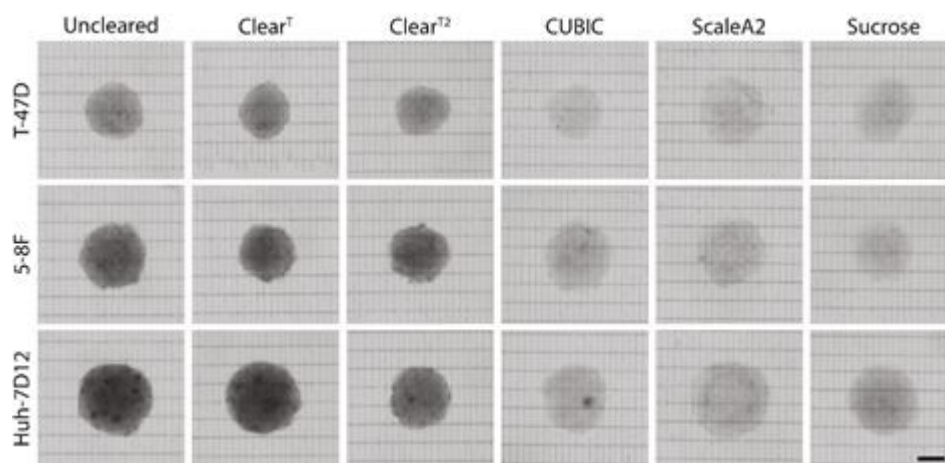

Figure 13 Qualitative comparison of cleared spheroids. Brightfield images of the different cleared spheroids on glass slides with a grid of parallel black lines. The scale bar represents 100 µm. Figure is adapted from [132].

We asked ten microscopy experts - each with a minimum of 5 years of experience in microscopy and working with spheroid images – to evaluate the 3D dataset (in Figure 14 we could see examples of the images, the experts had to examine). Their task was to visually assess the sharpness of the images. We considered their assessment as ground truth. Then, we compared the correlation between their evaluation and the results of the metrics. We found that out of the seven metrics examined, only intensity variance proved suitable for quantitatively measuring and assessing different optical clearing protocols. Finally, to measure the efficacy of the clearing protocols, we used intensity variance metric and identified the best clearing protocols for each cell line. As anticipated, the tested optical clearing protocols exhibited varying performances on the three cell lines. For the T-47D

cell line, which formed the least compact spheroids, the Sucrose, CUBIC, and ScaleA2 protocols demonstrated equal effectiveness, resulting in no significant quality differences among the cleared groups. The ScaleA2 clearing protocol provided the best image quality for the 5-8F spheroids. Finally, the Huh-7D12 cell line only showed successful visualisation of single nuclei in the lower regions of the spheroids when using the Sucrose clearing protocol.
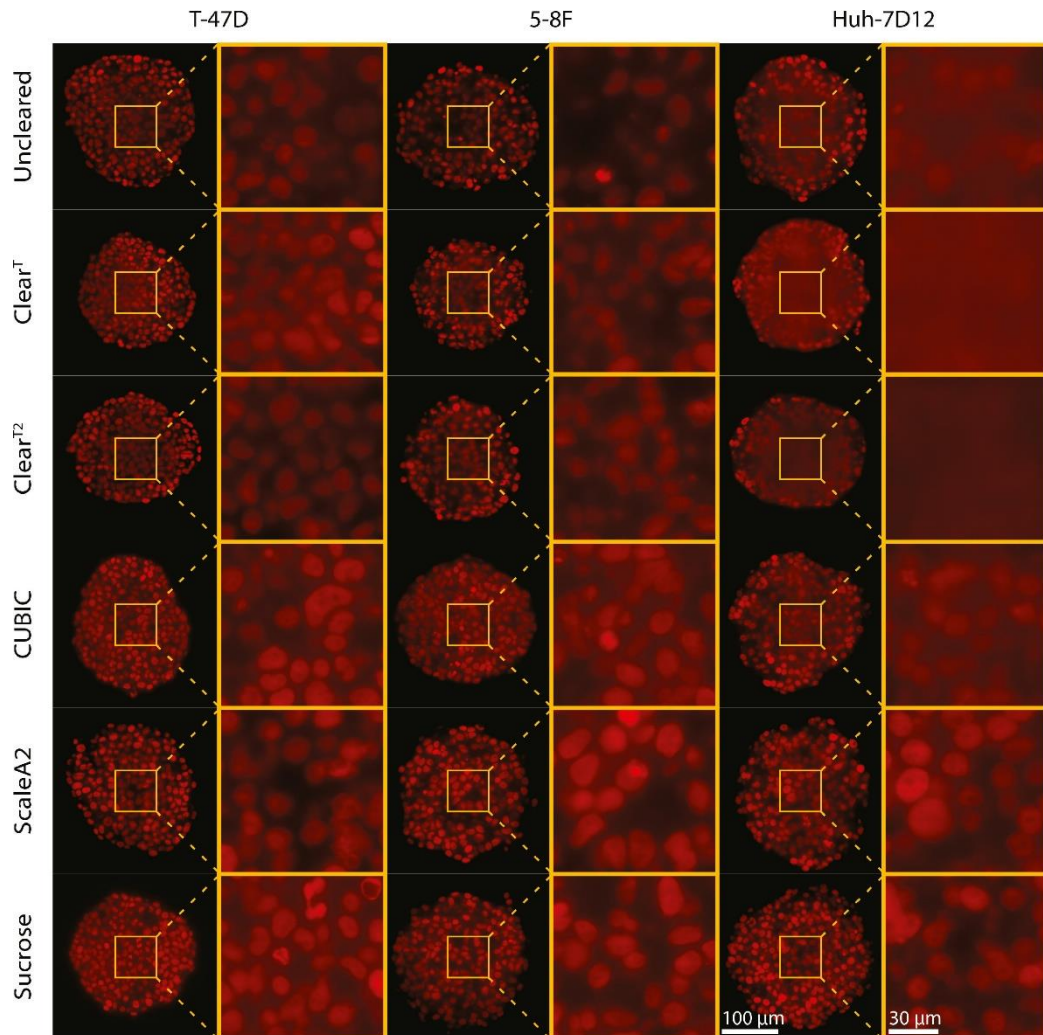

Figure 14 *Comparison of the optical clearing protocols on nuclei-labelled fluorescence images, showing the middle region of the spheroids. Figure is adapted from* [132].

5.1.2 3D nuclei annotation

One of the biggest challenges in computational biology is the segmentation of single cells in microscopy images. Segmentation is the first step in analysing cell cultures before

further phenotype-based statistics and other bioimage analysis tasks can be performed. Studies have demonstrated that deep learning-based systems significantly surpass classical image processing techniques when it comes to 2D nuclei segmentation [51]. However, these approaches require precise and large training datasets (for the segmentation of 3D cell cultures the training data contains 3D-annotated spheroids). Generating such ground truth datasets in 2D often involves manually drawing cell contours on a 2D canvas. Likewise, the natural progression to 3D would entail annotating each slice of the volume data. However, it is not difficult to see that this approach is extremely time-consuming. In addition, when annotating slice by slice, the human eye may not be able to find the exact boundary of the objects, which could lead to discontinuous object surfaces, which is against our goal to create the most accurate training dataset.

To overcome these issues, we designed 3D-Cell-Annotator [9] (Figure 15), offering an alternative method for accurately outlining 3D shapes through the utilisation of a specialised active surface model [137]. This tool is a patch for the segmentation plugin of the widely used Medical Imaging Interaction Toolkit (MITK) [138]. Due to the computational complexity and high cost of active surface models, our approach was specifically designed to leverage Graphics Processing Units (GPUs) and implemented within the NVidia CUDA framework. This implementation resulted in a considerable speed boost, several orders of magnitude faster compared to traditional CPU implementations.
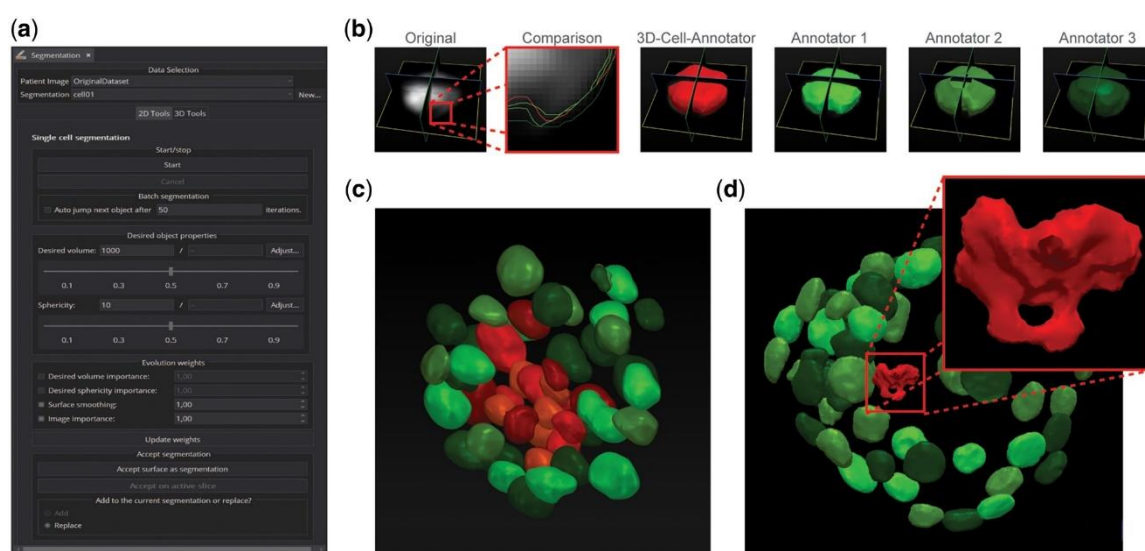

Figure 15 *3D-Cell-Annotator (a) 3D-Cell-Annotator graphical user interface. (b) Confocal single-cell dataset annotated by three experts. Despite the fact that the*

annotators are all experts in the field, the obtained segmentations slightly differ (green contours). However, those obtained by the proposed software do not vary significantly (red contour). (c) Segmentations of a cancer-derived multicellular spheroid, imaged with an LSFM at a single-cell level. (d) 3D-Cell-Annotator can be used to extract cells with a special phenotype as shown in the magnified cell (red). Figure is adapted from [9].

This tool facilitates the 3D segmentation of individual cells and nuclei from a 3D dataset, commonly acquired using confocal, multi-photon, or light-sheet fluorescence microscopes. It employs 3D active contours with shape descriptors as prior information to achieve accurate single cell annotation in a semi-automatic manner. Each object is assigned a label to initiate contour evolution, and the annotation process can be done manually, cell-by-cell, or semi-automatically by placing initial seed points. Unlike the general active surface algorithm, which may generate object clusters when cells share boundaries, the proposed selective active surface method uses user-provided shape descriptor values (sphericity and volume) to apply forces and ensure more precise segmentation. During surface evolution, these prior parameters can be finely adjusted with high precision to achieve single cell level segmentation. The resulting segmentations are automatically exported as 3D masks.

During the evaluation of 3D-Cell-Annotator, we computed the Jaccard Index for the segmentations obtained by 3D-Cell-Annotator, and compared it to other tools as well as to manual segmentations executed by expert annotators [9, 10]. The obtained results showed that 3D-Cell-Annotator works with an accuracy comparable to human experts. Based on these results, we consider this tool suitable for generating training tests for more advanced machine learning approaches.

5.1.3 3D nuclei segmentation

As we implied in chapter 5.1.2, our aim is to segment cell nuclei automatically. Of the existing methods, we chose StarDist-3D [139] because its developers claim that it works with high precision in images with low signal-to-noise ratios and/or dense packing of nuclei, which is the case in images of spheroids. The name "StarDist" was chosen because this model applies a star-convex polygon representation for cell shape, instead of using

more traditional methods like watershed transformations [140] or the U-Net convolutional neural network [141].

As StarDist is a method for deep learning based instance segmentation, it requires training data. This data consists of corresponding pairs of input (i.e. raw) images and fully annotated label images (i.e. every pixel is labelled with a unique object id or 0 for background). During the training there are two main steps (Figure 16):

1. Object Detection: StarDist begins by detecting the centers of individual cells in the 3D image. Each cell is associated with a center voxel (a pixel in 3D space). The task is formulated as a binary classification problem where each voxel in the 3D image is classified as either being the center of a cell or not.

2. Shape Prediction: After the centers of cells are detected, StarDist predicts the 3D shape of each cell. This is done by predicting the distances from the center voxel to the boundary of the cell in various directions.
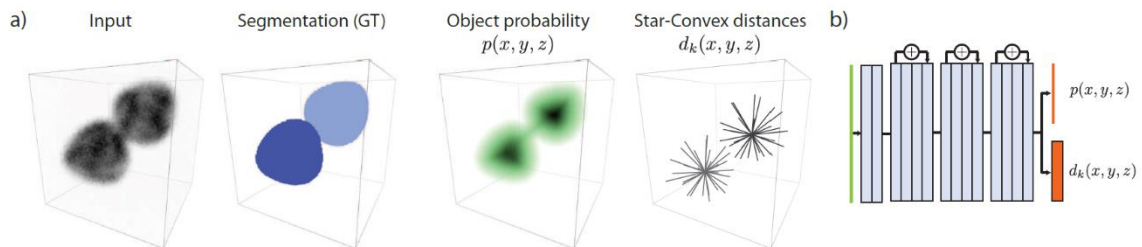
Figure 16 *Representation of the StarDist-3D method. a) StarDist-3D method is trained to densely predict object probabilities p and radial distances d_k to object boundaries. b) Schematic of the used convolutional neural networks architecture based on ResNet. Figure is adapted from* [139].

This method predicts the parameters of the polyhedra directly and densely for each pixel. Following this, it applies non-maximum suppression to remove redundancies from the large set of polyhedron shapes that we've obtained. Ideally, this process will leave us with only one predicted shape for each actual object in the image.

5.2. Materials and methods

5.2.1 Co-culture spheroid dataset

We used 3D images of co-culture spheroids as a test dataset. The spheroids were generated from Hela-Kyoto adenocarcinoma cells and MRC-5 fibroblast cells. The cell ratio was: 20+80% (60 HeLa cells + 240 MRC-5 = 300 cells/well). The seeding happened sequentially, which means that on day 1 60 HeLa cells per well were seeded into a U-bottom, cell-repellent 384-well plate (Greiner, 787979). On day 2, 240 MRC-5 cells were added to each well. The spheroids were incubated in a medium consists of DMEM supplemented with 10% of FBS, 1% L-glutamine and 1% P/S/A. After the spheroids developed, they were washed twice with Ca^{2+}/Mg^{2+} PBS and fixed with 4% PFA for an hour at room temperature. For the staining, the spheroids were incubated in 1% TRITON-X for overnight, then wash with PBS 2 times. The nuclei were stained with DAPI (1 µg/ml) overnight. The Hela-Kyoto cells express two fluorescent proteins, a H2B-associated mCherry fluorescent protein and an alpha tubulin-associated EGFP (enhanced GFP). This means that the nuclei of Hela-Kyoto cells, when excited with 638 nm light, are visible in fluorescence microscopy images without staining. When looking at the DAPI channel, all nuclei from both the HeLa and fibroblast cell lines are visible (Figure 17).
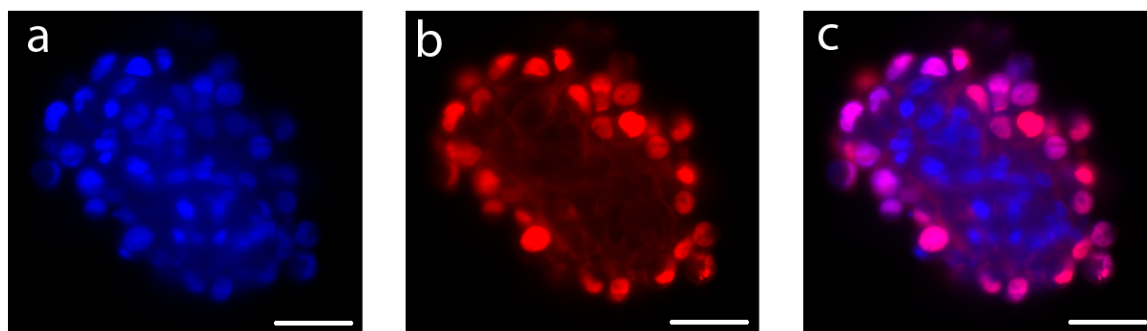
Figure 17 Cell nuclei in a HeLa-Kyoto – MRC-5 co-culture spheroid. a) Cells under 405 nm laser excitation (we could see all of the cell nuclei), b) cells under 638 nm laser excitation (we could only see the Hela-Kyoto cells), c) the combination of the channels in a) and b). Scalebar: 50 µm.

A Leica SP8 Digital LightSheet microscope was used to take fluorescence images. Fluorescence light sheet images were acquired with an exposure time of 200 ms at 50% laser intensity at 405 and 638 nm (maximum laser intensity 350 mW), and a 25x/0.95

detection objective was used for light sheet imaging with a 2.5 mm mirror device mounted on the objective. Images were captured with the sCMOS DFC9000 Leica camera at a resolution of 2048 × 2048 pixels with a pixel size of 0.14370117 μm. The spacing between images in each z-set was 3.7 μm.

5.2.2 Segmentation

For 3D nuclei segmentation, we used the aforementioned StarDist-3D method [139]. However, as it was described in subchapter 5.1.3, to train the deep neural network, we need annotated 3D data. To create that, we used 3D-Cell-Annotator [9] on 12 images showing fluorescently labelled nuclei of spheroids. Our training dataset contained manually and semi-automatically annotated nucleus instances (7238 in total). We applied data augmentations during training, including random rotations, flips, and intensity changes, which are typically sensible for 3D microscopy images.

We randomly chose 9/3 images for training/validation. To evaluate the performance of our trained model, we used the same metrics as the authors of the StarDist article [139]. Namely, we calculated

$$accuracy(\tau) = \frac{TP}{TP + FN + FP}$$

where *TP* are true positives, which are pairs of predicted and ground-truth nuclei having an overlap beyond a chosen *intersection over union* threshold (τ). *FP* are false positives (unmatched predicted instances) and *FN* are false negatives (unmatched ground-truth instances). The value of τ can be between 0 (even slightly overlapping objects count as correctly predicted) and 1 (only pixel-perfectly overlapping objects count). During our evaluation, we set τ to 0.7 and reached 0.6453 accuracy.

After the training was finished, we used our model to segment nuclei in new, previously unseen images (see Figure 18).
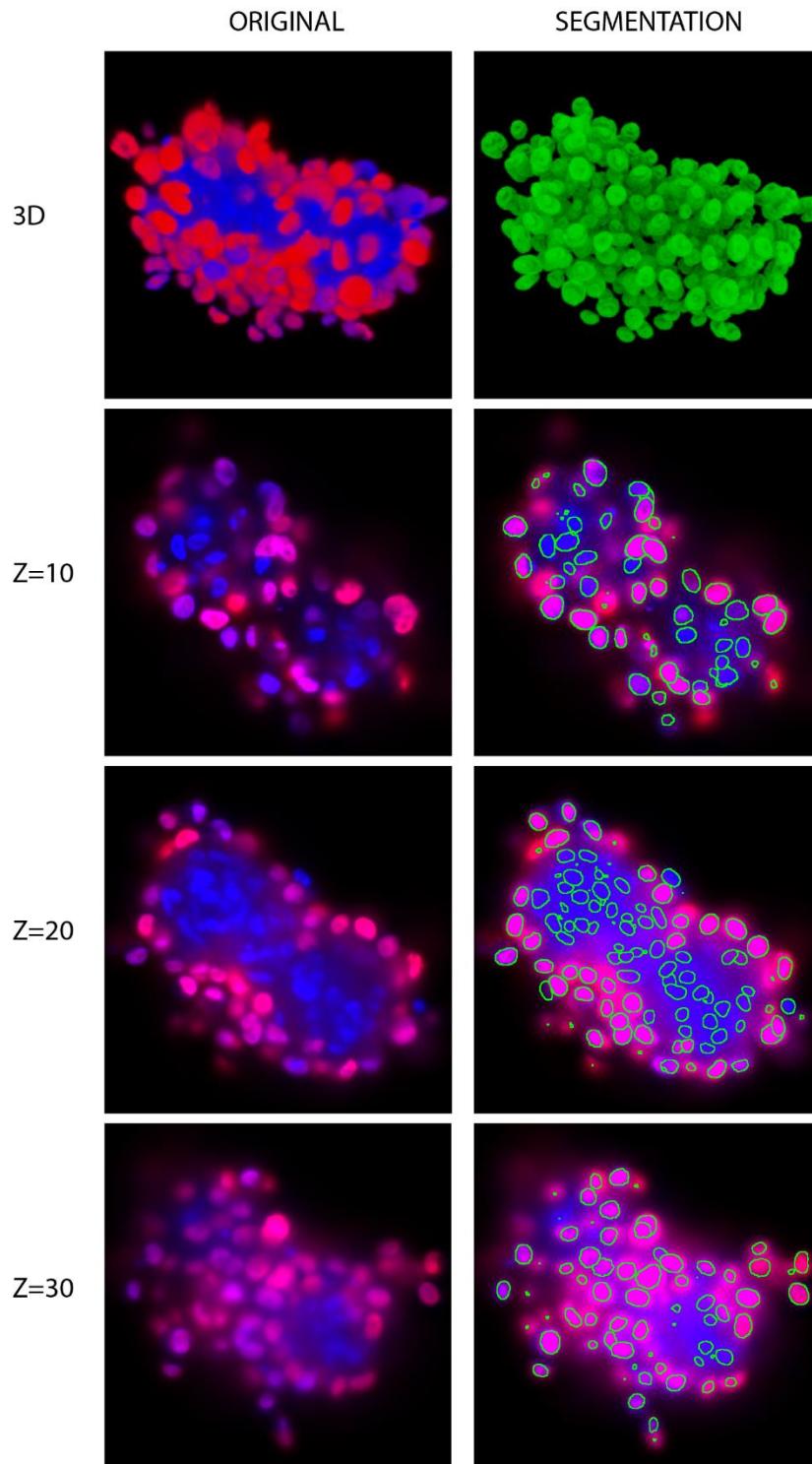
Figure 18 *Nuclei segmentation with StarDist-3D method on a Hela-Kyoto-MRC-5 co-culture spheroid. Top: 3D representation of a nuclei-labelled co-culture spheroid and the segmentation what was performed on it. Bottom: Representation of the nuclei segmentation in different z-positions, showing the top, the middle and the bottom region of the spheroid.*

5.2.3 Feature extraction

We extracted 3D features that describe the shape and intensity of the selected nuclei and we used neighbourhood features to represent the microenvironment. The full list of features we used:

- *Regular features*:
    - *Shape features*: elongation, equivalent ellipsoid diameters, equivalent sphere diameter, equivalent sphere perimeter, extent, Feret diameter, flatness, number of components, principal moments, rotation invariants, roundness, surface voxels, volumetry, voxels
    - *Intensity features*: integrated, minimum, maximum, mean, median and standard deviation statistics of a 3D region
- *Neighbourhood features*: the minimum, maximum, mean, median, and standard deviation statistics of the regular features; distance features: minimum, maximum, mean, median, standard deviation.

Similar to what was presented in Chapter 3, we have defined what we consider a neighbour in two ways: with the KNN and the N-distance methods (here, we calculated the Euclidean-distances in the 3D space). For the feature extraction, we used BIAS (see subsection 3.3.1).

5.2.4 Machine learning classification

After feature extraction, we created a training dataset for machine learning classification using BIAS. We distinguished two classes: HeLa-Kyoto cells and MRC-5 cells and 400 cells were labelled. We took special care to not label the same cell types that are in a close proximity, because it could potentially cause a bias in the evaluation. During the labelling, the human experts used information in the images from both the red and blue channels to distinguish the two cell types. Fibroblast cells are visible only in the blue channel, while carcinoma cells are visible in both channels (Figure 17,19). However, after preliminary tests, where our concept performed above 99% accuracy (Supplementary Section 3), we raised the question whether accurate classification was possible using shape features only. So it is important to point out that from then, we performed our training in such a way that the machine learning algorithms were not given intensity information of the objects

(whether a given nucleus was visible in the red or blue channel), but could only use data about the shape of the nuclei (Figure 19).

We tested the performance of two classification methods: Random Forest and Multilayer Perceptron with different KNN and N-distance sizes. We used 10-fold cross validation to measure the accuracy.
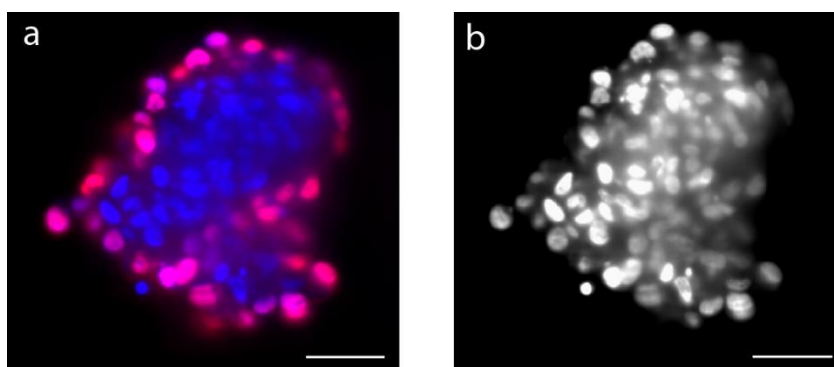
Figure 19 *a) Image seen by the human expert during training data generation b) Image used by the machine learning algorithm. Scalebar: 50 µm.*

5.3. Results

With two classification methods (Random Forest and Multilayer Perceptron), we compared whether the usage of regular features, neighbourhood features or the combination of these features give us the highest classification accuracy (Figure 20). We also took into account the size of the neighbourhood, we selected 5-25 nearest neighbours for the KNN and 100-500 pixels (14.37-71.85 µm) for the N-distance-based analysis.
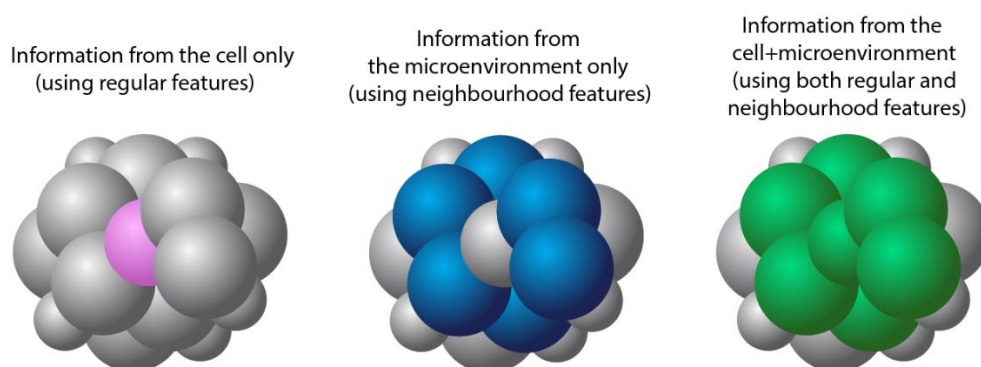
Figure 20 *Illustration of the origin of regular features, neighbourhood features and the combination of them*

The cross-validation results show that using neighbourhood features increases accuracy in every examined case (Figure 21). For both classifiers, whether KNN or N-distance approach was used, the highest results were obtained when both regular and neighbourhood features were included in the calculation. The best performance we observed was for the 25 KNN using the Random Forest classifier. In this case, accuracy reached 87.5%, which is 13% better than that achieved when considering local features only.
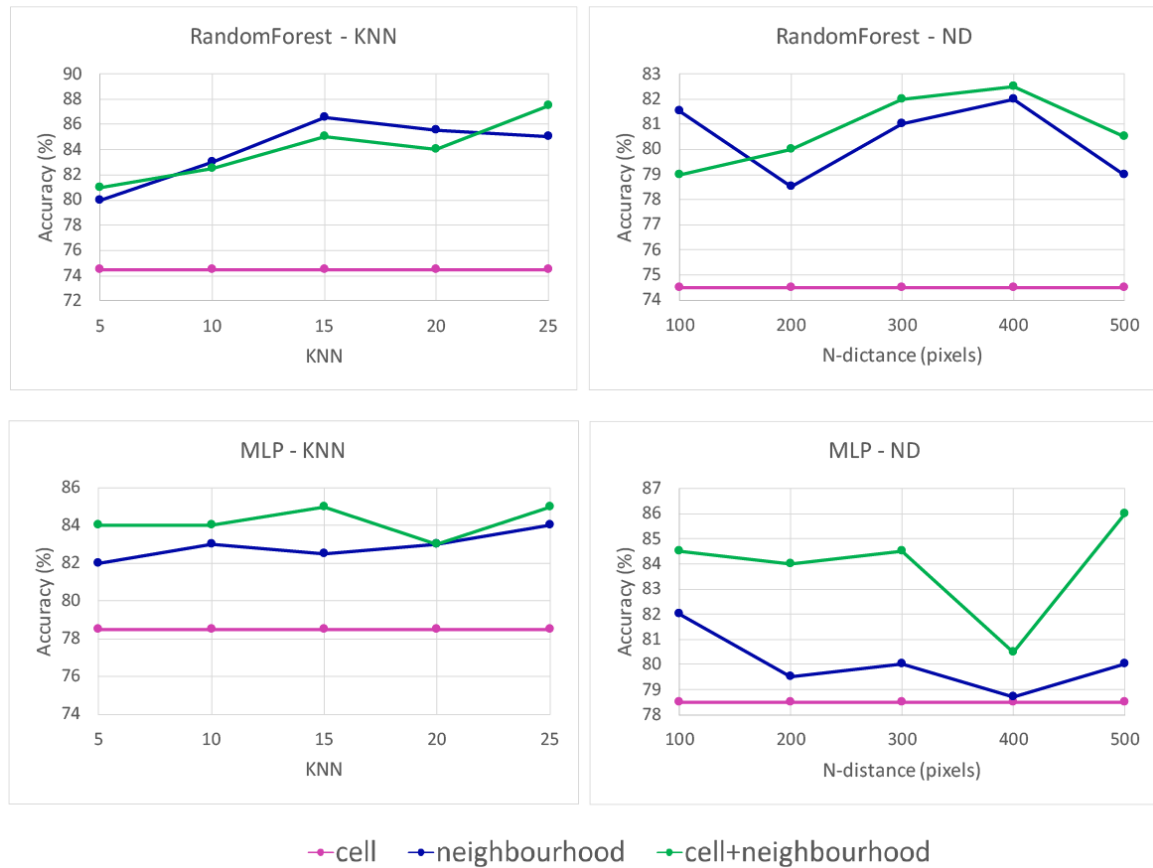
Figure 21 *Comparison of the performance of machine learning methods RandomForest and MultilayerPerceptron (MLP) on different neighbourhood distances. Neighbours were selected with the KNN (left) and the N-distance methods (right).*

6. Discussion

The unprecedented progress in collecting and storing digital data has fuelled the demand for fast and dependable computer-based processing of digital images. This process aims to extract valuable insights from complex and diverse image datasets. In fields like life sciences, the improvements in microscopy provides never-seen chances for in-depth and detailed examination of biological systems. However, analysing this large amount of information requires automated processing of thousands of images.

In this thesis, cell biology and pathology derived microscopy image analysis was addressed at a single-cell level. This kind of analysis can be a starting point to get detailed insight to the mechanism of action, viability or disease progression of individual cells in samples. There is a great potential that this deeper understanding could lead to more efficient treatments in drug discovery and clinical trials, or diagnosis in personalised medicine.

Phenotypic single-cell analysis has become an important part of next-generation digital pathology evaluations. Regular histology work includes comparing neighbouring cells on a slide at smaller or larger distances. For instance, the subjective morphological comparison of nearby tumour cells is commonly used to identify anisocytosis or anisonucleosis, two biological hallmarks of malignancy [6]. Most often, digital pathology evaluation strategies concentrate on single cell features, the environment of individual cells is beyond its focus.

In the first part of this thesis, we introduced a machine learning-based phenotyping method that uses both local and neighbourhood features. We showed that taking the cellular microenvironment into account significantly increases the recognition accuracy. This enhancement was observable for both cell cultures and tissue sections. However, we should point out that it was somewhat weaker (but still noticeable) in the case of images of cell cultures. From a biological viewpoint it is not difficult to explain why there is a difference in improvements between the MCF-7 and UBC datasets. Human tissue is a collection of heterogeneous cell types. Certain cell types frequently appear near each other, so recognising one can help us identify the other.

The main questions we needed to address were: how many nearby cells do we need to include and from how far away to improve single-cell classification? In a cell culture, as

expected, including more cells from the environment increased accuracy for all of the classifiers until it reached a plateau. In the case of the urinary bladder cancer sections, we found a peak of the optimal distance of neighbours at ~80–100 micrometres, almost independently of the type of the classification method. Due to the inclusion of neighbouring cells, the amount of information substantially rises until a certain point (i.e. the optimal neighbourhood size). After this, adding more cells that are farther apart, led to a slowly growing confusion, i.e. the increasing number of neighbouring elements resulted in a decrease in accuracy. In our study, the NaiveBayes classifier achieved a modest level of accuracy, while the SMO, RandomForest, and MultiLayer Perceptron methods worked with high accuracy.

In the second part of the thesis, we presented a method combining fisheye transformation with deep learning, an extension to our previous model, incorporating the information obtained from the cellular microenvironment in phenotypic classification. We showed that our method works better on MCF-7 cell culture and urinary bladder cancer datasets than using traditional machine learning with regular and neighbourhood features. We compared our results to the performance of deep neural networks (ResNet50 and InceptionV3) that used non-fisheye transformed images as inputs. For each dataset we used (a cell culture, two tissue sections, and a dataset containing images of animals), training with fisheye-transformed images resulted in significantly higher phenotypic classification accuracies.

An interesting segment of the testing was the inclusion of the iWildCam dataset. This is the only dataset in this thesis which is not cell biology or histology related. In the case of this set, usage of the fisheye transformation caused only a minor improvement in accuracy compared to the other datasets. The reason behind that might be that while recording the animals, fixed positioned cameras were used. This means that if animals were close or far from the camera, the view of their environment could be big, small, or not visible at all. Hence, even if we increase the window size, it may occur that we do not gain more information about the surrounding area.

The third part of the thesis delved into the challenges of working with 3D cell cultures and the subsequent analysis in a three-dimensional context. The scientific community is excited about 3D cellular model systems because they promise to more closely reflect and recreate the in vivo tissue environment than 2D systems. We have to keep in mind though, that

these models frequently lack the necessary cell types and growth factors and do not take into account long-distance signalling from other organs, the immune system, the endocrine system, or the microbiome. As a result, in many cases they do not represent the complexity of many in vivo tissues [142].

Imaging of 3D model systems is a difficult task, due to the fact that these systems are characterised by high density and differences in refractive index that perturb the penetration depth of light and the opportunity to visualise very large spheroids [143]. In our work, we compared five clearing protocols on three types of spheroids generated from carcinoma cell-lines. We reviewed and evaluated seven quality metrics which quantitatively characterise the imaging quality. Based on our findings, we proposed the use of a unique quality metric as a way to compare optical clearing techniques and select the one that is most appropriate for a given experiment.

A first step of many single-cell image analysis pipeline is segmentation. There are already existing methods to do this task in 3D [10], however, especially the deep-learning approaches require 3D annotated data to work properly. We developed 3D-Cell-Annotator that could potentially help annotators to create such training dataset in a semi-automated fashion.

Finally, we showed our results in studying single-cells and their neighbourhood in a 3D co-culture that consisted of carcinoma and fibroblast cells. We found that including the neighbourhood features in our calculations improved phenotypic classification accuracy. An interesting result is that we could achieve a higher accuracy using the neighbourhood features only without including information about the cell itself. Another important finding is that we could recognize the two cell-types with 87.5% accuracy when we took into account only the shape attributes of the cells and their neighbours. This could have a critical influence on cell staining or labelling execution. Designing these cell staining experiments is a demanding task. So if we can demonstrate that we can get enough information for analysis while using fewer dyes, we can make it easier to carry out experiments.

In conclusion, we showed that the incorporation of the microenvironment into machine-learning based decisions can improve the task of single-cell phenotypic classification. This underscores the notion that cellular structures exhibit a deliberate organisation, and it is beneficial to account for these macro-structures in our considerations.

Our research also raises several directions to follow. One thing worth testing is the effectiveness of the fisheye transformation in 3D. We have seen that in the 2D case, it has improved the accuracy of the cell classification. However, the 2D implementation of the transformation was not integrated into a deep learning network, so it implies an extra pre-processing step. Including this integration in the 3D implementation would probably make the learning process easier and faster.

Another direction is to examine more complex 3D structures. It could be achieved by increasing the number of cell lines we use during co-culture spheroid generation. Another way to get more information from 3D cell cultures is to distinguish more phenotypes than we worked with before (for example dead/alive cells or mitotic cells). In our opinion, similar to the 2D case, the microenvironment may have a greater influence on the appearance of individual cells in 3D tissue samples. However, even with the promising advancements in tissue sectioning and image registration methods [144–146], it is rarely possible to achieve 3D single-cell resolution. Nonetheless, we believe that with the right choice of optical clearing and fluorescence staining protocols, we can get closer to 3D single-cell phenotype analysis in tissue samples. Classifying cells in such systems more accurately is a step towards characterising and understanding the phenotypic heterogeneity and cellular diversity of organisms.

Acknowledgements

I would like to thank my supervisor Péter Horváth for his support and guidance throughout my PhD. He was always open to share his ideas and advices and it is with his invaluable assistance that I have been able to develop both as a scientist and as an individual.

I am also grateful to past and present members of the BIOMAG group for the invaluable discussions. I thank Krisztián Koós, Mária Kovács and Csaba Molnár for their instrumental role in facilitating my smooth integration into the group during my first days. I appreciate the help of Dávid Bauer, Ferenc Kovács, András Kriston, Mária Harmati and Ervin Tasnádi, who always found the time to discuss technical issues with me. I would also like to express my gratitude to Filippo Piccinini who hosted me for a month in his group in Italy and introduced me to the world of 3D cell cultures.

I would like to thank the 'room 636 guys', Ákos Diósdi, István Grexa, Dominik Hirling and Nikita Moshkov for their humour and endless support. They are not just my co-workers, but also my dear friends. Plus, without our shared Spotify playlist, cell annotation would not be the same.

A special acknowledgment goes to my friend Klára Gerlei for proofreading this thesis. She and Péter Bélteky kept my spirits high over the last many, many years.

I extend my deep gratitude to my mother, Gabriella Kovács for the patience and support she has given me. And last but not least, it would not have been possible to write my thesis without my daughter, Zsófi whose smile always filled me with energy.

Summary

Machine learning has assumed a pivotal role in the realms of cell biology and medical image analysis. This emergence is primarily attributed to advancements in microscopy and computational cell biology, resulting in an unprecedented surge in data volume, often reaching the scale of millions of images per study. Modern-day researchers increasingly prefer high-content screenings; however, manually analysing the resulting datasets is either excessively time-consuming or, in some instances, not feasible. Moreover, there is potential for machines to identify valuable features within images that are beyond the human eye's capabilities. There is a shared interest in achieving detailed and reliable medical diagnoses and treatment. To accomplish this objective, it is crucial to enhance the accuracy of machine learning algorithms.

This thesis presents our research in microscopic image analysis. Our aim was to extract valuable insights from complex image datasets on a single-cell level, particularly in the context of cell biology and pathology. We showed the influence of considering the cellular microenvironment in the phenotypic characterisation of individual cells using supervised machine learning and deep learning techniques.

Firstly, we analysed images of MCF-7 cell culture and urinary bladder cancer tissue sections with classical supervised machine learning methods. We defined two approaches to represent the microenvironment: the K-nearest neighbours (KNN) and the N-distance methods. We extracted regular and neighbourhood features, and we have seen that while the local features of cells can be similar across different phenotypic classes, the neighbourhood features are able to identify them. The results of our analysis demonstrated that the incorporation of neighbourhood features significantly enhances the accuracy of machine learning-based classification, regardless of whether the data originates from cell cultures or tissue sections. The optimal size of the neighbourhood varied according to the specific dataset and classifier used. Notably, our findings emphasised the substantial impact of neighbourhood features on tissue section phenotyping, with performance improvement close to 20%.

In the second part of the dissertation, we introduced a novel approach of representing images to deep-learning-based image classification networks. The fundamental concept revolves around the following notion: the original image includes both the object of

interest, as well as its surrounding microenvironment within a pre-defined range. Subsequently, a fisheye-like spatial sampling technique is applied to transform the images. The fisheye sampling collects more pixels from the close proximity of the object of interest, and the resolution decreases for larger proximity. Our findings demonstrated that the proposed transformation highly outperforms conventional machine-learning techniques and deep-learning-based classifiers. This performance was evaluated across various datasets including cell cultures, scans of cancerous tissues, and real-life images.

While images in the MCF-7 cell culture dataset may contain visually uniform sections, it is important to recognise that these areas do not consist of cells that are molecularly identical. In such instances, the fisheye transformation proves valuable in capturing distinctions within these regions, and the utilisation of neighbourhood information offers a more statistically robust foundation for decision making.

The most notable enhancement was in the case of urinary bladder cancer and lung cancer tissue sections, where variations in the microenvironment are clearly distinguishable. These distinctions become evident in histological examinations of tissues, revealing the synergistic relationships and interdependencies among various cell types. Our approach effectively captures these distinctions by employing the fisheye transformation and taking into account the spatial relationships of cells in different phenotypic classes.

We observed only a modest accuracy improvement in the case of the iWildCam dataset (containing images of wild animals). It is still a relevant finding, as it demonstrates that the fisheye transformation approach is not useful in the case of microscopy images only, but for images from other aspects of life as well, where the environment plays an important role.

In the third part of the thesis, we turned our attention to 3D cell cultures. As 3D single-cell analysis is a relatively new scientific field, we faced several challenges during the steps that precede phenotypic classification.

We discussed the enhancement of microscopy image quality through optical clearing and assessed the efficacy of various clearing protocols. We presented our work on the development and comparison of a novel metric designed to assess the effectiveness of optical clearing protocols for 3D images in a consistent manner. We generated a 3D dataset consisting of cancer spheroids and used five different clearing protocols. We examined

seven no-reference sharpness metrics to evaluate these protocols. Out of the seven metrics only intensity variance proved suitable for quantitatively measuring the effect of optical clearing in microscopy images.

Then, we explored the difficulties and remedies associated with annotating and segmenting cells in three dimension. Segmentation is the first step of single-cell level bioimage analysis. In 2D it is already demonstrated that the usage of deep learning methods for this task is highly effective. However, for the segmentation of 3D cell cultures, such algorithms require 3D-annotated data. To create this dataset manually is time-consuming and could lead to inaccurate training instances. To overcome these issues, we developed an MITK (Medical Imaging Interaction Toolkit) plugin, 3D-Cell-Annotator, which allows us to do annotation in a semi-automatic way.

Lastly, we shared our achieved progress in investigating cells and their microenvironment within 3D co-cultures consisted of carcinoma and fibroblast cells. Similar to the first part, we used KNN and N-distance measurements to determine which cells we consider neighbours, and then performed the classifications with supervised machine learning algorithms. Our results showed, that including the neighbourhood features in the machine learning process increased phenotypic classification accuracy. Furthermore, we could distinguish the two cell types with 87.5% accuracy, solely by considering the shape attributes of the cells and their neighbours.

Overall, the research demonstrates that integrating the cellular microenvironment into machine learning-driven analysis enhances single-cell phenotypic classification. This highlights the importance of considering macro-structures within cellular systems, ultimately advancing the understanding and potential applications of image analysis in various scientific contexts.

Összefoglalás

A gépi tanulás kulcsfontosságú szerepet tölt be a sejtbiológia és az orvosi képelemzés területén. Ez elsősorban a mikroszkópia és a számítógépes sejtbiológia fejlődésének köszönhető, ami az adatmennyiség soha nem látott mértékű megugrását eredményezte, gyakran elérve a több millió képet vizsgálatonként. Napjainkban a kutatók egyre inkább a high-content felvételeket részesítik előnyben. Az így keletkező adathalmazok kézi elemzése azonban vagy túlságosan időigényes, vagy egyes esetekben egyenesen lehetetlen. Ezen kívül az elemzések során a számítógépek olyan értékes jellemzőket azonosíthatnak a képeken belül, amelyek az emberei szem számára láthatatlanok. Közös érdek a részletes és megbízható orvosi diagnózisok és kezelések felállítása. E cél eléréséhez elengedhetetlen a gépi tanulási algoritmusok pontosságának növelése.

Ez a dolgozat a mikroszkopikus képelemzéssel kapcsolatos kutatásainkat mutatja be. Célunk az volt, hogy egysejtes szinten, különösen a sejtbiológia és a patológia összefüggésében értékes felismeréseket nyerjünk összetett képadathalmazokból. Megmutattuk, hogy a sejtek mikrokörnyezetének figyelembevétele milyen hatással van az egyes sejtek fenotípus jellemzésére, felügyelt gépi tanulás és mélytanulási technikák segítségével.

Először MCF-7 sejttenyészetről és húgyhólyagrákos szöveti metszetekről készült képeket elemeztünk klasszikus felügyelt gépi tanulási módszerekkel. Két megközelítést használtunk a mikrokörnyezet meghatározására: a K-közelebbi szomszéd (KNN) és az N-távolság módszerét. Lokális és szomszédsági jellemzőket vontunk ki, és azt láttuk, hogy míg a sejtek helyi jellemzői hasonlóak lehetnek a különböző fenotípus osztályokban, a szomszédsági jellemzők képesek megkülönböztetni őket. Eredményeink azt mutatták, hogy a szomszédsági jellemzők bevonása jelentősen növeli a gépi tanuláson alapuló osztályozás pontosságát, függetlenül attól, hogy az adatok sejtkultúrákból vagy szöveti metszetekből származnak. A szomszédság optimális mérete az adott adathalmaztól és az alkalmazott osztályozótól függően változott. Eredményeink kiemelik a szomszédsági jellemzők jelentős hatását a szöveti metszetek fenotipizálása esetében, ahol a teljesítményjavulás megközelítette a 20%-ot.

A disszertáció második részében a képek reprezentálásának újszerű megközelítését mutattuk be, amelyek a mélytanuláson alapuló képosztályozó hálózatok bemeneteként

71

funkcionálhatnak. Az elvárásaink a következők voltak a bemeneti képekkel kapcsolatban: az eredeti kép tartalmazza mind a számunkra érdekes objektumot, mind pedig az azt körülvevő mikrokörnyezetet egy előre meghatározott tartományon belül. Ezt követően egy halszemoptika-szerű térbeli mintavételi technikát alkalmazunk a képek átalakítására. A halszemoptika-szerű mintavételezés több képpontot gyűjt össze a vizsgált objektum közvetlen közeléből, mint a távolabb elhelyezkedő képterületekről. Eredményeink azt mutatták, hogy a javasolt transzformáció nagymértékben felülmúlja a hagyományos gépi tanulási technikákat és a mélytanuláson alapuló osztályozókat. Ezt a teljesítményt különböző adathalmazokon, köztük sejttenyészeteken, rákos szöveti metszeteken és valós életből származó képeken értékeltük.

Bár az MCF-7 sejtkultúra adathalmaz képei vizuálisan egységes megjelenésű sejteket tartalmazhatnak, fontos felismerni, hogy ezek a területek nem molekulárisan azonos sejtekből állnak. Ilyen esetekben a halszem-transzformáció értékesnek bizonyul a régiókon belüli különbségek megragadásában, és a szomszédsági információk felhasználása statisztikailag megbízhatóbb alapot nyújt az osztályozáshoz.

A legjelentősebb javulást a húgyhólyagrák és a tüdőrák szöveti metszeteknél tapasztaltuk, ahol a mikrokörnyezet eltérései egyértelműen felismerhetők. Ezek a különbségek szövettani vizsgálatok során válnak nyilvánvalóvá, feltárva a különböző sejttípusok közötti szinergikus kapcsolatokat és kölcsönös függőségeket. Megközelítésünk a halszem-transzformáció alkalmazásával és a különböző fenotípusos osztályokba tartozó sejtek térbeli kapcsolatainak figyelembevételével hatékonyan használja fel ezen különbség-információkat.

Az iWildCam adathalmaz (amely vadon élő állatok képeit tartalmazza) esetében csak szerény pontosságjavulást tapasztaltunk. Mindazonáltal a változás szignifikáns és kiemelt számunkra, mivel azt mutatja, hogy a halszem-transzformáción alapuló megközelítés nem csak a mikroszkópos képek esetében hasznos, hanem az élet más területeiről származó képek esetében is, ahol a környezet fontos szerepet játszik.

A dolgozat harmadik részében a 3D-s sejtkultúrák felé fordítottuk figyelmünket. Mivel a 3D egysejtes analízis viszonylag új tudományos terület, a fenotípus osztályozást megelőző lépések során számos kihívással szembesültünk.

Tárgyaltuk a mikroszkópos képminőség optikai tisztítással történő javítását, és felmértük a különböző tisztítási protokollok hatékonyságát. Bemutattuk egy olyan új metrika

kifejlesztésére és összehasonlítására irányuló munkánkat, amelynek célja a 3D képek optikai tisztítási protokolljainak hatékonyságának egységesített értékelése volt. Létrehoztunk egy rákos szferoidokból álló 3D-s adathalmazt és öt különböző tisztítási protokollt alkalmaztunk ezen mintákon. E protokollok hatékonyságának megállapítására hét fajta kiértékelést vizsgáltunk. A hét metrika közül csak az intenzitásvariáció bizonyult alkalmasnak az optikai tisztítás hatásának kvantitatív mérésére mikroszkópos képeken.

Ezután megvizsgáltuk a sejtek háromdimenziós annotálásával és szegmentálásával kapcsolatos kihívásokat. A szegmentálás az egysejtes biológiai képek elemzésének első lépése. 2D-ben már bebizonyosodott, hogy a mélytanulási módszerek használata erre a feladatra igen hatékony. A 3D-s sejttenyészetek szegmentálásához azonban az ilyen algoritmusoknak 3D-s annotált tanító adatokra van szükségük. Ennek az adathalmaznak a manuális létrehozása időigényes és pontatlan tanítási példák használatához vezethet. E problémák leküzdésére kifejlesztettünk egy MITK (Medical Imaging Interaction Toolkit) plugint, a 3D-Cell-Annotator-t, amellyel az annotációt részben automatizált módon végezhetjük el.

Végül megosztottuk a sejtek és mikrokörnyezetük vizsgálatában elért eredményeinket a karcinóma- és fibroblaszt sejtekből álló 3D ko-kultúrák esetében. Az első részhez hasonlóan KNN és N-távolság mérésekkel határoztuk meg, hogy mely sejteket tekintjük szomszédnak, majd felügyelt gépi tanulási algoritmusokkal végeztük el az osztályozásokat. Eredményeink azt mutatták, hogy a szomszédsági jellemzők bevonása a gépi tanulási folyamatba növelte a fenotípus osztályozási pontosságot. 87,5%-os pontossággal tudtuk megkülönböztetni a két sejttípust a szferoidokon belül, kizárólag a sejtek és szomszédaik alaki jellemzőinek figyelembevételével.

Összességében a kutatás azt mutatja, hogy a sejtek mikrokörnyezetének integrálása a gépi tanulás által vezérelt elemzésbe javítja az egysejtes fenotípus osztályozást. Ez rávilágít a mikrostruktúrák sejtes rendszereken belüli figyelembevételének fontosságára, ami végső soron a képelemzés megértését és lehetséges alkalmazásait segíti elő különböző tudományos kontextusokban.

References

1. Horvath, P., Aulner, N., Bickle, M., Davies, A.M., Nery, E. Del, Ebner, D., Montoya, M.C., Östling, P., Pietiäinen, V., Price, L.S., Shorte, S.L., Turcatti, G., Von Schantz, C., Carragher, N.O.: Screening out irrelevant cell-based models of disease. Nat. Rev. Drug Discov. 15, 751–769 (2016). https://doi.org/10.1038/nrd.2016.175.

2. Domingos, P.: A Few Useful Things to Know About Machine Learning. Commun. ACM. 55, 78–87 (2012). https://doi.org/10.1145/2347736.2347755.

3. Sommer, C., Gerlich, D.W.: Machine learning in cell biology – teaching computers to recognize phenotypes. J. Cell Sci. 126, 5529 LP – 5539 (2013).

4. Grys, B.T., Lo, D.S., Sahin, N., Kraus, O.Z., Morris, Q., Boone, C., Andrews, B.J.: Machine learning and computer vision approaches for phenotypic profiling. J. Cell Biol. 216, 65–71 (2016). https://doi.org/10.1083/jcb.201610026.

5. Pratapa, A., Doron, M., Caicedo, J.C.: Image-based cell phenotyping with deep learning. Curr. Opin. Chem. Biol. 65, 9–17 (2021). https://doi.org/10.1016/j.cbpa.2021.04.001.

6. Toth, T., Balassa, T., Bara, N., Kovacs, F., Kriston, A.: Environmental properties of cells improve machine learning-based phenotype recognition accuracy. Sci. Rep. 1–9 (2018). https://doi.org/10.1038/s41598-018-28482-y.

7. Toth, T., Bauer, D., Sukosd, F., Peter, H.: Fisheye transformation enhances deep-learning- based single-cell phenotyping by including cellular microenvironment. Cell Reports Methods. 2, 100339 (2022). https://doi.org/10.1016/j.crmeth.2022.100339.

8. Diosdi, A., Hirling, D., Kovacs, M., Toth, T., Harmati, M., Koos, K., Buzas, K., Piccinini, F., Horvath, P.: A quantitative metric for the comparative evaluation of optical clearing protocols for 3D multicellular spheroids. Comput. Struct. Biotechnol. J. 19, 1233–1243 (2021). https://doi.org/10.1016/j.csbj.2021.01.040.

9. Tasnadi, E.A., Toth, T., Kovacs, M., Diosdi, A., Pampaloni, F., Molnar, J., Piccinini, F., Horvath, P.: 3D-Cell-Annotator : an open-source active surface tool for single-cell segmentation in 3D microscopy images. 36, 2948–2949 (2020).

https://doi.org/10.1093/bioinformatics/btaa029.

10. Piccinini, F., Balassa, T., Carbonaro, A., Diosdi, A., Toth, T., Moshkov, N., Tasnadi, E.A., Horvath, P.: Software tools for 3D nuclei segmentation and quantitative analysis in multicellular aggregates. Comput. Struct. Biotechnol. J. 18, 1287–1300 (2020). https://doi.org/10.1016/j.csbj.2020.05.022.

11. Shinde, P.P.: A Review of Machine Learning and Deep Learning Applications. 2018 Fourth Int. Conf. Comput. Commun. Control Autom. 1–6 (2018).

12. Russell, S., Norvig, P.: Artificial Intelligence: A Modern Approach. Prentice Hall Press, USA (2020).

13. Khemphila, A., Boonjing, V.: Comparing performances of logistic regression, decision trees, and neural networks for classifying heart disease patients. In: 2010 International Conference on Computer Information Systems and Industrial Management Applications (CISIM). pp. 193–198 (2010). https://doi.org/10.1109/CISIM.2010.5643666.

14. Usama, M., Qadir, J., Raza, A., Arif, H., Yau, K.A., Elkhatib, Y., Hussain, A., Al-Fuqaha, A.: Unsupervised Machine Learning for Networking: Techniques, Applications and Research Challenges. IEEE Access. 7, 65579–65615 (2019). https://doi.org/10.1109/ACCESS.2019.2916648.

15. Likas, A., Vlassis, N., J. Verbeek, J.: The global k-means clustering algorithm. Pattern Recognit. 36, 451–461 (2003). https://doi.org/https://doi.org/10.1016/S0031-3203(02)00060-2.

16. Murtagh, F., Contreras, P.L.S.: Algorithms For Hierarchical Clustering: An Overview. WIREs Data Min. Knowl. Discov. 2, 86–97 (2011). https://doi.org/10.1002/widm.53.

17. Ringnér, M.: What is principal component analysis? Nat. Biotechnol. 26, 303–304 (2008). https://doi.org/10.1038/nbt0308-303.

18. van Engelen, J.E., Hoos, H.H.: A survey on semi-supervised learning. Mach. Learn. 109, 373–440 (2020). https://doi.org/10.1007/s10994-019-05855-6.

19. Reddy, Y.C.A.P., Viswanath, P., Reddy, B.E.: Semi - supervised learning : a brief review. 7, 81–85 (2018).

20. Schmidt, J., Marques, M.R.G., Botti, S., Marques, M.A.L.: Recent advances and applications of machine learning in solid-state materials science. npj Comput. Mater. 5, 83 (2019). https://doi.org/10.1038/s41524-019-0221-0.

21. Choudhary, K., DeCost, B., Chen, C., Jain, A., Tavazza, F., Cohn, R., Park, C.W., Choudhary, A., Agrawal, A., Billinge, S.J.L., Holm, E., Ong, S.P., Wolverton, C.: Recent advances and applications of deep learning methods in materials science. npj Comput. Mater. 8, 59 (2022). https://doi.org/10.1038/s41524-022-00734-6.

22. Cai, L., Gao, J., Zhao, D.: A review of the application of deep learning in medical image classification and segmentation. Ann. Transl. Med. 8, 713 (2020). https://doi.org/10.21037/atm.2020.02.44.

23. Lauriola, I., Lavelli, A., Aiolli, F.: An introduction to Deep Learning in Natural Language Processing: Models, techniques, and tools. Neurocomputing. 470, 443–456 (2022). https://doi.org/https://doi.org/10.1016/j.neucom.2021.05.103.

24. Ying, X.: An Overview of Overfitting and its Solutions. J. Phys. Conf. Ser. 1168, 22022 (2019). https://doi.org/10.1088/1742-6596/1168/2/022022.

25. Kaur, H., Nori, H., Jenkins, S., Caruana, R., Wallach, H., Wortman Vaughan, J.: Interpreting Interpretability: Understanding Data Scientists' Use of Interpretability Tools for Machine Learning. In: Proceedings of the 2020 CHI Conference on Human Factors in Computing Systems. pp. 1–14. Association for Computing Machinery, New York, NY, USA (2020). https://doi.org/10.1145/3313831.3376219.

26. Rosenblatt, F.: The perceptron: a probabilistic model for information storage and organization in the brain. Psychol. Rev. 65 6, 386–408 (1958).

27. Linnainmaa, S.: Taylor expansion of the accumulated rounding error. BIT Numer. Math. 16, 146–160 (1976). https://doi.org/10.1007/BF01931367.

28. Ivakhnenko, A.G., Lapa, V.G.: CYBERNETIC PREDICTING DEVICES. Presented at the (1966).

29. Krizhevsky, A., Hinton, G.E.: ImageNet Classification with Deep Convolutional Neural Networks. 1–9.

30. Dang, Q., Yin, J., Wang, B., Zheng, W.: Deep Learning Based 2D Human Pose

Estimation : A Survey. 24, 663–676 (2019).

31.   Ronao, C.A., Cho, S.: Human activity recognition with smartphone sensors using deep learning neural networks. Expert Syst. Appl. 59, 235–244 (2016). https://doi.org/10.1016/j.eswa.2016.04.032.

32.   Schroff, F., Kalenichenko, D., Philbin, J.: FaceNet: A unified embedding for face recognition and clustering. In: 2015 IEEE Conference on Computer Vision and Pattern Recognition (CVPR). pp. 815–823 (2015). https://doi.org/10.1109/CVPR.2015.7298682.

33.   Grigorescu, S.: A survey of deep learning techniques for autonomous driving. (2019). https://doi.org/10.1002/rob.21918.

34.   Moen, E., Bannon, D., Kudo, T., Graf, W., Covert, M., Van Valen, D.: Deep learning for cellular image analysis. Nat. Methods. 16, 1233–1246 (2019). https://doi.org/10.1038/s41592-019-0403-1.

35.   He, K., Sun, J.: Deep Residual Learning for Image Recognition. 1–9.

36.   Weiss, K., Khoshgoftaar, T.M., Wang, D.: A survey of transfer learning. J. Big Data. 3, 9 (2016). https://doi.org/10.1186/s40537-016-0043-6.

37.   Mei, X., Liu, Z., Robson, M.S.P.M., Marinelli, B., Huang, M.: RadImageNet : An Open Radiologic Deep Learning Research Dataset for Effective Transfer Learning. (2022).

38.   Alzubaidi, L., Zhang, J., Humaidi, A.J., Al-Dujaili, A., Duan, Y., Al-Shamma, O., Santamaría, J., Fadhel, M.A., Al-Amidie, M., Farhan, L.: Review of deep learning: concepts, CNN architectures, challenges, applications, future directions. J. Big Data. 8, 53 (2021). https://doi.org/10.1186/s40537-021-00444-8.

39.   Azizpour, H., Razavian, A., Sullivan, J., Maki, A., Carlsson, S.: Factors of Transferability for a Generic ConvNet Representation. IEEE Trans. Pattern Anal. & Mach. Intell. 38, 1790–1802 (2016). https://doi.org/10.1109/TPAMI.2015.2500224.

40.   Litman, T.: Personalized medicine-concepts, technologies, and applications in inflammatory skin diseases. APMIS. 127, 386–424 (2019). https://doi.org/10.1111/apm.12934.

41.   Singh, S., Carpenter, A.E., Genovesio, A.: Increasing the Content of High-Content Screening : An Overview. (2014). https://doi.org/10.1177/1087057114528537.

42.   Dao, D., Fraser, A.N., Hung, J., Ljosa, V., Singh, S., Carpenter, A.E.: CellProfiler Analyst: interactive data exploration, analysis and classification of large biological image sets. Bioinformatics. 32, 3210–3212 (2016). https://doi.org/10.1093/bioinformatics/btw390.

43.   Mcdole, K., Amat, F., Turaga, S.C., Branson, K., Keller, P.J., Amat, F., Berger, A.: In Toto Imaging and Reconstruction of Post- Implantation Mouse Development at the Single- Cell Level In Toto Imaging and Reconstruction of Post-Implantation Mouse Development at the Single-Cell Level. 859–876 (2018). https://doi.org/10.1016/j.cell.2018.09.031.

44.   Kapałczyńska, M., Kolenda, T., Przybyła, W., Zajączkowska, M., Teresiak, A., Filas, V., Ibbs, M., Bliźniak, R., Łuczewski, Ł., Lamperska, K.: 2D and 3D cell cultures - a comparison of different types of cancer cell cultures. Arch. Med. Sci. 14, 910–919 (2018). https://doi.org/10.5114/aoms.2016.63743.

45.   Philippeos, C., Hughes, R.D., Dhawan, A., Mitry, R.R.: Introduction to cell culture. Methods Mol. Biol. 806, 1–13 (2012). https://doi.org/10.1007/978-1-61779-367-7_1.

46.   Ramsey, W.S., Hertl, W., Nowlan, E.D., Binkowski, N.J.: Surface treatments and cell attachment. In Vitro. 20, 802–808 (1984). https://doi.org/10.1007/BF02618296.

47.   Shen, M., Horbett, T.A.: The effects of surface chemistry and adsorbed proteins on monocyte/macrophage adhesion to chemically modified polystyrene surfaces. J. Biomed. Mater. Res. 57, 336–345 (2001). https://doi.org/10.1002/1097-4636(20011205)57:3<336::aid-jbm1176>3.0.co;2-e.

48.   Wiatrak, B., Kubis-Kubiak, A., Piwowar, A., Barg, E.: PC12 Cell Line: Cell Types, Coating of Culture Vessels, Differentiation and Other Culture Conditions. Cells. 9, (2020). https://doi.org/10.3390/cells9040958.

49.   Shariff, A., Kangas, J., Coelho, L.P., Quinn, S., Murphy, R.F.: Automated Image Analysis for High-Content Screening and Analysis. J. Biomol. Screen. 15, 726–734 (2010). https://doi.org/10.1177/1087057110370894.

50. Antoniou, N., Prodromidou, K., Kouroupi, G., Boumpoureka, I., Samiotaki, M., Panayotou, G., Xilouri, M., Kloukina, I., Stefanis, L., Grailhe, R., Taoufik, E., Matsas, R.: High content screening and proteomic analysis identify a kinase inhibitor that rescues pathological phenotypes in a patient-derived model of Parkinson's disease. npj Park. Dis. 8, 15 (2022). https://doi.org/10.1038/s41531-022-00278-y.

51. Hollandi, R., Szkalisity, A., Toth, T., Carpenter, A.E., Smith, K., Hollandi, R., Szkalisity, A., Toth, T., Tasnadi, E., Molnar, C., Mathe, B., Grexa, I.: Methods in Brief nucleAIzer : A Parameter-free Deep Learning Framework for Nucleus Segmentation Using Image Style Transfer ll ll Methods in Brief nucleAIzer : A Parameter-free Deep Learning Framework for Nucleus Segmentation Using Image Style Transfer. Cell Syst. 10, 453-458.e6 (2020). https://doi.org/10.1016/j.cels.2020.04.003.

52. Grimm, J.B., Lavis, L.D.: Caveat fluorophore: an insiders' guide to small-molecule fluorescent labels. Nat. Methods. 19, 149–158 (2022). https://doi.org/10.1038/s41592-021-01338-6.

53. Proteins, F.: Use of Fluorescent Probes : Their Effect on Cell Biology and Limitations. 2036, 2031–2036 (2012).

54. Bancroft, J.D., Gamble, M.: Theory and practice of histological techniques. Elsevier health sciences (2008).

55. Taqi, S.A., Sami, S.A., Sami, L.B., Zaki, S.A.: A review of artifacts in histopathology. J. Oral Maxillofac. Pathol. 22, 279 (2018). https://doi.org/10.4103/jomfp.JOMFP_125_15.

56. Underwood, J.C.E.: More than meets the eye: the changing face of histopathology. Histopathology. 70, 4–9 (2017). https://doi.org/10.1111/his.13047.

57. Veta, M., Pluim, J.P.W., van Diest, P.J., Viergever, M.A.: Breast Cancer Histopathology Image Analysis: A Review. IEEE Trans. Biomed. Eng. 61, 1400–1411 (2014). https://doi.org/10.1109/TBME.2014.2303852.

58. Lovitt, C.J., Shelper, T.B., Avery, V.M.: Advanced cell culture techniques for cancer drug discovery. Biology (Basel). 3, 345–367 (2014).

https://doi.org/10.3390/biology3020345.

59. Westhouse, R.A.: Safety assessment considerations and strategies for targeted small molecule cancer therapeutics in drug discovery. Toxicol. Pathol. 38, 165–168 (2010). https://doi.org/10.1177/0192623309354341.

60. Hughes, J.P., Rees, S., Kalindjian, S.B., Philpott, K.L.: Principles of early drug discovery. Br. J. Pharmacol. 162, 1239–1249 (2011). https://doi.org/10.1111/j.1476-5381.2010.01127.x.

61. Gomez-Roman, N., Stevenson, K., Gilmour, L., Hamilton, G., Chalmers, A.J.: A novel 3D human glioblastoma cell culture system for modeling drug and radiation responses. Neuro. Oncol. 19, 229–241 (2017). https://doi.org/10.1093/neuonc/now164.

62. Ramaiahgari, S.C., den Braver, M.W., Herpers, B., Terpstra, V., Commandeur, J.N.M., van de Water, B., Price, L.S.: A 3D in vitro model of differentiated HepG2 cell spheroids with improved liver-like properties for repeated dose high-throughput toxicity studies. Arch. Toxicol. 88, 1083–1095 (2014). https://doi.org/10.1007/s00204-014-1215-9.

63. Lv, D., Hu, Z., Lu, L., Lu, H., Xu, X.: Three-dimensional cell culture: A powerful tool in tumor research and drug discovery. Oncol. Lett. 14, 6999–7010 (2017). https://doi.org/10.3892/ol.2017.7134.

64. Huang, Y., Tong, L., Yi, L., Zhang, C., Hai, L., Li, T., Yu, S., Wang, W., Tao, Z., Ma, H., Liu, P., Xie, Y., Yang, X.: Three-dimensional hydrogel is suitable for targeted investigation of amoeboid migration of glioma cells. Mol. Med. Rep. 17, 250–256 (2018). https://doi.org/10.3892/mmr.2017.7888.

65. Lv, D., Yu, S.-C., Ping, Y.-F., Wu, H., Zhao, X., Zhang, H., Cui, Y., Chen, B., Zhang, X., Dai, J., Bian, X.-W., Yao, X.-H.: A three-dimensional collagen scaffold cell culture system for screening anti-glioma therapeutics. Oncotarget. 7, 56904–56914 (2016). https://doi.org/10.18632/oncotarget.10885.

66. Piccinini, F., Santis, I. De, Bevilacqua, A.: Advances in cancer modeling: fluidic systems for increasing representativeness of large 3D multicellular spheroids. Biotechniques. 65, 312–314 (2018). https://doi.org/10.2144/btn-2018-0153.

67. Cesarz, Z., Tamama, K.: Spheroid Culture of Mesenchymal Stem Cells. Stem Cells Int. 2016, 9176357 (2016). https://doi.org/10.1155/2016/9176357.

68. Sawant-Basak, A., Obach, R.S.: Emerging Models of Drug Metabolism, Transporters, and Toxicity. Drug Metab. Dispos. 46, 1556–1561 (2018). https://doi.org/10.1124/dmd.118.084293.

69. Sant, S., Johnston, P.A.: The production of 3D tumor spheroids for cancer drug discovery. Drug Discov. Today Technol. 23, 27–36 (2017). https://doi.org/https://doi.org/10.1016/j.ddtec.2017.03.002.

70. Di Modugno, F., Colosi, C., Trono, P., Antonacci, G., Ruocco, G., Nisticò, P.: 3D models in the new era of immune oncology: focus on T cells, CAF and ECM. J. Exp. Clin. Cancer Res. 38, 117 (2019). https://doi.org/10.1186/s13046-019-1086-2.

71. Lock, J.G., Stromblad, S.: Systems microscopy: an emerging strategy for the life sciences. Exp. Cell Res. 316, 1438–1444 (2010). https://doi.org/10.1016/j.yexcr.2010.04.001.

72. Boland, M. V, Murphy, R.F.: A neural network classifier capable of recognizing the patterns of all major subcellular structures in fluorescence microscope images of HeLa cells. Bioinformatics. 17, 1213–1223 (2001). https://doi.org/10.1093/bioinformatics/17.12.1213.

73. Young, D.W., Bender, A., Hoyt, J., McWhinnie, E., Chirn, G.-W., Tao, C.Y., Tallarico, J.A., Labow, M., Jenkins, J.L., Mitchison, T.J., Feng, Y.: Integrating high-content screening and ligand-target prediction to identify mechanism of action. Nat Chem Biol. 4, 59–68 (2008).

74. Gasparri, F., Mariani, M., Sola, F., Galvani, A.: Quantification of the proliferation index of human dermal fibroblast cultures with the ArrayScan high-content screening reader. J. Biomol. Screen. 9, 232–243 (2004). https://doi.org/10.1177/1087057103262836.

75. Carpenter, A.E., Jones, T.R., Lamprecht, M.R., Clarke, C., Kang, I.H., Friman, O., Guertin, D.A., Chang, J.H., Lindquist, R.A., Moffat, J., Golland, P., Sabatini, D.M.: CellProfiler: image analysis software for identifying and quantifying cell phenotypes. Genome Biol. 7, R100 (2006). https://doi.org/10.1186/gb-2006-7-10-

r100.

76. Molnar, J., Molnar, C., Horvath, P.: An Object Splitting Model Using Higher-Order Active Contours for Single-Cell Segmentation. In: Bebis, G., Boyle, R., Parvin, B., Koracin, D., Porikli, F., Skaff, S., Entezari, A., Min, J., Iwai, D., Sadagic, A., Scheidegger, C., and Isenberg, T. (eds.) Advances in Visual Computing: 12th International Symposium, ISVC 2016, Las Vegas, NV, USA, December 12-14, 2016, Proceedings, Part I. pp. 24–34. Springer International Publishing, Cham (2016). https://doi.org/10.1007/978-3-319-50835-1_3.

77. Molnar, C., Jermyn, I.H., Kato, Z., Rahkama, V., Östling, P., Mikkonen, P., Pietiäinen, V., Horvath, P.: Accurate Morphology Preserving Segmentation of Overlapping Cells based on Active Contours. Sci. Rep. 6, 32412 (2016). https://doi.org/10.1038/srep32412.

78. Achanta, R., Shaji, A., Smith, K., Lucchi, A., Fua, P., Susstrunk, S.: SLIC Superpixels Compared to State-of-the-Art Superpixel Methods. IEEE Trans. Pattern Anal. Mach. Intell. 34, 2274–2282 (2012). https://doi.org/10.1109/TPAMI.2012.120.

79. Achanta, R., Shaji, A., Smith, K., Lucchi, A., Fua, P., Süsstrunk, S.: Slic Superpixels Technical Report. (2010).

80. Neumann, B., Walter, T., Heriche, J.-K., Bulkescher, J., Erfle, H., Conrad, C., Rogers, P., Poser, I., Held, M., Liebel, U., Cetin, C., Sieckmann, F., Pau, G., Kabbe, R., Wunsche, A., Satagopam, V., Schmitz, M.H.A., Chapuis, C., Gerlich, D.W., Schneider, R., Eils, R., Huber, W., Peters, J.-M., Hyman, A.A., Durbin, R., Pepperkok, R., Ellenberg, J.: Phenotypic profiling of the human genome by time-lapse microscopy reveals cell division genes. Nature. 464, 721–727 (2010). https://doi.org/10.1038/nature08869.

81. Banerjee, I., Yamauchi, Y., Helenius, A., Horvath, P.: High-Content Analysis of Sequential Events during the Early Phase of Influenza A Virus Infection, (2013). https://doi.org/10.1371/journal.pone.0068450.

82. Jones, T.R., Kang, I.H., Wheeler, D.B., Lindquist, R.A., Papallo, A., Sabatini, D.M., Golland, P., Carpenter, A.E.: CellProfiler Analyst: data exploration and analysis software for complex image-based screens. BMC Bioinformatics. 9, 482 (2008).

https://doi.org/10.1186/1471-2105-9-482.

83. Jones, T.R., Carpenter, A.E., Lamprecht, M.R., Moffat, J., Silver, S.J., Grenier, J.K., Castoreno, A.B., Eggert, U.S., Root, D.E., Golland, P., Sabatini, D.M.: Scoring diverse cellular morphologies in image-based screens with iterative feedback and machine learning. Proc. Natl. Acad. Sci. U. S. A. 106, 1826–1831 (2009). https://doi.org/10.1073/pnas.0808843106.

84. Rämö, P., Sacher, R., Snijder, B., Begemann, B., Pelkmans, L.: CellClassifier: supervised learning of cellular phenotypes. Bioinformatics. 25, 3028–3030 (2009). https://doi.org/10.1093/bioinformatics/btp524.

85. Misselwitz, B., Strittmatter, G., Periaswamy, B., Schlumberger, M.C., Rout, S., Horvath, P., Kozak, K., Hardt, W.-D.: Enhanced CellClassifier: a multi-class classification tool for microscopy images, (2010). https://doi.org/10.1186/1471-2105-11-30.

86. Horvath, P., Wild, T., Kutay, U., Csucs, G.: Machine Learning Improves the Precision and Robustness of High-Content Screens. J. Biomol. Screen. 16, 1059–1067 (2011). https://doi.org/10.1177/1087057111414878.

87. Piccinini, F., Balassa, T., Szkalisity, A., Molnar, C., Paavolainen, L., Kujala, K., Buzas, K., Sarazova, M., Pietiainen, V., Kutay, U., Smith, K., Horvath, P.: Advanced Cell Classifier: User-Friendly Machine-Learning-Based Software for Discovering Phenotypes in High-Content Imaging Data. Cell Syst. 4, 651-655.e5 (2017). https://doi.org/10.1016/j.cels.2017.05.012.

88. Orlov, N., Shamir, L., Macura, T., Johnston, J., Eckley, D.M., Goldberg, I.G.: WND-CHARM: Multi-purpose image classification using compound image transforms. Pattern Recognit. Lett. 29, 1684–1693 (2008). https://doi.org/http://dx.doi.org/10.1016/j.patrec.2008.04.013.

89. Uhlmann, V., Singh, S., Carpenter, A.E.: CP-CHARM: segmentation-free image classification made accessible. BMC Bioinformatics. 17, 51 (2016). https://doi.org/10.1186/s12859-016-0895-y.

90. Elowitz, M.B., Levine, A.J., Siggia, E.D., Swain, P.S.: Stochastic gene expression in a single cell. Science. 297, 1183–1186 (2002).

https://doi.org/10.1126/science.1070919.

91. Maheshri, N., O'Shea, E.K.: Living with noisy genes: how cells function reliably with inherent variability in gene expression. Annu. Rev. Biophys. Biomol. Struct. 36, 413–434 (2007). https://doi.org/10.1146/annurev.biophys.36.040306.132705.

92. Raj, A., van Oudenaarden, A.: Nature, nurture, or chance: stochastic gene expression and its consequences. Cell. 135, 216–226 (2008). https://doi.org/10.1016/j.cell.2008.09.050.

93. Snijder, B., Sacher, R., Ramo, P., Damm, E.-M., Liberali, P., Pelkmans, L.: Population context determines cell-to-cell variability in endocytosis and virus infection. Nature. 461, 520–523 (2009). https://doi.org/10.1038/nature08282.

94. Vlamakis, H., Aguilar, C., Losick, R., Kolter, R.: Control of cell fate by the formation of an architecturally complex bacterial community. Genes Dev. 22, 945–953 (2008). https://doi.org/10.1101/gad.1645008.

95. Ljosa, V., Sokolnicki, K.L., Carpenter, A.E.: Annotated high-throughput microscopy image sets for validation. Nat Meth. 9, 637 (2012).

96. Caie, P.D., Walls, R.E., Ingleston-Orme, A., Daya, S., Houslay, T., Eagle, R., Roberts, M.E., Carragher, N.O.: High-Content Phenotypic Profiling of Drug Response Signatures across Distinct Cancer Cells. Mol. Cancer Ther. 9, 1913 LP – 1926 (2010).

97. Smith, K., Horvath, P.: Active Learning Strategies for Phenotypic Profiling of High-Content Screens. J. Biomol. Screen. 19, 685–695 (2014). https://doi.org/10.1177/1087057114527313.

98. Scheeder, C., Heigwer, F., Boutros, M.: Machine learning and image-based profiling in drug discovery. Curr. Opin. Syst. Biol. 10, 43–52 (2018). https://doi.org/https://doi.org/10.1016/j.coisb.2018.05.004.

99. Lin, D., Sun, L., Toh, K.-A., Zhang, J.B., Lin, Z.: Biomedical image classification based on a cascade of an SVM with a reject option and subspace analysis. Comput. Biol. Med. 96, 128–140 (2018). https://doi.org/https://doi.org/10.1016/j.compbiomed.2018.03.005.

100. Dufour, A.C., Jonker, A.H., Olivo-Marin, J.C.: Deciphering tissue morphodynamics

using bioimage informatics. Philos. Trans. R. Soc. B Biol. Sci. 372, (2017). https://doi.org/10.1098/rstb.2015.0512.

101. Gupta, A., Harrison, P.J., Wieslander, H., Pielawski, N., Kartasalo, K., Partel, G., Solorzano, L., Suveer, A., Klemm, A.H., Spjuth, O., Sintorn, I.M., Wählby, C.: Deep Learning in Image Cytometry: A Review. Cytom. Part A. 95, 366–380 (2019). https://doi.org/10.1002/cyto.a.23701.

102. Standke, S.J., Colby, D.H., Bensen, R.C., Burgett, A.W.G., Yang, Z.: Mass Spectrometry Measurement of Single Suspended Cells Using a Combined Cell Manipulation System and a Single-Probe Device. Anal. Chem. 91, 1738–1742 (2019). https://doi.org/10.1021/acs.analchem.8b05774.

103. Mattiazzi Usaj, M., Sahin, N., Friesen, H., Pons, C., Usaj, M., Masinas, M.P.D., Shuteriqi, E., Shkurin, A., Aloy, P., Morris, Q., Boone, C., Andrews, B.J.: Systematic genetics and single-cell imaging reveal widespread morphological pleiotropy and cell-to-cell variability. Mol. Syst. Biol. 16, e9243 (2020). https://doi.org/10.15252/msb.20199243.

104. Coudray, N., Ocampo, P.S., Sakellaropoulos, T., Narula, N., Snuderl, M., Fenyö, D., Moreira, A.L., Razavian, N., Tsirigos, A.: Classification and mutation prediction from non–small cell lung cancer histopathology images using deep learning. Nat. Med. 24, 1559–1567 (2018). https://doi.org/10.1038/s41591-018-0177-5.

105. Sullivan, D.P., Winsnes, C.F., Åkesson, L., Hjelmare, M., Wiking, M., Schutten, R., Campbell, L., Leifsson, H., Rhodes, S., Nordgren, A., Smith, K., Revaz, B., Finnbogason, B., Szantner, A., Lundberg, E.: Deep learning is combined with massive-scale citizen science to improve large-scale image classification. Nat. Biotechnol. 36, 820–828 (2018). https://doi.org/10.1038/nbt.4225.

106. Ouyang, W., Winsnes, C.F., Hjelmare, M., Cesnik, A.J., Åkesson, L., Xu, H., Sullivan, D.P., Dai, S., Lan, J., Jinmo, P., Galib, S.M., Henkel, C., Hwang, K., Poplavskiy, D., Tunguz, B., Wolfinger, R.D., Gu, Y., Li, C., Xie, J., Buslov, D., Fironov, S., Kiselev, A., Panchenko, D., Cao, X., Wei, R., Wu, Y., Zhu, X., Tseng, K.-L., Gao, Z., Ju, C., Yi, X., Zheng, H., Kappel, C., Lundberg, E.: Analysis of the Human Protein Atlas Image Classification competition. Nat. Methods. 16, 1254–1261 (2019). https://doi.org/10.1038/s41592-019-0658-6.

107. Thul, P.J., Åkesson, L., Wiking, M., Mahdessian, D., Geladaki, A., Ait Blal, H., Alm, T., Asplund, A., Björk, L., Breckels, L.M., Bäckström, A., Danielsson, F., Fagerberg, L., Fall, J., Gatto, L., Gnann, C., Hober, S., Hjelmare, M., Johansson, F., Lee, S., Lindskog, C., Mulder, J., Mulvey, C.M., Nilsson, P., Oksvold, P., Rockberg, J., Schutten, R., Schwenk, J.M., Sivertsson, Å., Sjöstedt, E., Skogs, M., Stadler, C., Sullivan, D.P., Tegel, H., Winsnes, C., Zhang, C., Zwahlen, M., Mardinoglu, A., Pontén, F., von Feilitzen, K., Lilley, K.S., Uhlén, M., Lundberg, E.: A subcellular map of the human proteome. Science (80-.). 356, eaal3321 (2017). https://doi.org/10.1126/science.aal3321.

108. Bove, A., Gradeci, D., Fujita, Y., Banerjee, S., Charras, G., Lowe, A.R.: Local cellular neighborhood controls proliferation in cell competition. Mol. Biol. Cell. 28, 3215–3228 (2017). https://doi.org/10.1091/mbc.e17-06-0368.

109. Mesa, K.R., Kawaguchi, K., Cockburn, K., Gonzalez, D., Boucher, J., Xin, T., Klein, A.M., Greco, V.: Homeostatic Epidermal Stem Cell Self-Renewal Is Driven by Local Differentiation. Cell Stem Cell. 23, 677-686.e4 (2018). https://doi.org/10.1016/j.stem.2018.09.005.

110. Sahin, C.: The Geometry and Usage of the Supplementary Fisheye Lenses in Smartphones. Smartphones from an Appl. Res. Perspect. (2017). https://doi.org/10.5772/intechopen.69691.

111. Schmalstieg, D., Hollerer, T.: Augmented reality: principles and practice. Addison-Wesley Professional (2016).

112. Sáez, Á., Bergasa, L.M., López-Guillén, E., Romera, E., Tradacete, M., Gómez-Huélamo, C., del Egido, J.: Real-Time Semantic Segmentation for Fisheye Urban Driving Images Based on ERFNet, (2019). https://doi.org/10.3390/s19030503.

113. Tseng, D., Chen, C., Tseng, C.: Automatic detection and tracking in multi-fisheye cameras surveillance system. Int. J. Comput. Elect. Eng. 9, (2017).

114. Li, T., Tong, G., Tang, H., Li, B., Chen, B.: FisheyeDet: A Self-Study and Contour-Based Object Detector in Fisheye Images. IEEE Access. 8, 71739–71751 (2020). https://doi.org/10.1109/ACCESS.2020.2987868.

115. Silberstein, S., Levi, D., Kogan, V., Gazit, R.: Vision-based pedestrian detection for

rear-view cameras. In: 2014 IEEE Intelligent Vehicles Symposium Proceedings. pp. 853–860 (2014). https://doi.org/10.1109/IVS.2014.6856399.

116. Bertozzi, M., Castangia, L., Cattani, S., Prioletti, A., Versari, P.: 360° Detection and tracking algorithm of both pedestrian and vehicle using fisheye images. In: 2015 IEEE Intelligent Vehicles Symposium (IV). pp. 132–137 (2015). https://doi.org/10.1109/IVS.2015.7225675.

117. Jaderberg, M., Simonyan, K., Zisserman, A., kavukcuoglu, koray: Spatial Transformer Networks. In: Cortes, C., Lawrence, N., Lee, D., Sugiyama, M., and Garnett, R. (eds.) Advances in Neural Information Processing Systems. Curran Associates, Inc. (2015).

118. Rios, A.C., Clevers, H.: Imaging organoids: a bright future ahead. Nat. Methods. 15, 24–26 (2018). https://doi.org/10.1038/nmeth.4537.

119. Method of the Year 2014. Nat. Methods. 12, 1 (2015). https://doi.org/10.1038/nmeth.3251.

120. Costa, E.C., Silva, D.N.: Optical clearing methods : An overview of the techniques used for the imaging of 3D spheroids. 2742–2763 (2019). https://doi.org/10.1002/bit.27105.

121. Richardson, D.S., Lichtman, J.W.: Clarifying Tissue Clearing. (2015). https://doi.org/10.1016/j.cell.2015.06.067.

122. Tian, T., Yang, Z., Li, X.: Tissue clearing technique : Recent progress and biomedical applications. 489–507 (2021). https://doi.org/10.1111/joa.13309.

123. Ueda, H.R., Ertürk, A., Chung, K., Gradinaru, V., Chédotal, A., Tomancak, P., Keller, P.J.: Tissue clearing and its applications in neuroscience. Nat. Rev. Neurosci. 21, 61–79 (2020). https://doi.org/10.1038/s41583-019-0250-1.

124. Richardson, D.S., Guan, W., Matsumoto, K., Pan, C., Chung, K., Ertürk, A., Ueda, H.R., Lichtman, J.W.: Tissue clearing. Nat. Rev. Methods Prim. 1, 1–24 (2021). https://doi.org/10.1038/s43586-021-00080-9.

125. Tainaka, K., Kuno, A., Kubota, S.I., Murakami, T., Ueda, H.R.: Chemical Principles in Tissue Clearing and Staining Protocols for Whole-Body Cell Profiling. Annu. Rev. Cell Dev. Biol. 32, 713–741 (2016). https://doi.org/10.1146/annurev-cellbio-

111315-125001.

126. Dekkers, J.F., Alieva, M., Wellens, L.M., Ariese, H.C.R., Jamieson, P.R., Vonk, A.M., Amatngalim, G.D., Hu, H., Oost, K.C., Snippert, H.J.G., Beekman, J.M., Wehrens, E.J., Visvader, J.E., Clevers, H., Rios, A.C.: High-resolution 3D imaging of fixed and cleared organoids. Nat. Protoc. 14, 1756–1771 (2019). https://doi.org/10.1038/s41596-019-0160-8.

127. Smyrek, I., Stelzer, E.H.K.: Quantitative three-dimensional evaluation of immunofluorescence staining for large whole mount spheroids with light sheet microscopy. Biomed. Opt. Express. 8, 484 – 499 (2017). https://doi.org/10.1364/BOE.8.000484.

128. Costa, E.C., Moreira, A.F., de Melo-Diogo, D., Correia, I.J.: Polyethylene glycol molecular weight influences the ClearT2 optical clearing method for spheroids imaging by confocal laser scanning microscopy. J. Biomed. Opt. 23, 55003 (2018). https://doi.org/10.1117/1.JBO.23.5.055003.

129. Ansari, N., Müller, S., Stelzer, E.H.K., Pampaloni, F.: Chapter 13 - Quantitative 3D Cell-Based Assay Performed with Cellular Spheroids and Fluorescence Microscopy. In: Conn, P.M.B.T.-M. in C.B. (ed.) Laboratory Methods in Cell Biology. pp. 295–309. Academic Press (2013). https://doi.org/https://doi.org/10.1016/B978-0-12-407239-8.00013-6.

130. Kolesová, H., Čapek, M., Radochová, B., Janáček, J., Sedmera, D.: Comparison of different tissue clearing methods and 3D imaging techniques for visualization of GFP-expressing mouse embryos and embryonic hearts. Histochem. Cell Biol. 146, 141–152 (2016). https://doi.org/10.1007/s00418-016-1441-8.

131. Schindelin, J., Arganda-Carreras, I., Frise, E., Kaynig, V., Longair, M., Pietzsch, T., Preibisch, S., Rueden, C., Saalfeld, S., Schmid, B., Tinevez, J.-Y., White, D.J., Hartenstein, V., Eliceiri, K., Tomancak, P., Cardona, A.: Fiji: an open-source platform for biological-image analysis. Nat. Methods. 9, 676–682 (2012). https://doi.org/10.1038/nmeth.2019.

132. Diosdi, A., Hirling, D., Kovacs, M., Toth, T., Harmati, M., Koos, K., Buzas, K., Piccinini, F., Horvath, P.: Cell lines and clearing approaches : a single-cell level 3D light-sheet fluorescence microscopy dataset of multicellular spheroids. Data Br. 36,

107090 (2021). https://doi.org/10.1016/j.dib.2021.107090.

133. Kuwajima, T., Sitko, A.A., Bhansali, P., Jurgens, C., Guido, W., Mason, C.: ClearT: a detergent- and solvent-free clearing method for neuronal and non-neuronal tissue. Development. 140, 1364–1368 (2013). https://doi.org/10.1242/dev.091844.

134. Susaki, E.A., Tainaka, K., Perrin, D., Kishino, F., Tawara, T., Watanabe, T.M., Yokoyama, C., Onoe, H., Eguchi, M., Yamaguchi, S., Abe, T., Kiyonari, H., Shimizu, Y., Miyawaki, A., Yokota, H., Ueda, H.R.: Whole-Brain Imaging with Single-Cell Resolution Using Chemical Cocktails and Computational Analysis. Cell. 157, 726–739 (2014). https://doi.org/https://doi.org/10.1016/j.cell.2014.03.042.

135. Hama, H., Kurokawa, H., Kawano, H., Ando, R., Shimogori, T., Noda, H., Fukami, K., Sakaue-Sawano, A., Miyawaki, A.: Scale: a chemical approach for fluorescence imaging and reconstruction of transparent mouse brain. Nat. Neurosci. 14, 1481–1488 (2011). https://doi.org/10.1038/nn.2928.

136. Tsai, P.S., Kaufhold, J.P., Blinder, P., Friedman, B., Drew, P.J., Karten, H.J., Lyden, P.D., Kleinfeld, D.: Correlations of neuronal and microvascular densities in murine cortex revealed by direct counting and colocalization of nuclei and vessels. J. Neurosci. Off. J. Soc. Neurosci. 29, 14553–14570 (2009). https://doi.org/10.1523/JNEUROSCI.3287-09.2009.

137. Molnar, J., Tasnadi, E., Kintses, B., Farkas, Z., Pal, C., Horvath, P., Danka, T.: Active Surfaces for Selective Object Segmentation in 3D. In: 2017 International Conference on Digital Image Computing: Techniques and Applications (DICTA). pp. 1–7 (2017). https://doi.org/10.1109/DICTA.2017.8227401.

138. Nolden, M., Zelzer, S., Seitel, A., Wald, D., Müller, M., Franz, A.M., Maleike, D., Fangerau, M., Baumhauer, M., Maier-Hein, L., Maier-Hein, K.H., Meinzer, H.-P., Wolf, I.: The Medical Imaging Interaction Toolkit: challenges and advances : 10 years of open-source development. Int. J. Comput. Assist. Radiol. Surg. 8, 607–620 (2013). https://doi.org/10.1007/s11548-013-0840-8.

139. Weigert, M., Schmidt, U., Haase, R., Sugawara, K., Myers, G.: Star-convex polyhedra for 3D object detection and segmentation in microscopy. Proc. - 2020 IEEE Winter Conf. Appl. Comput. Vision, WACV 2020. 3655–3662 (2020).

https://doi.org/10.1109/WACV45572.2020.9093435.

140. Lotufo, R.A., Falcao, A.X., Zampirolli, F.A.: IFT-Watershed from gray-scale marker. In: Proceedings. XV Brazilian Symposium on Computer Graphics and Image Processing. pp. 146–152 (2002). https://doi.org/10.1109/SIBGRA.2002.1167137.

141. Ozgur Cicek, Ahmed Abdulkabdir, Soeren S. Lienkamp, Thomas Brox, O.R.: 3D U_net. Med. Image Comput. Comput. Interv. 424–432 (2016). https://doi.org/10.1007/978-3-319-46723-8.

142. Carragher, N., Piccinini, F., Tesei, A., Jr, O.J.T., Bickle, M., Horvath, P.: Concerns, challenges and promises of high-content analysis of 3D cellular models. Nat. Rev. Drug Discov. 17, 606 (2018). https://doi.org/10.1038/nrd.2018.99.

143. le Roux, L., Volgin, A., Maxwell, D., Ishihara, K., Gelovani, J., Schellingerhout, D.: Optimizing imaging of three-dimensional multicellular tumor spheroids with fluorescent reporter proteins using confocal microscopy. Mol. Imaging. 7, 214–221 (2008).

144. Ossipova, O., Sokol, S.Y.: Cryosectioning and Immunostaining of Xenopus Embryonic Tissues. Cold Spring Harb. Protoc. 2021, pdb.prot107151 (2021). https://doi.org/10.1101/pdb.prot107151.

145. Hoque, M.Z., Keskinarkaus, A., Nyberg, P., Mattila, T., Seppänen, T.: Whole slide image registration via multi-stained feature matching. Comput. Biol. Med. 144, 105301 (2022). https://doi.org/https://doi.org/10.1016/j.compbiomed.2022.105301.

146. Lu, J., Öfverstedt, J., Lindblad, J., Sladoje, N.: Is image-to-image translation the panacea for multimodal image registration? A comparative study. PLoS One. 17, 1–33 (2022). https://doi.org/10.1371/journal.pone.0276196.

Supplementary

Section 1 – Significance test for the results with SMO classifier in the case of the MCF-7 dataset

We compare our results to an earlier study, in which the MCF-7 dataset was analysed with Advanced Cell Classifier. In that study, the highest accuracy reached considering regular features only was 88.4%, using the SimpleLogistic (Logistic Boost) classifier, while in this paper we report 90.8% best performance with the combination of regular and neighbourhood features (SMO classifier). The 2.4% difference in accuracy is significant. We randomized our data several times and calculated the accuracies with the mentioned classifiers (Logistic Boost for information from single-cells only, and SMO for data with neighbourhood features).

Advanced Cell Classifier Logistic Boost accuracies:	Neighbourhood SMO accuracies:
88.3443	90.795
88.5236	90.9145
88.2845	90.4363
88.165	90.1973
88.2247	90.9743

As a statistical procedure, two-sample t-test was performed, we considered the result significant at $p < 0.05$.

Descriptive Statistics		*N*	*Mean*	*SD*	*SEM*
ACC		5	88.30842	0.1376	0.06154
Neighbourhood		5	90.66348	0.33386	0.14931
	Difference:		-2.35506		

t-Test Statistics	*t Statistic*	*DF*	*Prob>|t|*
Equal Variance Assumed	-14.58315	8	4.79E-07
Equal Variance NOT Assumed	-14.58315	5.3209	1.71E-05

Null hypothesis: mean1-mean2 = 0

Alternative hypothesis: mean1-mean2 <> 0

At the 0.05 level, the difference is significant.

Section 2- Significance tests for the results with the fisheye transformation method

MCF-7

Our best result (accuracy: 91.38%) for this dataset with the fisheye-transformation appears with a window size of 543 pixels with a focal length of 130 arbitrary units when we used ResNet50. We compare this result to a baseline, where we used ResNet50 (accuracy: 84.31%). For the baseline we cropped out images around the cells' centre with 192x192 pixel diameter (so in this case, we haven't performed fisheye transformation on the original images). Deep learning calculations were run 5-5 times on both the baseline and the fisheye transformed data.

MCF7 baseline accuracies	MCF7 best accuracies
82,23	92
84,89	90,15
85,03	91,08
84,17	91,68
85,23	91,99

As a statistical procedure, two-sample t-test was performed, we considered the result significant at p <0.05.

Descriptive statistics

		N	Mean	SD	SEM	Median
MCF7_baseline		5	84,31	1,22955	0,54987	84,89
MCF7_best		5	91,38	0,78253	0,34996	91,68
	Difference	5	-7,07		0,65179	-6,76

t-Test Statistics

	t Statistic	DF	Prob>|t|
Equal Variance Assumed	-10,8471	8	4,61E-06
Equal Variance NOT Assumed (Welch Correction)	-10,8471	6,78368	1,56E-05

Null hypothesis: mean1-mean2 = 0

Alternative hypothesis: mean1-mean2 <> 0

At the 0.05 level, the 7.07% difference in accuracy is significant.

Urinary Bladder Cancer

Our best result (accuracy: 98.14%)for this dataset with the fisheye-transformation appears with a window size of 272 pixels with a focal length of 150 arbitrary units when we used ResNet50. We compare this result to a baseline, where we used ResNet50 (accuracy: 94.41%). For the baseline we cropped out images around the cells' centre with 192x192 pixel diameter (so in this case, we haven't performed fisheye transformation on the original images). Deep learning calculations were run 5-5 times on both the baseline and the fisheye transformed data.

UBC baseline accuracies	UBC best accuracies
94,12	97,94
94,68	98,24
94,04	98,24
94,85	97,97
94,36	98,31

As a statistical procedure, two-sample t-test was performed, we considered the result significant at p <0.05.

Descriptive statistics

		N	Mean	SD	SEM	Median
UBC_baseline		5	94,41	0,35	0,15652	94,36
UBC_best		5	98,14	0,17161	0,07675	98,24
	Difference	5	-3,73		0,17433	-3,82

t-Test Statistics

	t Statistic	DF	Prob>|t|
Equal Variance Assumed	-21,3965	8	2,40E-08

Equal Variance NOT Assumed (Welch Correction)	-21,3965	5,81818	9,37E-07

Null hypothesis: mean1-mean2 = 0

Alternative hypothesis: mean1-mean2 <> 0

At the 0.05 level, the 3.83% difference in accuracy is significant.

Lung Cancer

Our best result (accuracy: 99.46%)for this dataset with the fisheye-transformation appears with a window size of 272 pixels with a focal length of 170 arbitrary units when we used inceptionV3. We compare this result to a baseline, where we used inceptionV3 (accuracy: 97.25%). For the baseline we cropped out images around the cells' centre with 192x192 pixel diameter (so in this case, we haven't performed fisheye transformation on the original images). Deep learning calculations were run 5-5 times on both the baseline and the fisheye transformed data.

LC baseline accuracies	LC best accuracies
97,32	99,64
97,54	98,97
97,01	99,57
97,03	99,54
97,35	99,58

As a statistical procedure, two-sample t-test was performed, we considered the result significant at $p < 0.05$.

Descriptive statistics						
		N	Mean	SD	SEM	Median
Lung_baseline		5	97,25	0,22638	0,10124	97,32
Lung_best		5	99,46	0,27632	0,12357	99,57
	Difference	5	-2,21		0,15975	-2,32

t-Test Statistics

	t Statistic	DF	Prob>|t|
Equal Variance Assumed	-13,8341	8	7,20E-07
Equal Variance NOT Assumed (Welch Correction)	-13,8341	7,70198	1,03E-06

Null hypothesis: mean1-mean2 = 0

Alternative hypothesis: mean1-mean2 <> 0

At the 0.05 level, the 2.21% difference in accuracy is significant.

iWildCam2020

Our best result (accuracy: 95.48%)for this dataset with the fisheye-transformation appears when 2.5× the size of bounding boxes were considered as the neighbourhood feature and focal length was set to 150 units and we used ResNet50. We compare this result to a baseline, where we used ResNet50 (accuracy: 95.3%). For the baseline we cropped out images with different dimensions based on the bounding boxes provided by the Kaggle organisers (so in this case, we haven't performed fisheye transformation on the images). Deep learning calculations were run 5-5 times on both the baseline and the fisheye transformed data.

iWildCam baseline accuracies	iWildCam best accuracies
95,32	95,51
95,29	95,46
95,27	95,49
95,33	95,46
95,29	95,48

As a statistical procedure, two-sample t-test was performed, we considered the result significant at p <0.05.

Descriptive statistics					
	N	Mean	SD	SEM	Median
iWildCam_baseline	5	95,3	0,02449	0,01095	95,29
iWildCam_best	5	95,48	0,02121	0,00949	95,48

Difference	5	-0,18		0,01449	-0,19

t-Test Statistics			
	t Statistic	DF	Prob>|t|
Equal Variance Assumed	-12,4212	8	1,65E-06
Equal Variance NOT Assumed (Welch Correction)	-12,4212	7,84	1,96E-06

Null hypothesis: mean1-mean2 = 0

Alternative hypothesis: mean1-mean2 <> 0

At the 0.05 level, the 0.18% difference in accuracy is significant.

**Section 3 – Machine learning classification results for 3D co-culture spheroid**

In the case of the 3D cell culture dataset (described in Chapter 5.2.1), we extracted all regular features of the cells that is possible to calculate in BIAS. Namely:

- *Shape features*: elongation, equivalent ellipsoid diameters, equivalent sphere diameter, equivalent sphere perimeter, extent, Feret diameter, flatness, number of components, principal moments, rotation invariants, roundness, surface voxels, volumetry, voxels

- *Intensity features (for both the blue and the red channel)*: integrated, minimum, maximum, mean, median and standard deviation statistics of a 3D region

We used the RandomForest and Multilayer Perceptron algorithms for the classification. With 10-fold cross validation we got the following classification accuracies: RandomForest: 98.5%, Multilayer Perceptron: 99.5%.
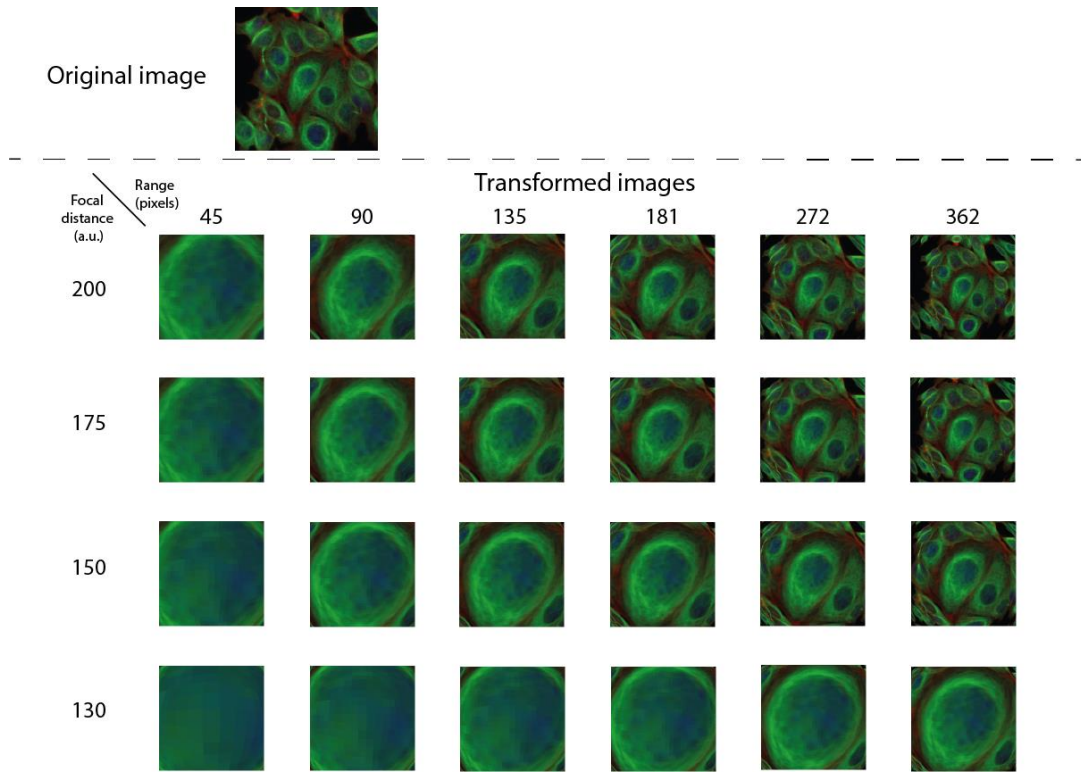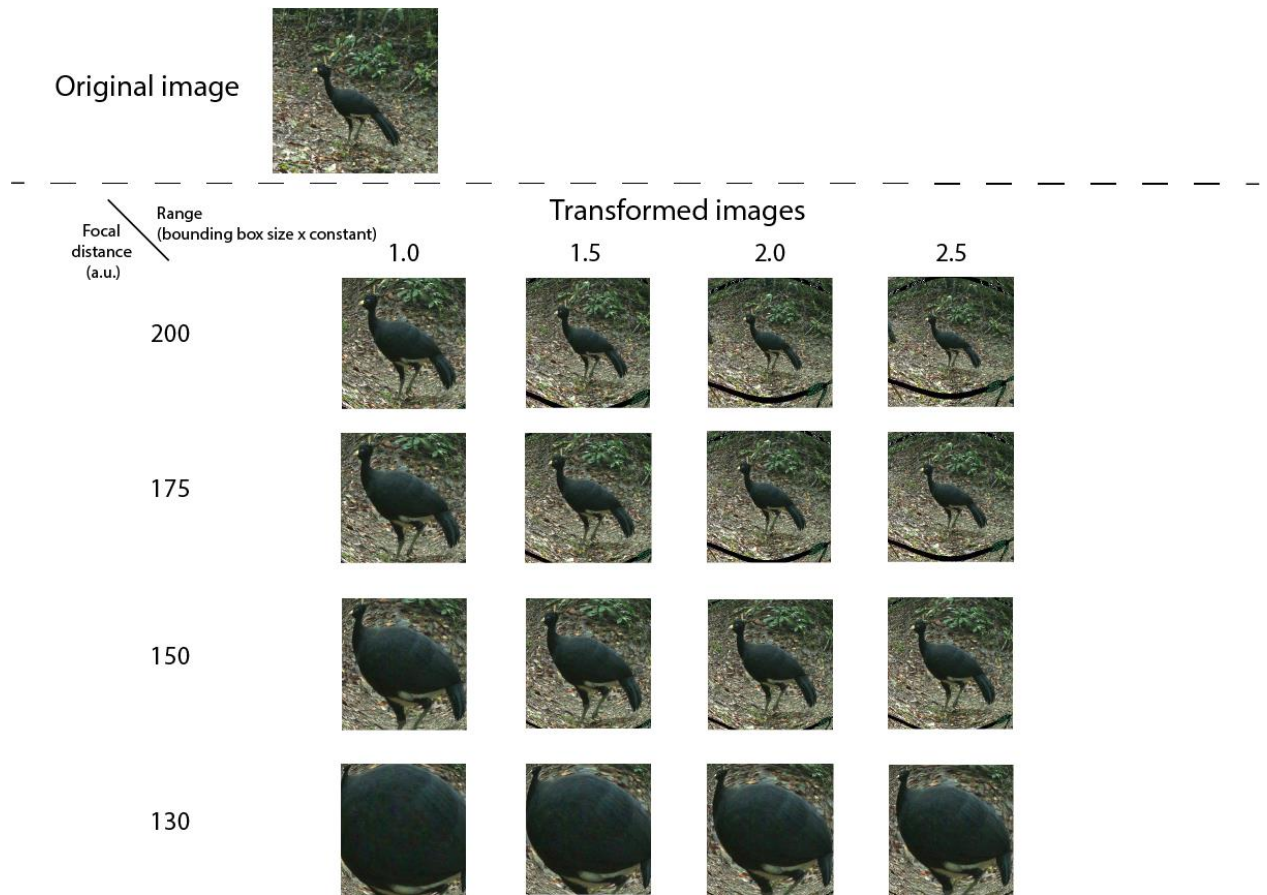
Supplementary Figure S1. Examples of the fisheye transformation with different window sizes (ranges) and focal distances using the 'equidistant' mapping function in the MCF-7 cell culture dataset.
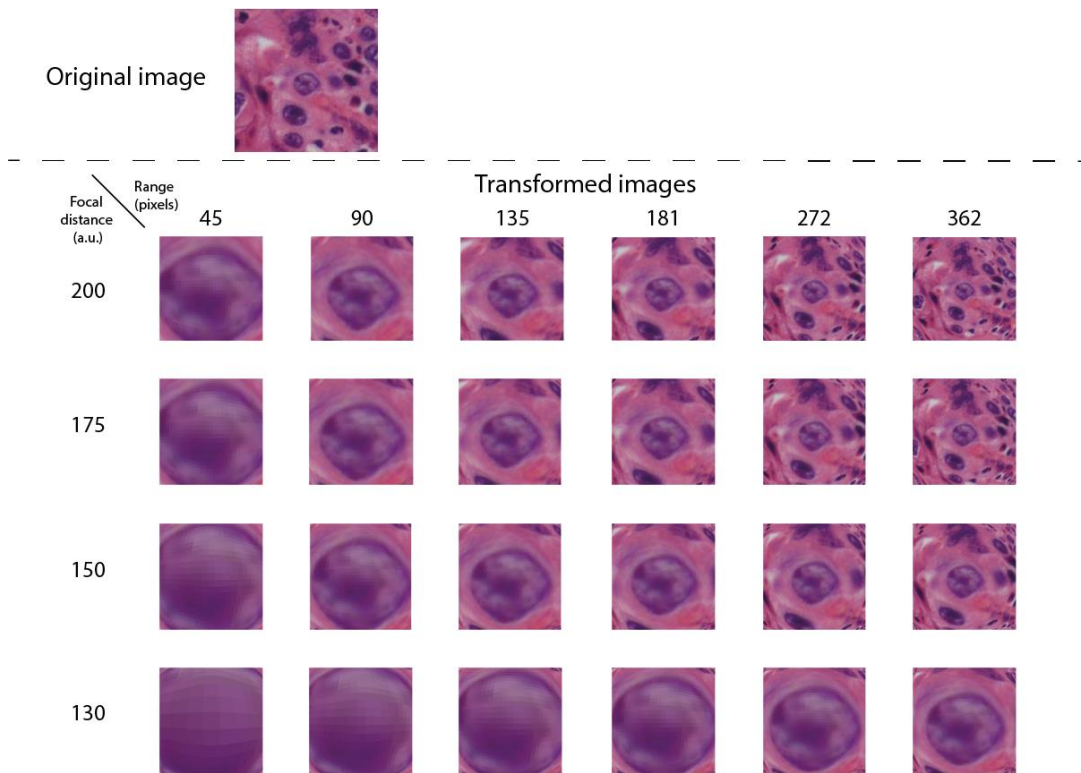
Supplementary Figure S2. Examples of the fisheye transformation with different window sizes (ranges) and focal distances using the 'equidistant' mapping function in the urinary bladder cancer tissue dataset.
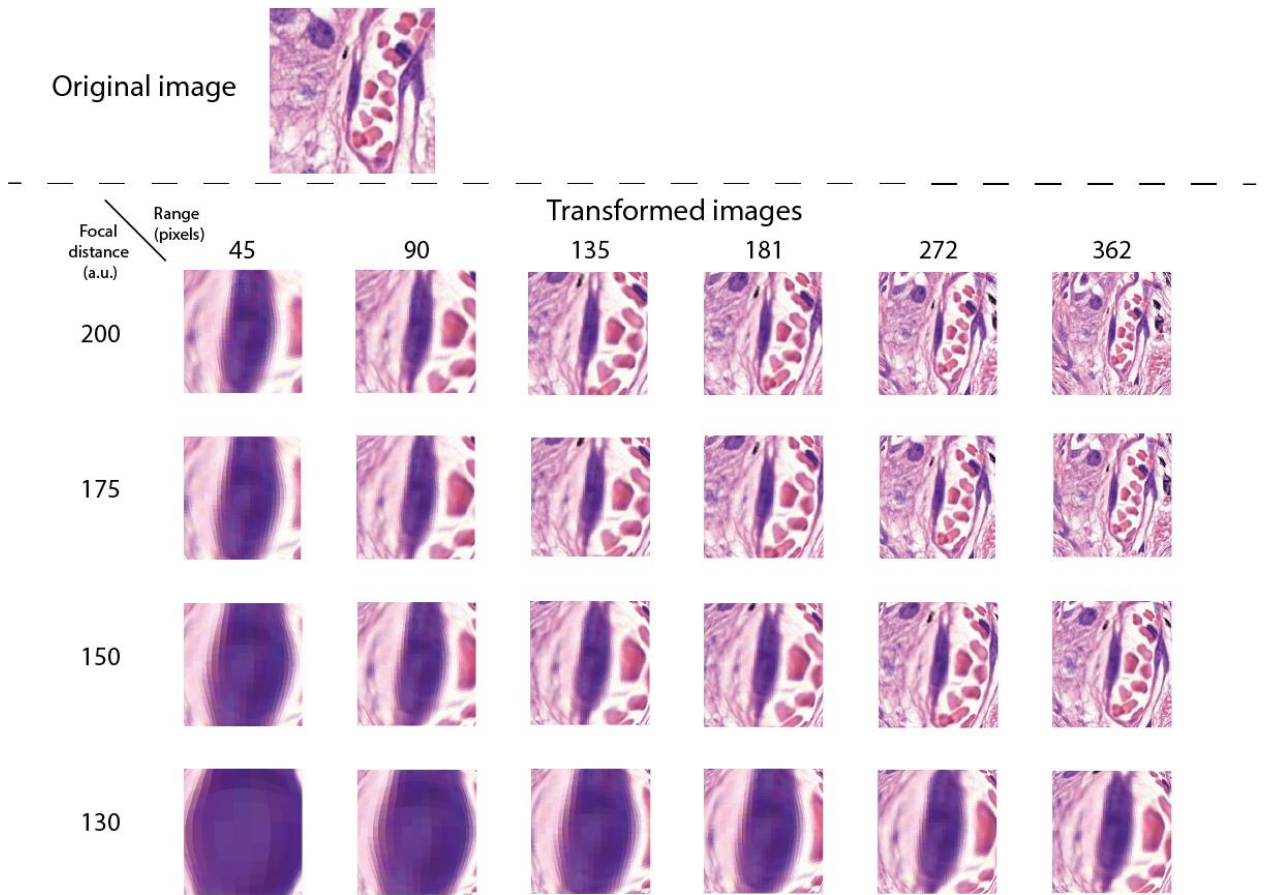
Supplementary Figure S3. Examples of the fisheye transformation with different window sizes (ranges) and focal distances using the 'equidistant' mapping function in the lung cancer tissue dataset.

Supplementary Figure S4. Examples of the fisheye transformation with different window sizes (ranges) and focal distances using the 'equidistant' mapping function in the iWildCam2020 dataset.